Preparation and characterization of undoped and transition metal doped TiO_2 nanoparticles for the photocatalytic degradation of phthalate esters

A

Thesis

Submitted in the partial fulfillment of the

requirements for the award of degree of

DOCTOR OF PHILOSOPHY

By

Pooja Singla

(Regn. No. 901212008)

Under the Supervision of

Dr. Kulvir Singh
(Professor)

Dr. O.P. Pandey
(Senior Professor)

School of Physics and Materials Science

Thapar University, Patiala-147004 (Punjab), India

September, 2017

DEDICATED

TO MY

FAMILY

CERTIFICATE

This is to certify that the thesis entitled **"Preparation and characterization of undoped and transition metal doped TiO_2 nanoparticles for the photocatalytic degradation of phthalate esters"** in the partial fulfillment of the requirements for the award of the degree of Doctor of Philosophy in the School of Physics and materials Science, Thapar University, Patiala is an authentic record of my own work carried out under the supervision of Dr. Kulvir Singh and Dr. O.P. Pandey. The thesis has not been submitted in part or full to any other university or institute for the award of any degree.

P. Singla

(Pooja Singla) **Date:** 4.09.2017

(901212008)

This is to certify that the above statement made by the candidate is correct and true to the best of my knowledge.

Dr. Kulvir Singh
(Professor)
School of Physics and Materials Science
Thapar University
Patiala-147004

Dr. O.P. Pandey
(Senior Professor)
School of Physics and Materials Science
Thapar University
Patiala-147004

ACKNOWLEDGEMENTS

This thesis is the culmination of my journey of Ph.D which was just like climbing a high peak step by step accompanied with hardship, encouragement, a bit frustration, and huge trust. At this moment of accomplishment, I would like to express my sincere thanks to those who have contributed to this thesis and supported me in many ways during this journey.

First of all I am indebted to my supervisors, **Dr. Kulvir Singh** and **Dr. O.P. Pandey** for their guidance, encouragement, understanding and personal attention. **Dr. Kulvir Singh** has always been a great support to me throughout my Ph.D. He has always provided decisive and energetic support. His deep insights always helped me. Words fail to express my deep sense of gratitude to **Dr. O.P. Pandey** for his support, positive criticism, suggestions, ideas and devoted time. It would be impossible to count all the ways that he has helped me in my work. His commitment towards work will always inspire me. I am thankful to him for his support and kindness.

I would like to express my thanks to my Doctoral committee members, **Dr. B.C. Mohanty**, **Dr. Amjad Ali** and **Dr. S.D. Tiwari** for their valuable suggestions and criticism during my progress report presentations. I am grateful to **Dr. Manoj Sharma**, Head, School of Physics and Materials Science for providing the help and support whenever required. I am thankful to **Dr. B.N. Chudasama** and **Ms. Loveleen Kaur Brar** for their suggestions and whole-hearted willingness to discuss the ideas about work. I am profoundly obliged to **Prof. Prakash Gopalan,** Director, Thapar University, Patiala for his generous financial assistance and facilitation.

I am grateful to my dear friends and colleagues, Dr. Satwinder Singh, Dr. Paramjyot Jha, Dr. Alok Garg, Mr. Devender Kumar, Dr. Gurbinder Kaur, Ms. Neetu Bansal, Mr. Ayush Gupta, Mr. Piyush Sharma, Mr. Savid Khan, Ms. Amandeep Kaur, Dr. Samita Thakur, Dr. Sakshi Goyal,

Ms Purnima Sharma, Ms. Parveer Kaur, Ms. Navjot Kaur, Dr. Mintu Tyagi, Dr. Chandni Khurana, Dr. Gaurav Singla, Ms. Rajinder Kaur, Ms. Manpreet Kaur, Mr. Parveen Jha, Dr. Sunil Kumar Arya, Ms. Indu Gupta, Ms. Baldeep Kaur, Ms. Pallavi Gupta, Gaurav Sharma and Dr. Mani Mahajan, who helped in many ways in my work.

I would like to acknowledge Mr. Puroshottam, Mr. Vijay, Mr. Inder Mani Mishra, Mrs. Parveen, Mrs Neelam Sidana and Mr. Jant Singh, for their kind help and support at their part.

I am thankful to my mother in law **Mrs. Krishna Devi** and father in law **Mr. Gian Chand Garg,** for their support, encouragement, care, understanding and creation of a pleasant atmosphere for me during my Ph.D work.

I owe thanks to a very special person, my husband, **Mr. Puneet Garg**, for his continued and unfailing love, support and understanding during my pursuit of Ph.D degree. The completion of the work was not possible without his help. He made many sacrifices to fulfill my dream. I greatly value his contribution. He was always beside me during my hard and happy moments.

My mother **Mrs. Nisha Singla** and father **Mr. Kewal Krishan Singla**, deserve special thanks and great appreciation for their persistent moral support, care, blessings and unconditional love. I owe everything to them. I am thankful to my brother **Mr. Honey Singla** and sister **Ms. Shivani Mittal**, who stood by me all the times.

Above all, I thank the Almighty for giving me the patience and strength to work through all these years.

(Pooja Singla)

ABSTRACT

Photocatalysis is a series of light induced advanced redox reaction processes resulting in the degradation of organic pollutants in presence of oxygen and water. Photocatalytic degradation has attracted considerable attention in the field of waste water treatment due to its capacity to destroy contaminants under mild conditions. However, photocatalytic reactions using the traditional TiO_2 photocatalyst suffer from low energy efficiencies under solar irradiation. The low efficiency in the utilization of solar energy lies in its ability to absorb visible light and the high recombination rate of electron-hole pairs. This research is focused on the design of undoped and visible light active transition metals doped TiO_2 photocatalysts. These photocatalysts are used for the photocatalytic degradation of phthalate esters. Phthalate esters are the emerging organic pollutants having very harmful effects on human health.

In the present work, undoped TiO_2 nanoparticles of different sizes are prepared via sol gel method at different calcination temperatures. Doping of Fe, Cu and Ni metal into TiO_2 is done, separately using sol-gel technique. Doping is confirmed by characterizing the nanoparticles and the changes observed in their results. Doped samples show enhanced photocatalytic activity as compared to undoped TiO_2. The codoping of Fe and Cu into TiO_2 is also done. The structural, optical and thermal properties of the samples are investigated by X-ray diffraction (XRD), UV-Vis diffuse reflectance spectroscopy (DRS), Fourier transform infrared spectroscopy (FTIR), Raman spectroscopy, Thermogravimetric analyser (TGA), High resolution transmission electron microscopy (HRTEM) and photoluminescence (PL) techniques. All the prepared samples (doped and codoped) have shown better degradation of diethyl phthalate compared to unoped sample.

LIST OF PUBLICATIONS

- Pooja Singla, Manoj Sharma, O.P. Pandey, K. Singh, Photocatalytic degradation of azo dyes using Zn doped and undoped TiO_2 nanoparticles, **Appl Phys A** (2014) 116:371-378.
- Pooja Singla, O.P. Pandey and K. Singh, Study of Photocatalytic degradation of environmentally harmful diethyl phthalate using Ni doped TiO_2 nanoparticles, **Int J Environ Sci Technol** (2016) 13:849-856.
- Pooja Singla, O.P. Pandey and K. Singh, Study on photocatalytic degradation of diethyl phthalate using anatase-brookite heterojunction, **New J Chem (Communicated).**
- Pooja Singla, O.P. Pandey and K. Singh, Enhanced photocatalytic degradation of diethyl phthalate using Zn doped rutile TiO_2. **Indian J Pure Appl Phys (Accepted).**
- Rajinder Kaur, Pooja Singla and K. Singh, Photocatalytic degradation of diethyl phthalate using undoped and transition metals doped TiO_2 nanoparticles. **Int J Environ Sci Technol (Accepted).**
- Pooja Singla, O.P. Pandey and K. Singh, Enhanced photocatalytic activity of (Fe, Cu) codoped TiO_2 nanoparticles, **Int J Environ Sci Technol (Communicated).**

<u>Publications in Non-SCI Journals</u>

- Pooja Singla, Manoj Sharma, O.P. Pandey and K. Singh, Synthesis and characterization of Zn doped nano TiO_2 for efficient photocatalytic degradation of Eriochrome Black T, AIP Conf. Proc. 1536 (2013) 103-104.
- Pooja Singla, O.P. Pandey and K. Singh, Photocatalytic degradation of diethyl phthalate using TiO_2 nanoparticles, AIP Conf. Proc. 1591 (2014) 377-378.

PAPERS PRESENTED IN CONFERENCES

1. Pooja Singla, Manoj Sharma, O.P. Pandey and K. Singh, Synthesis and characterization of Zn doped nano TiO_2 for efficient photocatalytic degradation of Eriochrome Black T, *International conference on recent trends in applied Physics and Materials Science (RAM-2013) at Govt. College of engineering and technology, Bikaner, Feb. 1-2, (2013)* (Poster presented).

2. Pooja Singla, O.P. Pandey and K. Singh, Photocatalytic degradation of diethyl phthalate using TiO_2 nanoparticles, *DAE SSPS symposium, Thapar University Patiala, Dec. 17-21, (2013)* (Poster presented).

INDEX

LIST OF FIGURES

Chapter 5

Chapter 6

LIST OF TABLES

PREFACE

The present thesis deals with the synthesis and characterization of undoped and transition metal doped TiO_2 nanoparticles for the photocatalytic degradation of phthalate esters. The entire work is divided into seven chapters.

Chapter 1 describes the general introduction of the present work. It gives the information about the conventional methods used for the degradation of organic pollutants. The advantages of heterogeneous photocatalytic degradation technique over other processes are given. A brief introduction of TiO_2 and its application in photocatalysis is also provided. The importance of doping and codoping of transition metals into TiO_2 for improving its efficiency is discussed. The motivation of choosing phthalate esters for degradation is also described.

Chapter 2 gives the detailed account of the literature survey in the context of the degradation of phthalate esters. The work done on the degradation of phthalate esters by various conventional methods and advanced oxidation processes has been presented in this chapter. In the last section of this chapter, gaps in the study along with the aims and objectives of work are presented.

Chapter 3 gives the details of synthesis procedure used to prepare undoped and transition metal doped TiO_2 nanoparticles. Details of different techniques which have been used to characterize as prepared samples like X-ray diffraction (XRD), UV-vis diffuse reflectance spectroscopy (DRS), Fourier transform infrared spectroscopy (FTIR), Thermogravimetric analysis (TGA), Raman spectroscopy, Photoluminescence (PL) and High resolution transmission spectroscopy

(HRTEM) has been provided. The setup used to perform photocatalytic experiments has been given at the end of the chapter.

Chapter 4 deals with studies of structural, optical and thermal properties of TiO_2 nanoparticles prepared via sol-gel method followed by calcination at different temperatures (200 ^oC to 400 ^oC). The photocatalytic activity of the samples is discussed in light of the degradation of diethyl phthalate.

Chapter 5 describes the synthesis of undoped, Fe-doped, Cu-doped and (Fe, Cu) codoped TiO_2 nanoparticles prepared via sol-gel method. The enhanced photocatalytic activity of (Fe, Cu) codoped TiO_2 nanoparticles as compared to undoped and mono doped TiO_2 nanoparticles is discussed by comparing their results.

Chapter 6 gives the details of undoped and Ni doped TiO_2 nanoparticles synthesized by the sol-gel technique. The optimum concentration of nickel for the highest photocatalytic activity is determined.

Chapter 7 gives the conclusions and future scope of the work. Different sized TiO_2 nanoparticles are obtained by varying calcination temperature. TiO_2 nanoparticles having smallest size show highest photo catalytic activity. The enhanced visible light photocatalytic activity of (Fe, Cu) codoped sample as compared to other samples is obtained. The optimum concentration of nickel for highest photocatalytic activity is obtained to be 0.6 mol %.

Chapter 1
Introduction

Overview

The present chapter introduces the problem of water pollution due to organic pollutants like phthalate esters. The physical/chemical properties, applications and effects on human health of phthalate esters are discussed in detail. Various conventional methods used for removal of phthalate esters from the waste water are given. Details of advanced oxidation processes like heterogeneous photocatalytic degradation and its advantages over conventional methods for degradation of phthalate esters have been given. Mechanism of photocatalytic degradation of organic pollutants using TiO_2 as photocatalyst has been discussed. Advantages of taking TiO_2 as photocatalyst in comparison to the other photocatalysts have been explained. Doping and codoping of TiO_2 with transition metals has been discussed to improve the photocatalytic activity of TiO_2. At the end of the chapter, the importance of nanostructured TiO_2 in comparison to bulk TiO_2 has been given for photocatalytic degradation.

Water pollution is one of the most serious ecological threats faced by all the nations in the world. Industrial, pharmaceutical, agricultural and domestic effluents contain a large number of pollutants. These pollutants adversely affect the human health and the environment through contamination of drinking water supplies. According to world health organization, more than one billion people lack access to clean drinking water [1]. The latest report of United Nations Environment Programme (UNEP, June 2016) has mentioned that water pollution increased after 1990s in the many rivers of Latin America, Africa and Asia [2]. Effective removal of persistent pollutants particularly organic from waste water effluents has become a challenge. The most common organic pollutants include dyes, pesticides, insecticides, herbicides, chlorinated hydrocarbons, phenols, phthalate esters etc. [3, 4]. Persistence and continuous introduction of these pollutants into the environment make the conditions worse. For example, recently Comptroller and the Auditor General of India (CAG) in its report in July 2016, says that the water of Brahmaputra river is not fit to drink even after traditional treatment as total coliform (TC) level is far above the standard norm due to organic pollution. Thus, there is an urgent need to develop environmentally harmonious, ecologically safe and sustainable chemical technologies to purify the waste water.

1.1 Phthalate esters

1.1.1 Physical / chemical properties

Phthalate esters are the esters of the phthalic acid (1,2- benzenedicarboxylic acid). Fig. 1.1 shows the chemical structure of phthalate esters where R and R^1 are alkyl groups. Most of the phthalate esters are colorless and odorless sticky liquids at room temperature. Phthalate esters, except dimethyl phthalate (5 ^{o}C) and diundecyl phthalate (– 9 ^{o}C), have melting point below – 25 ^{o}C.

The boiling point of phthalate esters lies between 230 ^{o}C to 486 ^{o}C [5]. The water solubility of phthalate esters varies inversely with the length of alkyl chain. Phthalate esters are highly conjugated systems having pi-cloud on the benzene ring, the lone pairs on the oxygens and the p-orbitals on the carbonyl atoms are all conjugated. The substituents are meta-directing and they are ortho to each other, so all positions in the ring are more or less equally deactivated. Due to conjugation, these are stable compounds [6].

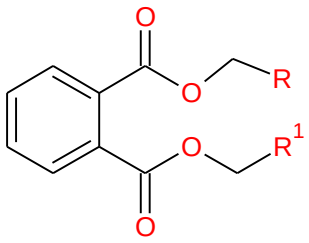

Figure 1.1: Chemical structure of phthalate esters.

1.1.2 Applications and human exposure

Phthalate esters are mainly used as plasticizers to improve the flexibility and longevity of the plastics. Due to low melting point and high boiling point, phthalate esters can be used as heat transfer fluids, plasticizers and carriers [5]. When phthalate esters are incorporated to the polymer matrix; the glass transition temperature of the polymer decreases [7]. Having excellent compatibility with the polymers, phthalate esters reduce the intermolecular forces and viscosity of polymers after entering the polymer matrix without any chemical reaction [5]. Short chain phthalates like dimethyl phthalate and dibutyl phthalate, are used in creams, nail polishes, baby lotions, aerosols, cosmetics, house fragrances, medical products etc. [8]. Long chain phthalate esters such as butyl benzyl phthalate, di-n-hexyl phthalate, di-2-ethylhexyl phthalate, di-n-octyl phthalate, di-iso-nonyl phthalate, di-iso-decyl phthalate are frequently used as plasticizers in polyvinyl chloride plastics, lubricants, adhesives, paints, printing inks, children toys, wallpapers,

flooring, food packaging films, medical products, table cloths, electronics etc. [8, 9]. The production of phthalate esters is increasing rapidly. It was 1.8 million tons in 1975, 6.2 million tons in 2009 and more than 8 million tons in 2011. Presently, nearly 80% of annual production of phthalate esters is used as plasticizers, especially for making of polyvinylchloride (PVC) [9].

Phthalate esters are not chemically bonded to the polymers; they can easily migrate to the surface of the polymer where they may be lost by variety of physical processes [7]. Phthalate esters are slowly released from industrial products during manufacturing, storage, use, and disposal [9]. The exposure of phthalate esters to the humans occurs through food, water, air and skin absorption. Phthalate esters have been found in urine, amniotic fluid, saliva, blood, breast milk and cord blood in humans during investigations [10]. Phthalate esters are present in measurable concentrations in the different environments worldwide.

1.1.3 Phthalates and human health

Phthalate esters are the endocrine disrupting chemicals. The clinical and experimental studies indicate that even small amounts of phthalate esters affect the biological processes in wildlife and humans, initiating teratogenicity, mutagenicity and carcinogenicity [9]. Phthalate exposure in men has been associated with hypospadias, gynecomastia, abnormal spermiogram and sperm DNA damage, cryptorchidism and abnormal levels of prolactin, LH, FSH, testosterone, free androgen index, estradiol, and sex hormone binding globulin [8]. Phthalate exposure in women has been related with infertility, endometriosis, leiomyomas, breast cancer, high rates of miscarriage, delayed or preterm gestation, and pregnancy complications such as anemia, toxemia, and preeclampsia [8]. Raised maternal urinary concentrations of some phthalate metabolites are related to the decreased mental power, motor development and increased internalizing behaviours, decrease in psychomotor development index in female infants [11].

Phthalates exposure may lead to shorter anogenital distance (AGD) in male infants and potential early marker of reproductive toxicity in humans [11]. In some experiments, when phthalate esters are exposed to the rodents, they show many symptoms called the phthalate syndrome which can be related to the effects of phthalate exposure in human males. The phthalate syndrome in rats is characterized by malformations in male organs, cryptorchidism, retention of nipples/areolae, and reduced AGD [8, 12]. Phthalate esters are one of the most commonly found persistent organic pollutants in the environment [8]. Some of the phthalate esters are blacklisted as priority water pollutants by US Environmental Protection Agency (EPA) and the Chinese Environment Monitoring Center [9].

1.2 Degradation pathways of phthalate esters

Physical and chemical methods for the removal of phthalate esters from water include floatation, chemical coagulation, activated carbon adsorption, membrane filtration etc. [13]. Floatation is a process for separating solid particles from a liquid phase primarily to lessen ions, colloids, macromolecules, microorganisms or fibers [14]. In coagulation/flocculation process, a coagulant is added to wastewater to destabilize the colloids. This destabilization of colloids is called coagulation. The agglomeration of destabilized particles into bigger particles (flocs) is called Flocculation. The flocs can be efficiently removed by flotation or sedimentation [14]. In active adsorption method, organic and inorganic compounds are removed via adsorption phenomenon which is based on surface interactions between carbon graphitic platelet surfaces and contaminants [15]. Biodegradation is another method of degradation of phthalate esters from environment which can be aerobic or anaerobic. Biological wastewater treatment uses bacteria and other microorganisms to decompose organic contaminants. Anaerobic treatment is a process where pollutant is broken down by microorganisms in absence of dissolved oxygen while

aerobic treatment is done in presence of oxygen [16]. Limitations associated with these methods are that they are very time consuming, generate wastes during wastewater treatment and cause secondary pollution problems which require supplementary steps and expenses [17]. Furthermore, the cost for both activated carbon and membrane exchange may be significant. Biological processes are not recommended for the compounds which are resistant or toxic to microorganisms [18].

1.2.1 Advanced Oxidation Processes (AOPs)

In recent years, Advanced Oxidation Processes (AOPs) for waste water treatment are gaining considerable attention. These methods involve the formation of strong oxidizing species such as $^{\cdot}OH$ radicals. This methodology involves the removal of organic pollutants (and sometimes inorganic) from waste water by oxidation of organic pollutants with hydroxyl radicals ($^{\cdot}OH$) produced *in-situ* [19, 20]. In many cases, the organic pollutant is completely mineralized into water and carbon dioxide. AOP's such as ozonation (O_3), ozone combined with hydrogen peroxide (O_3/H_2O_2) and UV irradiation (O_3/UV) or both (O_3/H_2O_2/UV), ozone combined with catalysts (O_3/catalysts), UV/H_2O_2, Fenton, photo-Fenton processes (Fe^{2+}/H_2O_2 and Fe^{2+}/H_2O_2/UV), the ultrasonic cavitation process and photo catalysis have been successfully used for waste water treatment [20]. Among advanced oxidation processes, heterogeneous photocatalytic degradation is a promising technology to degrade organic pollutants in wastewater. This technique is advantageous over competing processes due to complete mineralization of most organic pollutants, mild temperature and pressure conditions required, environmental friendly, low cost, no secondary pollution problems and potential to treat the pollutants present in trace amounts in wastewater [21].

1.3 Heterogeneous photocatalytic degradation

Heterogeneous photocatalytic degradation is a reaction in the presence of a semiconductor photocatalysts (e.g. TiO_2 and ZnO), an energetic light source and an oxidizing agent such as oxygen or air [22]. Mechanism of photocatalytic degradation using UV light and TiO_2 is depicted in Fig. 1.2.

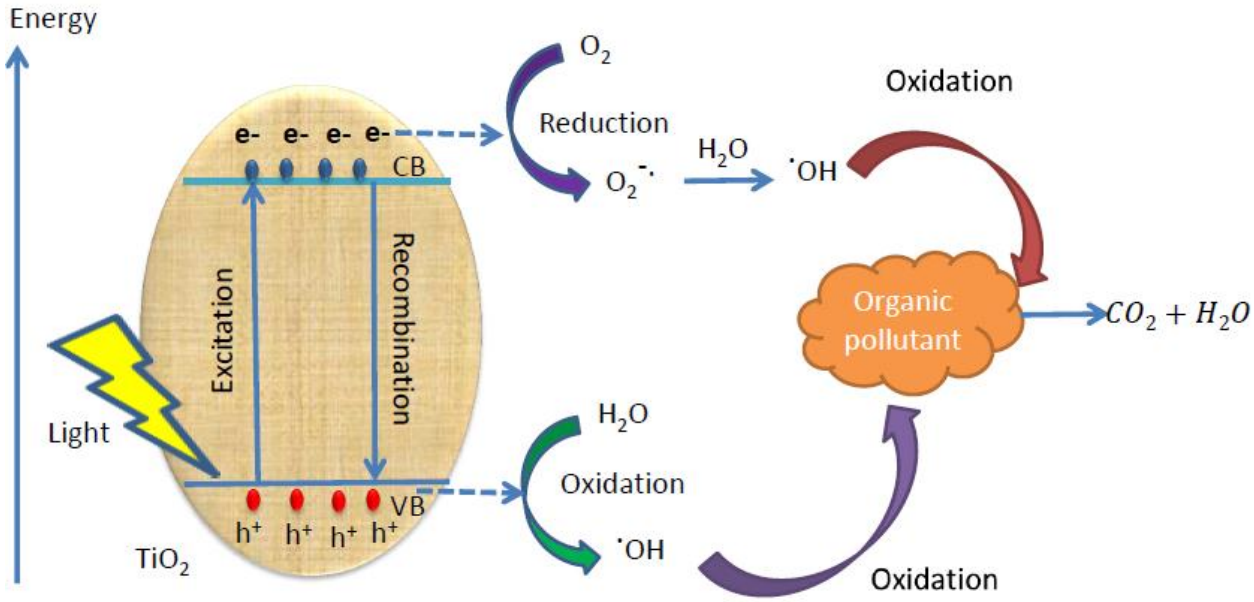

Figure 1.2: Mechanism of photocatalytic degradation of organic pollutants using TiO_2 as photocatalyst [23].

The photocatalytic reaction begins with the absorption of the photon having energy equal to or greater than the optical band gap of TiO_2 that produces an electron-hole pair on the surface of TiO_2. The electron makes a transition from valence band to the conduction band, on the other hand a positive hole is formed in the valence band. The pollutant and water gets oxidized by the positive holes, on the other hand the oxygen present on the surface of the catalyst gets reduced by the electrons in the conduction band. The superoxide ions ($O_2^{-\cdot}$) react with water to produce

hydroxyl radicals, which are very reactive and strong oxidizing agents. These produced hydroxyl radicals, break down the organic pollutant by the oxidation reactions. The reaction completes by recombination of electrons and holes [23, 24]. The parameters affecting photocatalytic degradation are properties of catalyst, catalyst dose, pH, light intensity and wavelength, initial concentration of pollutant etc. [25].

1.4 Titanium dioxide (TiO_2)

Titanium dioxide also called titania is naturally occurring oxide of titanium. TiO_2 is one of the most investigated materials because of its interesting optical and electronic properties, high stability, low cost, non-toxicity, biocompatibility, strong oxidizing power, photocatalytic activity etc. [26]. It is frequently used in environmental and energy fields, including self-cleaning surfaces, air and water purification systems, hydrogen evolution, photocatalytic CO_2 reduction into energy fuels, solar cells, supercapacitors, biomedical devices, lithium ion batteries and photo electrochemical conversion etc. [27]. TiO_2 has been considered as a suitable photocatalyst for waste water treatment. TiO_2 exists mainly in three phases namely anatase (tetragonal), rutile (tetragonal) and brookite (orthorhombic). Anatase phase of TiO_2 yields higher photocatalytic activity compared to rutile and brookite phases. However, when anatase phase coexists with small fraction of rutile and brookite, it shows enhanced photocatalytic activity than pure anatase phase due to migration of charge carriers [28]. The use of many metal oxides (TiO_2, ZrO_2, ZnO V_2O_5, WO_3, MoO_3, α-Fe_2O_3, SnO_2, $SrTiO_3$) and metal chalcogenides (ZnS, WS_2, CdSe, CdS, MoS_2) in photocatalysis reactions has been reported in the literature [29]. The positions of conduction bands (CB) and valence bands (VB) are important points in the selection of semiconductors. According to thermodynamic requirement, the positions of valence band and conduction band should be such that the redox potential of valence band holes must be

sufficiently positive to generate hydroxyl radicals and that of conduction band should be sufficiently negative to generate superoxide radicals [30, 31]. From Fig. 1.3 [29] it is clear that TiO_2, ZnO, $SrTiO_3$ and ZrO_2 exhibit favorable band gap positions as compared to other materials. The material is selected on the basis of its stability towards photocorrosion.

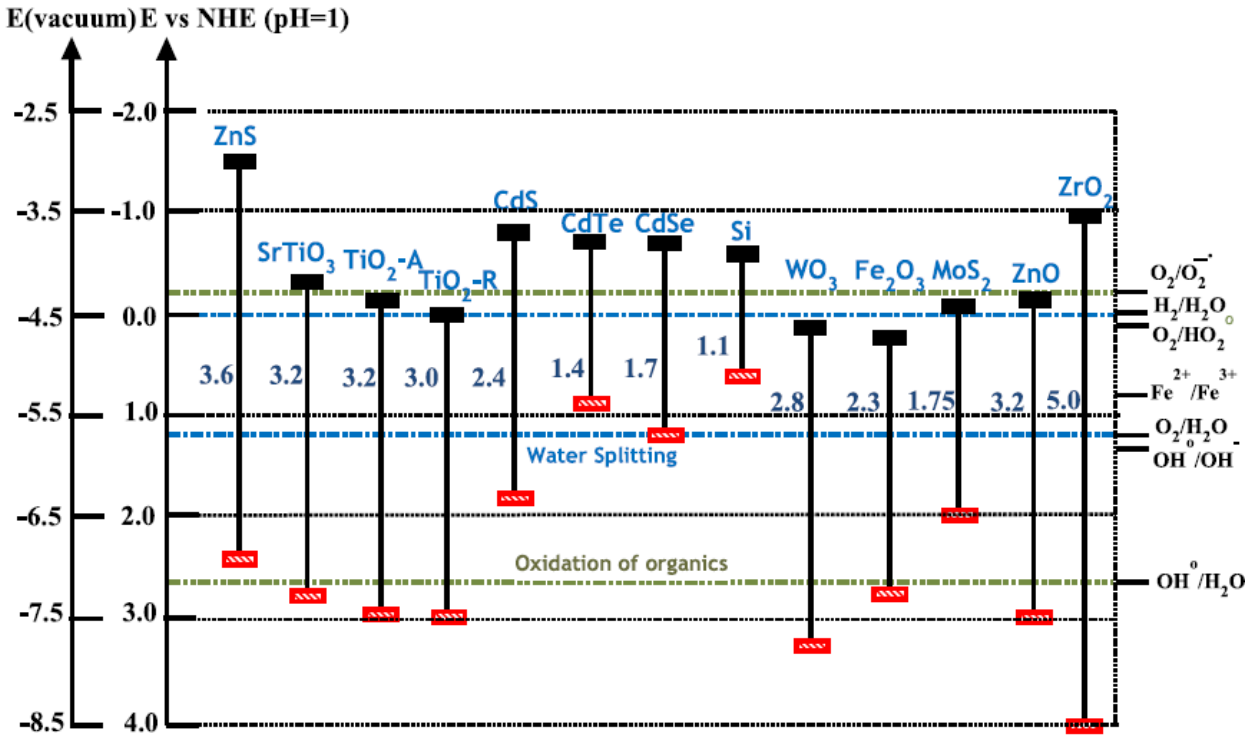

Figure 1.3: Band gap energy and band edge positions of different semiconductor oxides and chalcogenides, along with selected redox potentials [29].

For instance, ZnO and CdS exist mainly in +2 oxidation state and are susceptible to decompose by valence band holes, as follows.

$$ZnO + 2h^+ \longrightarrow Zn^{2+} + 1/2\ O_2 \qquad (8)$$

$$CdS + 2h^+ \longrightarrow Cd^{2+} + S \qquad (9)$$

ZnO undergoes inconsistent dissolution and produces $Zn(OH)_2$ on the surface. It leads to the deactivation of the material after some time. However, Ti in TiO_2 can change its oxidation state from +3 and +4 reversibly [29]. Hence, TiO_2 is preferred over the other materials. TiO_2 exists in two polymorphs namely anatase and rutile; however, anatase phase of TiO_2 having band gap energy 3.2 eV is more active for photocatalysis applications, even though rutile phase TiO_2 with a smaller band gap (3.0 eV) has the possibility to absorb at long wavelength radiation. The higher reducing power of anatase is due to its conduction band position, which is more negative as compared to rutile. Moreover, other features like optical and electronic properties, low-cost, inertness, stability, easy production and use, ability to increase the rate of reactions without any harm to environment make the TiO_2 as the photocatalyst of choice [29].

1.5 Doping and codoping of TiO_2 with transition metals

Some limitations of TiO_2 like high rate of electron-hole recombination and wide optical band gap limits its application on the commercial level using solar radiation as light source [32]. The high rate of recombination of charge carriers decreases the efficiency of photocatalytic reactions. Moreover, the wide band gap allows only UV light for photocatalytic applications which is only 3-5 % of solar spectrum [33]. Doping TiO_2 with transition metals is a promising method to make it capable to absorb the visible light and increase its photocatalytic activity. Hence, researchers have doped many transition metals like Fe, Cr, Mn, Co, Mo, Ni, Cu and Zn into TiO_2 to modify its optical band gap and photocatalytic activity [34-35]. The enhanced visible light photocatalytic activity of TiO_2 upon doping with transition metals may be explained as narrowing of the band gap, formation of impurity energy levels, formation of intrinsic defects (such as oxygen vacancies, interstitial Ti cations) and introduction of traps for electrons and/or holes. Recently, an approach to dope TiO_2 with more than one transition metal ions has attracted much attention

as it offers a better control to the tuning of band-gap [36]. Additionally, the photocatalytic activity of host material is improved as compared with single metal doping [37]. Yuan et al. [38] reported that Zn and Fe codoped TiO_2 exhibited two folds improved photocatalytic activity than undoped or single doped. Benjwal et al. [37] synthesized Zn, Mn codoped TiO_2 by sol-gel technique. The codoped samples showed higher red shift and photocatalytic activity than undoped sample. The enhancement in photocatalytic activity was due to its multiphase structure, increased absorption and the efficient transfer of electron hole pairs through co-dopant ions in the sub energy levels of TiO_2 [37].

1.6 Nanostructured titanium oxide

Nanosized TiO_2 particles are preferred for photocatalytic application than bulk TiO_2. The physical and chemical properties of the materials vary when their size approaches the nanoscale [39]. The chemical activity of heterogeneous catalysts is directly related to its specific area per unit volume. Surface area increases when the size is reduced from bulk to nanoscale. This confirms improved rate of reaction because of increased interaction between the reactants and the active sites. The unexpected optical properties of nanoparticles are due to their size which is small enough to produce quantum effects [40]. Sol-gel is one of most preferred method of synthesizing undoped, single doped or codoped TiO_2 nanoparticles. This method has many advantages over the competing methods, such as low temperature synthesis of highly pure nanosized powders, better control on stoichiometry, synthesis of homogeneous and composite materials [41]. These benefits have motivated many researcher groups to employ this technique to synthesize TiO_2 based photocatalysts.

1.7 Conclusive Remark

Water pollution due to organic pollutants is a serious concern for human health. Endrocrine disruptors like phthalate esters, present in drinking water supplies cause serious reproductive, and neurological disorders. Waste water effluents need to be treated before disposal. Conventional waste water treatment cause secondary pollution problems, are time consuming and costly. Hetrogenous photocatalytic degradation using TiO_2 based photocatalysts, is a promising technology for complete mineralization of organic pollutants in lesser time, under normal conditions with no secondary pollution. Undoped TiO_2 cannot use solar radiation as light for degradation of organic pollutants due to wide band gap and low quantum efficiency because of high recombination of eletron hole pairs. These limitations can be efficiently overcomed by doping and codoping of transition metal ions so that this process can be used for practical applications. Synthesis of such photocatalysts which can use renewable sources like solar energy for solving pollution problems effciently can be a great contribution to the society.

A detailed literature work has been carried out which is given in next chapter describing the synthesis of undoped and doped TiO_2 nanoparticles by various methods and their effect on the properties such as structural, optical and photocatalytic properties. The literature work describes the use of undoped and doped TiO_2 nanoparticles for the degradation of various organic pollutants.

References

1. R.J. Ramirez, C.A.P. Arellano, J.C. Varia, S.S. Martinez, Curr Org Chem 19 (2015) 540.
2. UNEP 2016. A Snapshot of the World's Water Quality: Towards a global assessment. United Nations Environment Programme, Nairobi, Kenya.162pp.
3. S. A. Saber, M.G. Rasul, Desalination 261 (2010) 3.
4. R.S. Thakur, R. Chaudhary, C. Singh, J Renew Sustain Ener 2 (2010) 1.
5. J. Yang, Y. Li, Y. Wang, J. Ruan, J. Zhang, C. Sun, Trends Analyt Chem 72 (2015) 10.
6. J.J. Maitland, Organic chemistry (2005) W.W. Nortan & Company NewYork.
7. C.A. Staples, The Handbook of Environmental Chemistry (2003) Springer New York.
8. I.A. Sheikh, R.F. Turki, A.M. Abuzenadah, G.A. Damanhouri, M.A. Beg, PLOS One 10 (2016) 13.
9. D.W. Gao, Z.D. Wen, Sci Total Environ 541 (2016) 986.
10. R. Mankidy, S. Wiseman, H. Ma, J.P. Giesy, Toxicol Lett 217 (2013) 50.
11. T.E. Arbuckle, K. Davis, L. Marro, M. Fisher, M. Legrand, A. LeBlanc, E. Gaudreau, W.G. Foster, V. Choeurng, W.D. Fraser, Environ Int 68 (2014) 55.
12. C. Wang, L. Yang, S. Wang, Z. Zhang, Y. Yu, M. Wang, M. Cromie, W. Gao, S.L. Wang, Sci Rep 6 (2016) 19982.
13. M.M. Abdel daiem, J. Rivera-Utrilla, R. Ocampo-Perez, J.D. Mendez-Díaz, M. Sanchez-Polo, J Environ Manage 109 (2012) 164.
14. N.B. Prakash, V. Sockan, P. Jayakaran, Int J Eng Sci Innov Technol 3 (2014) 479.
15. T. Robinson, G. McMullan, R. Marchant, P. Nigam (2001) Bioresour Technol 77 (2001) 247.

16. U. Wiesmann, I. S. Choi, E. Dombrowski, Fundamentals of Biological Wastewater Treatment (2006) Wiley-VCH Verlag GmbH & Co. KGaA Weinheim.
17. S. Ahmed, M.G. Rasul, W.N. Martens, R. Brown, M.A. Hashibd, Desalination 261 (2010) 3.
18. E. GilPavas, I. Dobrosz-Gómez, M. Á. Gómez-García, Water Sci Tech 63 (2011) 385.
19. M.A. Rauf, M.A. Meetani, S. Hisaindee, Desalination 276 (2011) 13.
20. B. Bethi, S.H. Sonawane, B.A. Bhanvase, S. Gumfekar, (2016) Chem Eng Process 109 (2016) 178.
21. A. O. Ibhadon, P. Fitzpatrick, Catalysts 3 (2013) 189.
22. C.M. Teh, A.R. Mohamed, J Alloys Compd 509 (2011) 1648.
23. J. Schneider, M. Matsuoka, M. Takeuchi, J. Zhang, Y. Horiuchi, M. Anpo and D.W. Bahnemann, Chem Rev 114 (2014) 9919.
24. A. Ajmal, I. Majeed, R. N. Malik, H. Idrissc, M. A. Nadeem, RSC Adv 4 (2014) 37003.
25. U.G. Akpan, B.H. Hameed, J Hazard Mater 170 (2009) 520.
26. S. Banerjee, S.C. Pillai, P. Falaras, K.E. O'Shea, J.A. Byrne, D. Dionysios, D. Dionysiou J Phys Chem Lett 5 (2014) 2543.
27. M. Ge, C. Cao, J. Huang, S. Li, Z. Chen, K. Q. Zhang, S.S. Al-Deyab, Y. Lai, J Mater Chem A 4 (2016) 6772.
28. G. Tian G, H. Fu, L. Jing, C. Tian, J Hazard Mater 161 (2015) 1122.
29. R. Vinu, G. Madras, J Indian Inst Sci 90 (2010) 189.
30. K. Kabra, R. Chaudhary, R.L. Sawhney, Ind Eng Chem Res 43 (2004) 7683.
31. A. Kudo, Y. Miselki, Chem Soc Rev 38 (2009) 253.
32. L. Agartan, D. Kausuz, J. Park, A. Ozturk, Ceram Int 41 (2015) 12788.

33. S. Wang, J.S. Lian, W.T. Zheng, Q. Jiang, Appl Surf Sci 263 (2012) 260.

34. A. Zaleska, Recent Pat Eng 2 (2008) 157.

35. B. Liu, H.M. Chen, C. Liu, S. C. Andrews, C. Hahn, P. Yang, J Am Chem Soc 135 (2013) 9995.

36. V. Etacheri, C.D. Valentin, J. Schneider, D. Bahnemann, S.C. Pillai, J Photochem Photobiol C 25 (2015) 1.

37. P. Benjwal, K. K. Kar, RSC Adv, 5 (2015) 98166.

38. Z. Yuan, J. Jia, L. Zhang, Mater Chem Phys 73 (2002) 323.

39. P. Praveen, G. Virthagiri, S. Mugundan, N. Shanmugam, Spectrochim Acta Mol Biomol Spectrosc 117 (2014) 622.

40. M. Zimmermann, B.Temel, G. Garnweitner, Chem Eng Process 74 (2013) 83.

41. U.G. Akpan, B.H. Hameed, Appl Catal A 375 (2010) 1.

Chapter 2
Literature Review

Overview

This chapter presents the detailed literature survey related to the degradation of phthalate esters. The use of various techniques like biological methods, conventional methods (floatation, chemical coagulation, activated carbon adsorption, membrane filtration etc.) and advanced oxidation techniques (ozonation (O_3), ozone combined with hydrogen peroxide (O_3/H_2O_2) and UV irradiation (O_3/UV) or both (O_3/H_2O_2/UV), ozone combined with catalysts (O_3/catalysts), UV/H_2O_2, Fenton, photo-Fenton processes (Fe^{2+}/H_2O_2 and Fe^{2+}/H_2O_2/UV), the ultrasonic cavitation process and photo catalysis) by the researchers for the degradation of phthalate esters in different studies is reviewed. This chapter completes by giving the motivation for the present work, based on some gaps in the above study.

The industrialization and urbanization has led to the release some complex and refractory organic pollutants like phthalate esters in the environment. It has become an urgent need to develop novel technologies for the removal of these types of pollutants. Phthalates and their metabolites are harmful for human and environment because of hepatotoxic, teratogenic and carcinogenic features **[1]**. There are numerous methods available for removing phthalate esters from the environment. In order to understand the work done for the degradation of phthalate esters, detailed literature survey has been done and presented in this chapter. The treatments used for the degradation of phthalate esters have been classified into three categories i.e. (i) physical/chemical treatments (ii) biological treatments (iii) advanced oxidation processes.

2.1 Physical/chemical treatments

Physical and chemical processes to remove of phthalate esters from waste water include floatation, chemical coagulation, flocculation, activated carbon adsorption, membrane filtration etc. **[2]**. Ayranci et al. **[3]** reported the adsorption behavior of phthalic acid and its esters on high area activated carbon cloth. Mohan et al. **[4]** investigated the adsorptive removal of diethyl phthalate (DEP) from aqueous phase on activated carbon. Results showed that DEP sorption was dependent on pH of aqueous phase and uptake was higher at acidic pH. Zhang et al. **[5]** studied the removal of phthalate esters and dissolved organic matter from landfill leachate by complexation- flocculation. Zheng et al. **[6]** investigated the viability of removing phthalate esters from fresh and partially stabilized landfill leachates by a coagulation and flocculation process. The results showed that 30 % of phthalate esters in fresh leachate could be removed. Salim et al. **[7]** studied the adsorption behavior of phthalate esters on chitosan beads. Zheng et al. **[8]** removed dioctyl phthalate (DOP) from water through flocculation process with polyacrylamide flocculant. Boonorat et al. **[9]** studied the phthalate ester degradation in

membrane bioreactor treating (MBR) municipal landfill leachate. The operation of MBR using municipal landfill leachate with C/N of 6 and solid retention time (SRT) of 90 days were optimum for the treatment of organic and nitrogen removals as well as the biodegradation of phthalate esters. The elimination of small amounts of phthalate esters from water by thin film composite nanofiltration hollow fiber membranes was investigated by Wei et al. **[10]**. The results showed that hydrophobic adsorption and steric hindrance play important role in phthalates removal.

2.2 Biological treatments

Biodegradation is widely studied method for the removal of phthalate esters from the environment. Phthalate esters can be degraded by fungi and bacteria under aerobic, anaerobic and anoxic conditions. In general, phthalate esters with shorter alkyl chain are more easily biodegraded than the higher alkyl chain phthalate esters in wastewater treatment processes [1]. Moreover, long chain phthalate esters have a strong capacity to adsorb onto suspended matter. Biological degradation studies of phthalate esters revealed that phthalate esters could take several days to several months for degradation. The problem of secondary pollution is also associated with biological methods.

Shelton et al. **[11]** reported biodegradation of six phthalate esters in anaerobic sludge. Two high molecular phthalate esters i.e. di-n-octyl phthalate and di-(2-ethylhexyl) phthalate were not degraded. On the other hand, dimethyl phthalate, diethyl phthalate, di-n-butyl phthalate were degraded within one week. Wang et al. **[12]** investigated the microbial degradation of phthalate esters (dimethyl phthalate, di-n-butyl phthalate and di-n-octyl phthalate) by acclimated sludge. Percentage degradation of dimethyl phthalate and di-n-butyl phthalate was 90 % in 3 days and 8

days, respectively. Degradation rate of di-n-octyl phthalate was very slow. Jianlong et al. **[13]** studied the anaerobic degradation of three phthalate esters in a digested sludge. The degradation rates were higher for small alkyl chain phthalate esters as compared to long chain phthalate esters. The degradation of phthalate esters using two aerobic bacteria stains i.e. DK4 and O18 isolated from a river sediment and petrochemical sludge, respectively was investigated by Chang et al. **[14]**. Short alkyl chains phthalate esters were easily degraded but long alkyl chain phthalate esters were poorly degraded with bacterial stains. Pakau et al. **[15]** reported that di-(2-ethylhexyl) phthalate (DEHP) in sewage sludge decreased continuously during aerobic composting. The removal efficiency of DEHP was 97 % after 20 days. The biodegradation of phthalate esters mixture in aqueous phase using a newly isolated bacterial strain namely, Variovorax sp was carried out **[16]**. The bacterial strain was able to degrade >99% of 300 mg L^{-1} phthalate esters in 30 h. The biodegradation of diethyl phthalate (DEP) and di-n-butyl phthalate (DBP) by three marine algae namely *Cylindrotheca closterium*, *Dunaliella salina*, *Chaetoceros muelleri*. *Cylindrotheca closterium* was found to be the most effective **[17]**. The degradation efficiency of diethyl phthalate and dibutyl phthalate using *Cylindrotheca closterium* after 168 hours was 81.2% and 93.1%, respectively. Wang et al. [18] investigated the degradation of three isomers dimethyl phthalate ester by red marine yeast *Rhodotorula mucilaginosa* isolated from deep sea sediments of the Atlantic Ocean. The yeast didn't mineralize the phthalate esters completely but it transformed them to their metabolites which were found to be resistant for further degradation. Ahuactzin-Perez et al. **[19]** investigated the biodegradation of di (2-ethyl hexyl) phthalate using fungus *F. culmorum*. F. culmorum degraded 95% of di (2-ethyl hexyl) phthalate (1000 mg/L) within 60 h of growth.

2.3 Advanced oxidation processes

Advanced oxidation processes have attracted much attention for treating organic pollutants in waste water. Advanced oxidation processes include various processes such as ozonation (O_3), ozone combined with hydrogen peroxide (O_3/H_2O_2) and UV irradiation (O_3/UV) or both (O_3/H_2O_2/UV), ozone combined with catalysts (O_3/catalysts), UV/H_2O_2, Fenton, photo-Fenton processes (Fe^{2+}/H_2O_2 and Fe^{2+}/H_2O_2/UV), the ultrasonic cavitation process, semiconductor photo catalysis etc. **[20]**. In advanced oxidation processes, the organic pollutants are being oxidized by $^{\cdot}OH$ radicals produced *in-situ*, leading to degradation of the pollutants. The fast reaction rates and non-selective oxidation are the main benefits of advanced oxidation processes **[21]**. The work done by various researchers for the degradation of phthalate esters using advanced oxidation processes is presented below in Table 2.1.

Table 2.1: Summary of degradation of phthalate esters by various advanced oxidation processes.

S.No.	Advanced Oxidation process used	Phthalate ester degraded	Investigations and Outcomes	Citation
1	Photocatalytic degradation using Degussa P25 and Hombikat UV 100 as photocatalysts	diethyl phthalate	• The degradation rates were highest for Degussa P25 at pH 6. • The additional electron acceptors enhanced the overall mineralization.	Muneer et al. **[22]**
2	Photocatalytic degradation using Fe (III) aquacomplexes under solar irradiation	diethyl phthalate	• The hydroxyl radicals responsible for the degradation of diethyl phthalate were generated through an intermolecular photoredox process in the excited state of Fe^{3+} aquacomplexes. • The degradation photoinduced by Fe^{3+} appeared to be an efficient method for removal of diethyl phthalate.	Mailhot et al. **[23]**
3	Sonochemical degradation at ultrasonic frequency of 80 kHz	di-n-butyl phthalate, butyl benzyl phthalate, di-(2-ethyl hexyl) phthalate, di-n-octyl phthalate, dimethyl phthalate, diethyl phthalate	• Ultrasonic treatment was able to remove high molecular weight phthalates but low molecular weight phthalates got recalcitrant. • To remove them, solid phase micro extraction technique was coupled with GC-MS technique.	Psillakis et al. **[24]**
4	Photocatalytic degradation using four types of TiO_2 pillared clays (fluorine mica, fluorine hectorite, montmorillonite, saponite)	di-n-butyl phthalate and dimethyl phthalate	• The variation of surface hydrophobicity of TiO_2 pillared clays with the host clay followed the trend: saponite < fluorine hectorite < montmorillonite < fluorine mica. • The trend of degradation and adsorption of phthalate ester was in agreement with the surface hydrophobicity	Ooka et al. **[25]**
5	UV irradiation coupled with Fenton reaction	diethyl phthalate	• The maximum degradation percentage was 75.9 % in 120 min at pH 3 in $UV/H_2O_2/Fe^{3+}$ system.	Yang et al. **[26]**

6	TiO_2 immobilized on glass beads initiated by UV irradiation (UV/TiO_2/glass)	di-n-butyl phthalate (DBP)	• This system yielded 75 % degradation efficiency of DBP with initial concentration of 5 mg/L in 80 min. • The effect of pH was found to be negligible on degradation rate when pH range was 4.5-9	Chiou et al. **[27]**
7	Photocatalytic degradation using TiO_2 powder	di-n-butyl-ortho-phthalate	• Gas chromatography technique was used for determining the intermediates. The final degradation product was carbon dioxide.	Kaneco et al. **[28]**
8	UV/H_2O_2 process	diethyl phthalate	• DEP was not effectively removed using UV irradiation and H_2O_2 alone. The combined UV/H_2O_2 effectively removed the diethyl phthalate. • With initial concentration of 1.0 mg/L, more than 98.6 % DEP was removed in 60 min under UV irradiation (133.9 $\mu W/cm^2$).	Xu et al. **[29]**
9	Ozonation using Ru/Al_2O_3 as catalyst	dimethyl phthalate	• TOC removal efficiency was greatly enhanced in presence of Ru/Al_2O_3. • TOC removal was 72 % in presence of Ru/Al_2O_3 which was only 15 % for direct ozonation.	Yunrui et al. **[30]**
10	Photocatalytic degradation using aqueous TiO_2 (Degussa, P25) suspension under UV irradiation using Ferrate (VI) and oxygen (O_2) as electron acceptors	dimethyl phthalate	• Fe (VI) was found to be a better electron acceptor than O_2 for scavenging conduction band electrons. • Dimethyl degradation in presence of O_2 followed a different pathway than in presence of Fe (VI). • Radicals generated in TiO_2-UV-O_2 were proposed to react with the aromatic ring while radicals generated in TiO_2-UV-Fe (VI) were proposed to react with the alkyl chain of	Yuan et al. **[31]**

			phthalate ester.	
11	Combined ferrate-photocatalysis (Fe (VI)-TiO_2-UV)	dimethyl phthalate	• The behavior of this process was compared in presence and absence of dissolved oxygen at pH 9. • Dimethyl phthalate degradation was inhibited in oxygen flow than nitrogen gas flow due to formation of Fe-O- (organic) complexes.	Yuan et al. **[32]**
12	Photocatalytic degradation using TiO_2 pillared montmorillonites	dimethyl phthalate	• TiO_2 pillared montmorillonites were prepared by introducing Ti^{4+} into a layer of montmorillonites modified with or without cetyltrimethylammonium bromide. • Hydrophobic TiO_2 pillared montmorillonites showed better photocatalytic performance than hydrophilic one.	Ding et al. **[33]**
13	Photo Fenton treatment coupled with biological system	di-(2-ethylhexyl) phthalate	• Parameters like concentrations of DEHP, Fe^{3+}, H_2O_2 and the reaction time affected the degradation efficiency. • The optimal time was 60 min for the pretreatment Fenton process and introduction into the biological system. • The wastewater pretreated by photo Fenton process was biodegradable. The mineralization was completed when wastewater was subsequently treated in biological system.	Chen et al. **[34]**
14	Photocatalytic degradation using TiO_2-coated magnetic poly (methyl methacrylate) (TiO_2/mPMMA) and platinum-doped TiO_2/mPMMA (Pt–TiO_2/mPMMA) microspheres	dimethyl phthalate	• Pt–TiO_2/mPMMA microspheres showed enhanced photocatalytic activity than the TiO_2/mPMMA microspheres, especially in terms of mineralization efficiency.	Chen et al. **[35]**
15	Photocatalytic degradation using composite of TiO_2 particle core and a	diethyl phthalate	• The composite showed higher photocatalytic activity as compared to pure Degussa P25.	Shen et al. **[36]**

	shell layer of Al^{3+}-doped 5 nm thick silica			
16	Electrochemical degradation at boron doped diamond (BDD) anode and platinum anode	dimethyl phthalate, diethyl phthalate, dipropyl phthalate, dibutyl phthalate, dihexyl phthalate, diheptyl phthalate, dioctyl phthalate	• The degradation and mineralization of phthalate esters was higher at BDD anode than Pt-anode owing to large amount of strong oxidants as free hydroxyl radicals in the system. • With increasing alkyl length chain of phthalate esters, degradation rates became higher at Pt anode than BDD anode due to different oxidation mechanism associated at two anodes.	Li et al. **[37]**
17	Photocatalytic degradation using TiO_2	diethyl phthalate	• The major intermediates determined by gas chromatography-mass spectrometry technique (GC-MS) were ethyl benzoate, methyl benzoate and carboxylic derivatives. • The photocatalytic degradation reaction followed first-order kinetics. The degradation efficiency increased with lower and higher pH due to base and acid catalyzed hydrolysis.	Huang et al. (2010) **[38]**
18	Electrochemical oxidation process using Pd/C gas-diffusion electrode as cathode and $Ti/IrO_2/RuO_2$ as anode	diethyl phthalate	• The cathode generated H_2O_2 through two electron reduction of fed oxygen molecule in the electrolysis. • Hydroxyl radical was determined by electron spin resonance spectrum. The percentage removal of DEP was 80 % after 9 h electrolysis.	Wang et al. **[39]**
19	Photocatalytic degradation using polyoxotungstate/titania nanocomposites	di-n-butyl phthalate (DBP), diethyl phthalate (DEP), and dimethyl phthalate (DMP)	• The degradation of DBP, DEP, and DMP reached to 98%, 84%, and 80%, respectively, after the simulated sunlight irradiation. • Nearly total mineralization of DBP and DEP was obtained in 12h.	Xu et al. **[40]**

			• It was mainly attributed to the adsorption behaviors of PAE molecules on the PW12/TiO2 composites; the synergistic effect existed between the Keggin unit and TiO_2 network; and quantum size effect of the composites	
20	Ozonation using Fe/SBA-15 as catalyst. SBA-15 is ordered mesoporous molecular sieve with narrow pore size distribution and large surface area	dimethyl phthalate	• The rate constant using Fe/SBA-15 was .0059 min^{-1} which was much higher than ozonation alone and SBA-15/O_3 process. • The mineralization of dimethyl phthalate followed first order kinetics.	Huang et al. **[41]**
21	Photocatalysis combined with UV irradiation and ozonation (TiO_2/UV/O_3)	dimethyl phthalate	• This combined effect showed enhanced degradation efficiency for dimethyl phthalate as compared to the photocatalysis combined with UV irradiation (TiO_2/UV), ozonation combined with UV irradiation (UV/O_3), and ozonation alone (O_3)	Jing et al. **[42]**
22	Oxidative degradation using Fenton process	Diethyl hexyl phthalate	• Maximum 85.6% degradation of DEHP was observed in less than 1h at pH 3 in H_2O_2/Fe^{2+} system. • The optimal conditions obtained were 90 mg/L H_2O_2, 5 mg/L Fe^{2+} and 20 mg/L DEHP in the solution at pH 3. • The maximum removal efficiency for real waste water was 70.4 % as compared to synthetic water (90.5%) in optimal conditions.	Esmaeli et al. **[43]**

23	Pulse radiolysis and electron beam radiolysis	dimethyl phthalate	• The bimolecular rate constants for the reaction of hydroxyl radical and hydrated electron with dimethyl phthalate were found to be 3.4 x 10^{-9} $M^{-1}s^{-1}$ and 1.6 x 10^{-10} $M^{-1}s^{-1}$, respectively, using pulse radiolysis. • Hydroxyl radicals reacted with the aromatic ring while hydrated electron reacted with the ester group.	Wu et al. **[44]**
24	Photocatalysis (TiO_2/UV process)	diethyl phthalate	• The optimal TiO_2 (Degussa P25) dosage and pH for the degradation was 1.0 g/L and 7.0, respectively. • The degradation reaction followed first order kinetics. • The maximum degradation was 78.6 % in 3h in optimum conditions.	Monsouri et al. **[45]**
25	Sonophotolytic degradation	diethyl phthalate	• Sonophotolytic degradation was more efficient than single sonolysis and photolysis process due to generation of H_2O_2.	Na et al. [46].
26	Photocatalytic degradation using organic layered double hydroxide (LDHs)/TiO_2 composites	dimethyl phthalate	• The enhanced rate of degradation of dimethyl phthalate was related to the synergistic effect between the enrichment of dimethyl phthalate on the composites and the external hydroxyl groups of composites.	Huang et al. **[47]**
27	Photocatalytic degradation using hollow glass microspheres coated with TiO_2 (HGM-TiO_2)	dimethyl phthalate	• The degradation of dimethyl phthalate followed first order kinetics. • The dimethyl degradation increased linearly with increasing dosage of HGM-TiO_2 up to 8.0 g/L.	Jiang et al. **[48]**

28	Electrochemical degradation using a one compartment filter press flow cell and a commercial dimensionally stable anode (DSA) electrode	dimethyl phthalate	• It was observed that in presence of low NaCl concentration, the electrolysis exhibited high degradation of dimethyl phthalate due to development of low recalcitrant organochlorine compounds. • Acidic conditions at elevated temperatures favored high degradation of dimethyl phthalate due to increase in oxidation power of Cl_2 and HOCl.	Souza et al. **[49]**
29	Degradation using UV irradiation, ozonation and UV/O_3 processes, separately	di-2-ethylhexyl phthalate (DEHP)	• UV irradiation combined with ozonation showed better degradation of DEHP than UV irradiation and ozonation alone due to synergistic effects. • The maximum DEHP degradation was 74 % with 200g/h ozone dosage in ozonation process alone but degradation was 93 % in UV/O_3 process in similar conditions.	Zarean et al. (2015) **[50]**
30	Sonophotolytic and sonolytic degradation	dimethyl phthalate (DMP), diethyl phthalate (DEP), di-n-butyl phthalate (DBP) and monomethyl phthalate (MMP))	• An ultrasonic system (400 kHz) and a photolytic system at 253.7 nm were employed separately and together for both pure water and secondary effluent. • Phthalate esters having greater hydrophobicity showed fast sonolysis and greater competitiveness in sonochemical reactions in the presence of other compounds. • But the synergistic benefits of combining UV with ultrasound were found to be less for more hydrophobic phthalate esters due to the lower accumulation of H_2O_2 which resulted in lower UV/H_2O_2 generation of •OH	Xu et al. **[51]**

			radicals.	
31	Electrokinetic process combined with a novel Fenton-like process catalyzed by nanoscale schwertmannite (Nano-SHM).	phthalate esters and acetaminophen	• The structure decomposition occurred when sediment was subjected to the novel Fenton-like oxidation. • Elecrtrokinetics process gave a solution for the problem by increasing transport of oxidation chemicals, acid/base fronts, and various ions in the remediation system. • The remediation time of 14 to 28 days was found to be beneficial for the removal of target compounds.	Yang et al. **[52]**
32	UV-254 nm/H_2O_2 process	dibutyl phthalate (DBP)	• The percentage removal of dibutyl phthalate was 77.1 % at initial concentration of 1µM, H_2O_2 dosage of 1.0 mM, UV fluence of 160 mJ/cm^2 and pH of 7.6. • The DBP degradation followed pseudo first order kinetics. • The presence of inorganic anions of Cl^-, NO_3^- and SO_4^{2-} and cations Fe^{3+} and Cu^{2+} had little impact on DBP degradation. Cu^{2+} improved degradation efficiency slightly even at low concentration of 0.01 mg/L.	Wang et al. **[53]**.

2.4 Gaps in study

Physical/Chemical treatments and biological treatments for the degradation of phthalate esters have their own limitations. These methods are compound specific, time consuming, tedious and expensive. Advance oxidation processes are fast processes and have many advantages. There are many reports available for the degradation of phthalate esters using advanced oxidation processes. Among advanced oxidation processes, heterogeneous photocatalytic degradation using semiconductor is a promising technology to degrade organic pollutants in wastewater. This process has many benefits like complete mineralization of most organic pollutants, mild temperature and pressure conditions required, environmental friendly, low cost, no secondary pollution problems and potential to treat pollutants present in trace amounts in wastewater **[54]**. Although, phthalate esters have been degraded using heterogeneous photocatalytic degradation technique using TiO_2 based photocatalyts, but transition metals (e.g. Fe, Zn, Cu, Ni) doped TiO_2 as photocatalysts for degradation of phthalate esters need to be explored. Doping TiO_2 with transition metals is a promising technique to increase the range of absorption of TiO_2 into the visible region and increasing its photocatalytic activity. Researchers have doped many transition metals like Fe, Cr, Mn, Co, Mo, Ni, Cu and Zn into TiO_2 to modify its band gap and photocatalytic activity **[55-56]**. Moreover, the codoping of transition metals in TiO_2 for the enhanced degradation of phthalate esters also needs to be explored. Considering these gaps in study, following are the objectives of the present work.

- To synthesize undoped and doped TiO_2 nanoparticles with transition metals such as Cu, Zn, Fe, Ni.
- To characterize the synthesized samples using X-Rays diffraction technique (XRD), Transmission Electron Microscope (TEM), Fourier Transform Infrared Spectroscopy

(FTIR), Photo Luminescence (PL), Diffuse Reflectance Spectra (DRS), Thermogravimetric Analysis (TGA).

- To study the effect of TiO_2 nanoparticles size distribution on degradation of phthalate esters.

References

1. D.W. Gao, Z.D. Wen, Sci Total Environ 541 (2016) 986.
2. M.M. Abdel daiem, J. Rivera-Utrilla, R. Ocampo-Perez, J.D. Mendez-Díaz, M. Sanchez-Polo, J Environ Manage 109 (2012) 164.
3. E. Ayranci, E. Bayram, J Hazard Mater B122 (2005) 147.
4. S.V. Mohan, S. Shailaja, M.M. Krishna, P.N. Sharma, J Hazard Mater 146 (2007) 278.
5. C. Zhang, Y. Wang, Waste Manage 29 (2009) 110.
6. Z. Zheng, H. Zhang, P.J. He, L.M. Shao, Y. Chen, L. Pang, Chemosphere 75 (2009) 180.
7. C.J. Salim, H. Liu, J.F. Kennedy, Carbohydr Polym 81 (2010) 640.
8. H. Zheng, J. Ma, C. Zhu, Z. Zhang, L. Liu, Y. Sun, X. Tang, Sep Purif Technol 123 (2014) 35.
9. J. Boonorat, C. Chiemchaisri, W. Chiemchaisri, K. Yamamoto, Chemosphere 150 (2016) 639.
10. X. Wei, W. Shi, Y. Fei, J. Chen, B. Lv, Y. Chen, Chem Eng J 292 (2016) 382.
11. D.R. Shelton, S.A. Boyd, J.M. Tledje, Environ Sci Technol 18 (1984) 93.
12. J. Wang, P. Liu, Y. Qian, Environ Int 22 (1996) 737.
13. W. Jianlong, C. Lujun, S. Hanchang, Q. Yi, Chemosphere 41 (2000) 1245.
14. B.V. Chang, C.M. Yang, C.H. Cheng, S.Y. Yuan, Chemosphere 55 (2004) 533.
15. C. Pakau, M. Kornaros, K. Stamatelatou, G. Lyberatos, Bioresour Technol 100 (2009) 1634.
16. B. Prasad, S. Suresh, APCBEE Procedia 1 (2012) 16.
17. J. Gao, J. Chi, Marine Poll Bull 99 (2015) 70.

18. J.W. Wang, Z.H. Luo, W. Xu, J.F. Ding, T.L. Zheng, Int Biodeterior Biodegradation 109 (2016) 223.
19. M.A. Perez, S.T. Beristain, J.G. Davila, M.G. Perez, M.C.G. Ruiz, C. Sanchez, Sci Total Environ 566 (2016) 1186.
20. B. Bethi, S.H. Sonawane, B.A. Bhanvase, S. Gumfekar, (2016) Chem Eng Process 109 (2016) 178.
21. M. Antonopoulou, E. Evgenidou, D. Lambropoulou, I. Konstantinou, Water Res 53 (2014) 215.
22. M. Muneer, J. Theurich, D. Bahnemann, J Photochem Photobiol A Chem 143 (2001) 213.
23. G. Mailhot, M. Sarakha, B. Lavedrine, S. Malato, Chemosphere 49 (2002) 525.
24. E. Psillakis, D. Mantzavinos, N. Kalogerakis, Chemosphere 54 (2004) 849.
25. C. Ooka, H. Yoshida, K. Suzuki, T. Hattori, Microporous Mesoporous Mater 67 (2004) 143.
26. G. Yang, X.K. Zhao, X.J. Sun, X.L. Lu, J Hazard Mater B126 (2005) 112.
27. C.S. Chiou, J.L. Shie, C.Y. Chang, C.C. Liu, C.T. Chang, J Hazard Mater B137 (2006) 1123.
28. S. Kaneco, H. Katsumata, T. Suzuki, K. Ohta, Chem Eng J 125 (2006) 59.
29. B. Xu, N.Y. Gao, X.F. Sun, S.J. Xia, M. Rui, M.O. Simonnot, C. Causerrand, J.F. Zhao, J Hazard Mater B139 (2007) 132.
30. Z. Yunrui, Z. Wanpeng, L. Fudong, W. Jianbing, Y. Shaoxia, Chemosphere 66 (2007) 145.
31. B.L. Yuan, X.Z. Li, N. Graham, Chemosphere 72 (2008) 97.

32. B.L. Yuan, X.Z. Li, N. Graham, Water Res 42 (2008) 1413.

33. X. Ding, T. An, G. Li, J. Chen, G. Sheng, J. Zhao, Res Chem Intermed 34 (2008) 67.

34. C.Y. Chen, P.S. Wu, Y.C. Chung, Bioresour Technol 100 (2009) 4531.

35. Y.H. Chen, L.L. Chen, N.C. Shang, J Hazard Mater 172 (2009) 20.

36. X. Shen, L. Zhu, C. Huang, H. Tang, Z. Yub, F. Deng, J Mater Chem 19 (2009) 4843.

37. H. Li, X. Zhu, Y. Jiang, J. Ni, Chemosphere 80 (2010) 845.

38. W.B. Huang, C.Y. Chen, Water Air Soil Pollut 207 (2010) 349.

39. H. Wang, D.J. Sun, Z.Y. Bian, J Hazard Mater 180 (2010) 710.

40. L. Xu, X. Yang, Y. Guo, F. Ma, Y. Guo, X. Yuan, M. Huo, J Hazard Mater 178 (2010) 1070.

41. R. Huang, H. Yan, L. Li, D. Deng, Y. Shu, Q. Zhang, Appl Catal B 106 (2011) 264.

42. Y. Jing, L. Li, Q. Zhang, P. Lu, P. Liu, X. Lu, J Hazard Mater 189 (2011) 40.

43. R. Esmaeli, A.H. Hassani, A. Eslami, M.A. Moghadam, A.A. Safari, Iran J Environ Health Sci Eng 8 (2011) 201.

44. M.H. Wu, N. Liu, G. Xu, J. Ma, L. Tang, L. Wang, Radiat Phys Chem 80 (2011) 420.

45. L. Monsouri, L. Bousselmi, Desalination Water Treat 40 (2012) 63.

46. S. Na, Y.G. Ahn, M. Cui, J. Khim, J Environ Manange 101 (2012) 104.

47. Z. Huang, P. Wu, Y. Lu, X. Wang, N. Zhu, Z. Dang, J Hazard Mater 246 (2013) 70.

48. W. Jiang, J.A. Joens, D.D. Dionysiou, K.E. O'Shea, J Photochem Photobiol A Chem 262 (2013) 7.

49. F.L. Souza, J.M. Aquino, D.W. Miwa, M.A. Rodrigo, A.J. Motheo, J Braz Chem Soc 25 (2014) 492.

50. M. Zarean, B. Bina, A. Ebrahimi, H. Pourzamini, F. Esteki, Int J Environ Health Eng 4 (2015) 1.

51. L.J. Xu, W. Chu, N. Graham, J Hazard Mater 288 (2015) 43.

52. G.C.C. Yang, S.C. Huang b, C.L. Wang, Y.S. Jen, Chemosphere 159 (2016) 282.

53. D. Wang, X. Duan, X. He, D.D. Dionysiou, Environ Sci Pollut Sci Res 23 (2016) 23772.

54. A. O. Ibhadon, P. Fitzpatrick, Catalysts 3 (2013) 189.

55. A. Zaleska, Recent Pat Eng 2 (2008) 157.

56. B. Liu, H.M. Chen, C. Liu, S. C. Andrews, C. Hahn, P. Yang, J Am Chem Soc 135 (2013) 9995.

Chapter 3
Experimental Techniques

Overview

This chapter encompasses the details of the raw materials and the synthesis procedure used to prepare undoped and transition metal doped TiO_2 nanoparticles. Various characterization techniques like X-ray diffraction (XRD), UV-vis diffuse reflectance spectra (DRS), Fourier transform infrared spectroscopy (FTIR), Thermogravimetric analysis (TGA), Raman spectroscopy, Photoluminescence (PL) and High resolution transmission spectroscopy (HRTEM) used for the characterization of the samples have been discussed. The details of the experimental conditions for synthesizing the samples and procedure for the photocatalytic degradation of phthalate esters are discussed in detail.

3.1 Chemical reagents

Table 1 presents the list of chemicals used in the present study. All the chemicals were used in pristine form without any further purification. Doubly distilled water was used during experimentation.

Table 3.1: List of chemicals used in present investigations.

Chemical reagent	**Chemical formula**	**Purity**	**Supplier**
Titanium (IV) isopropoxide	$C_{12}H_{26}O_4Ti$	97 %	Sigma Aldrich
Anhydrous ethanol	C_2H_5OH	99.9 %	Merck
Nitric acid	HNO_3	69-72 %	Loba chemie
Diethyl phthalate	$C_{12}H_{14}O_4$	99 %	Sd fine chem
Bis (2-ethylhexyl) phthalate,	$C_{24}H_{38}O_4$	99 %	Sd fine chem
Dimethyl phthalate	$C_{10}H_{10}O_4$	99 %	Sd fine chem
Nickel (III) nitrate hexahydrate	$Ni(NO_3).6H_20$	97 %	Himedia
Ferric nitrate nanohydrate,	$Fe(NO_3).9H_2O$	98 %	Loba chemie
Copper (II) acetate monohydrate	$C_4H_6CuO4.H_20$	98 %	Loba Chemie

3.2 Synthesis of samples

Transition metal doped TiO_2 nanoparticles were prepared by the sol-gel technique employing titanium (IV) isopropoxide as a Ti precursor. A mixture of titanium (IV) isopropoxide and anhydrous ethanol was initially prepared. These were mixed in a molar ratio of 1:25. This solution was magnetically stirred for 30 min. The above prepared mixture was added dropwise to a solution containing nitric acid, anhydrous ethanol, distilled water and transition metal salt

under magnetic stirring. The solution of nitric acid, anhydrous ethanol and distilled water was in molar ratio of 1: 3.6: 4.2. A transparent color sol was obtained, after complete addition of the ingredients. Furthermore, the sol was stirred continuously over a period of 6 h at room temperature to obtain the gel. The gel was kept for aging for one day and then aged gel was dried at 90 ^{o}C. To get a fine as well as homogeneous powder, the dried solid was ground in an agate mortar. The sample was washed with distilled water thrice to remove the impurities. Then the sample was dried and ground in agate mortar. Finally, the obtained powder was calcined at 450 ^{o}C for two hours. In present study, doping of Fe, Cu and Ni metal into TiO_2 was done. The transition metal salts used for the doping of Fe, Cu and Ni were Ferric nitrate nanohydrate ($Fe(NO_3).9H_2O$), Copper (II) acetate monohydrate ($C_4H_6CuO4.H_2O$) and Nickel (III) nitrate hexahydrate ($Ni(NO_3).6H_20$), respectively. The codoping of Fe and Cu into TiO_2 was also done. The undoped TiO_2 nanoparticles were prepared using the similar method as given as above except in the absence of metal salts. The synthesis of samples by above described method followed the work of Chen et al. [1].

3.3 Characterization methods

3.3.1 X-ray diffraction (XRD)

X-ray powder diffraction is a non-destructive, analytical technique mainly used for the detection of crystalline phases present in a material. It is also used to calculate the average crystallite size, lattice parameters, crystallinity, lattice strain etc. [2]. XRD involves the diffraction of monochromatic X-ray by a powder sample. X-ray diffractometer has three basic components i.e. (i) an X-ray tube (ii) a sample holder and (iii) an X-ray detector. X-rays are produced by a cathode ray tube which are filtered to produce monochromatic radiation and finally directed

towards the sample in the form of a collimated beam. When X-ray interacts with the sample, it produces constructive interference (and a diffracted ray) when the condition satisfy Braggs law, $n\lambda = 2\ d \sin\theta$ where, λ is the wavelength of the X-ray, θ is the scattering angle, and n is an integer representing the order of the diffraction peak [2]. When the sample is scanned over a range of 2θ angles, it gives the diffraction from all the possible directions of the lattice due to the random orientation of the powder materials. Diffraction angles are used to calculate the d-spacings of the unit cells which are further used for the identification of the crystalline phases. The observed patterns are indexed with the standard reference patterns. In the present study, X-ray powder diffraction analysis was carried out using PANalytical's X'Pert Pro X-ray diffractrometer with Cu Kα radiations (λ=1. 54 Å) and Ni filter with working voltage and current of 45 kV and 40 mA, respectively. The patterns were recorded over the angular range of 20^o-80^o. During experimentation the step size was 0.0130^o.

3.3.2 Fourier transform infrared spectroscopy (FTIR)

In infrared (IR) spectroscopy, the IR radiation incident on the sample gets absorbed and some part of it gets transmitted. IR spectroscopy is based the absorption of specific frequencies by the molecules which are characteristic of their structure. Thus, no two compounds produce the same infrared spectrum. The covalent bonds are like stiff springs which are capable of being stretched and bent. The inter-atomic distance between two atoms changes continuously in a stretching vibration. The angle between two bonds changes in bending vibrations. The bending vibrations are of four types i.e. scissoring (bending), rocking, wagging and twisting. Modern IR instruments are based on Michelson interferometer which employs a powerful and fast computer. The absorption spectrum is obtained by Fourier transform of an interferogram. Hence the instruments are known as Fourier transform infrared spectrometers. The absorption bands in a recorded IR

spectrum have three important parameters i.e. frequency, shape and intensity. Any deviation in band frequency, shape or intensity between the two spectra indicates the difference between the samples. All single absorption bands by nature are symmetric in shape and have shape that resembles a normal bell curve. Deviation in band shape is related to similar function group exist in different molecular environment [3]. The infrared spectra of the samples were recorded on FTIR spectrometer Model RZX (Perkin Elmer) using KBr pellets. The resolution of the FTIR instrument was 1 cm^{-1} and scan range of 4000 cm^{-1} to 250 cm^{-1}. Two milligrams of each sample was ground with 100 mg of KBr into a fine powder and pressed after applying 14 $kNcm^{-2}$ pressures for 5 min to get pellets for IR study.

3.3.3 Raman spectroscopy

Raman spectroscopy involves the scattering of a monochromatic radiation (from a laser source) by the sample. Raman spectrum results from the inelastic collisions of photons with molecules. In an inelastic collision, energy is exchanged between the photons and the molecules. The energy of resulting inelastically scattered photons get shifted up or down in comparison to the original monochromatic radiation [4]. This shift in energy gives the information about the vibrational modes in the system. A change in polarizability during molecular vibration is a crucial need to get Raman spectrum. A Raman spectrum is presented as intensity versus wavelength shift. In present study, Raman spectroscopic studies of the samples are carried out using Reinshaw in Via Raman spectrometer. For data collection 514.5 nm line of Ar^{+} laser along with 20 mW power was used. The calibration was done with the help of silicon as a reference at 520 cm^{-1} within ±1 cm^{-1}. For Raman spectra, the powder sample was loaded in a plastic sample holder and surface was made smooth by compressing the powder.

3.3.4 Diffuse reflectance spectroscopy

Diffuse reflectance spectroscopy (DRS) has been used to study the optical properties of the samples. Using DRS, it is possible to study the optical properties of the powder samples. DRS overcomes the effects of light scattering in the absorption spectra of the samples dispersed in liquid. In DRS, light with variable wavelength is incident on the sample, where it gets reflected, scattered and transmitted. The diffusely scattered light is then directed to detector optics by the collection accessory. The part of beam scattered within the sample and returned to the surface is considered to be diffuse reflection [5]. Diffuse reflectance spectra (DRS) of powdered samples were obtained from UV-Vis Spectrophotometer (Hitachi U-3900H) in spectral range of 250-800 nm. The sampling interval and scan speed during scan was 0.50 nm and 300 nm /min, respectively.

3.3.5 Ultraviolet-visible spectroscopy (UV-vis spectroscopy)

UV-vis spectroscopy deals with the absorption of light in ultraviolet and visible spectral region. It involves the transition between electronic energy levels of the molecule. The absorption of ultraviolet or visible light by a molecule promotes the electrons from ground state to excited states. In most of the cases, the favored transition is between highest occupied molecular orbital (HOMO) to lowest unoccupied molecular orbital (LUMO). UV-vis spectroscopy follows Beer Lambert law which states that: when a beam of monochromatic light is passed through a solution of an absorbing substance, the rate of decrease of intensity of radiation with the thickness of the absorbing solution is proportional to the incident radiation as well as the concentration of solution [6]. The extent of photocatalytic degradation of phthalate esters is determined using absorption spectra of phthalate esters (samples taken during degradation at regular intervals) using UV-vis Spectrometer (Hitachi U-3900H). The spectra of the samples were obtained in

spectral range of 250-800 nm. The sampling interval and scan speed during scan was 0.50 nm and 300 nm /min, respectively. The calculations were done on basis of Beer Lambert law.

3.3.6 Photoluminescence spectroscopy

Photoluminescence spectroscopy is a non-destructive technique to examine the electronic structure of the materials. In PL spectroscopy, light is incident on the specimen, where it gets absorbed. The excess energy is transferred to the material by a process called photoexcitation. The excess energy can be dissipated by the sample by the emission of light called luminescence. Photoexcitation causes electrons of the material to transit into allowed excited energy levels. The excess energy may be released either by radiative process (in the form of light) or by non-radiative process. The molecules may drop down into any of several vibrational levels in the ground state emitting the photons with different energies. The structure of various vibrational levels can be determined by analyzing the intensity and wavelength of light emitted in fluorescent spectroscopy [7]. In present study, Photoluminescence (PL) emission spectra at room temperature were measured by using a spectrofluorimeter (Perkin Elmer, Model- LS55).

3.3.7 Thermal analysis (TGA)

Thermo gravimetric analysis (TGA) is a technique in which the mass of a substance is measured as a function of temperature or time when the substance is subjected to a controlled temperature program. Mass vs temperature graph obtained in this analysis is called thermogram (TG). The mass variation is attributed to: (i) mass reduction due to desorption, decomposition or drying and (ii) the gain of mass due to oxidation process. The weight of sample is plotted against temperature and time [8]. Thermal analysis is carried out with the help of NETZCH Zupiter STA

449 F3 simultaneous thermal analyzer in argon atmosphere with heating rate of 10 ^{o}C/min from 25 to 800 ^{o}C. The reference used was Al_2O_3.

3.3.8 High resolution transmission electron microscopy (HRTEM)

Transmission electron microscopy (TEM) provides morphological, compositional and crystallographic information based on the interaction of energetic electrons with the sample. The emitted electrons from the filament pass through a series of electromagnetic lenses and strike on the screen to form the image. The wavelength of the electrons determines the image resolution.

The high-resolution transmission electron microscopy (HRTEM) uses both the transmitted and the scattered beams to generate an interference image. The electrons coming out of the sample combine at a point in the image plane. HRTEM is extensively used to investigate the crystal structures and lattice imperfections in various types of materials with higher resolution on an atomic scale [7]. The point defects, stacking faults, dislocations, precipitates grain boundaries and surface structures can be characterized by this technique [7].

In present study, the morphology and size of nanoparticles are characterized using high resolution transmission electron microscopy (HRTEM) on instrument Tecnai G2 20, 200 keV, FEI.

3.4 Photocatalytic degradation experiment

The photocatalytic degradation of diethyl phthalate is carried out in a three-jacketed column photoreactor (shown in Fig. 3.1) made up of borosilicate glass with an effective volume of 100 ml. The three jackets of photoreactor are used individually for circulating water to maintain the temperature, for the lamp and for the reaction mixture. A mercury lamp of 125 W (λ=365 nm)

having intensity 40,000 lux is placed axially inside the photoreactor. The experimental conditions are fixed at 30ppm diethyl phthalate solution and catalyst loading of 1g/L. Prior to photoreaction, the suspension is magnetically stirred in dark condition for 30 min to establish

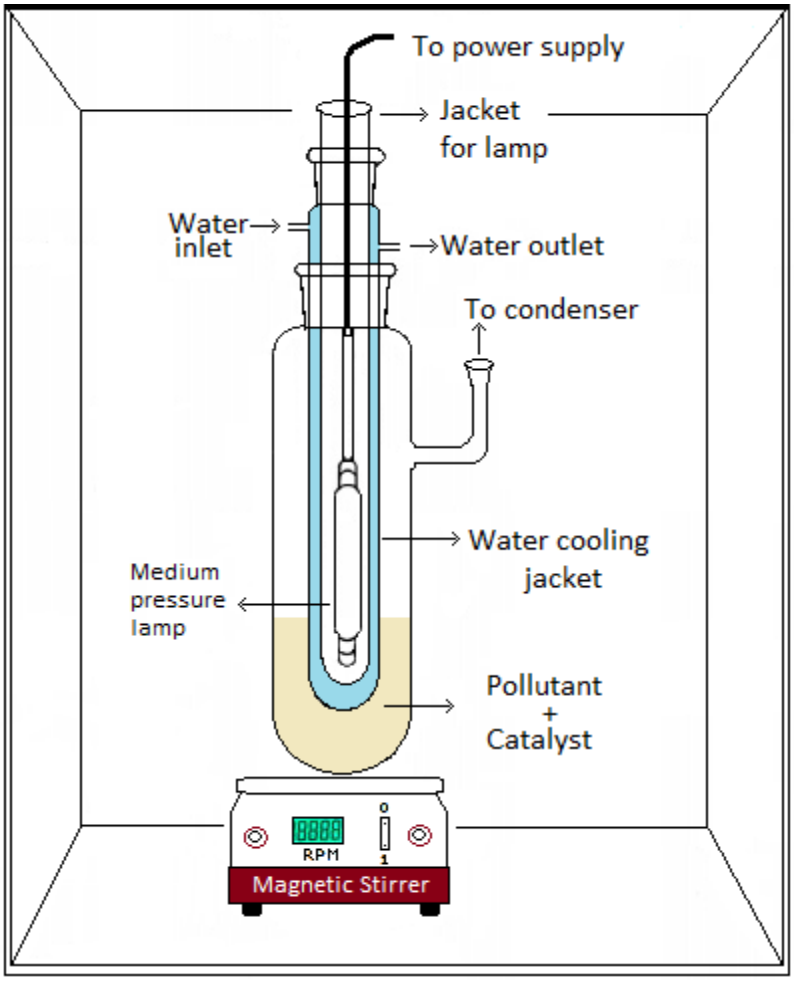

Figure 3.1: Experimental setup for photocatalytic reactions.

absorption/desorption equilibrium condition. Likewise during the photocatalytic reaction, the aqueous suspension is magnetically stirred. Aliquots of mixture are taken out at periodic intervals during the irradiation and then filtered through Millipore syringe filters (PTFE, 0.45µm). The filtrates were analyzed for the maximum absorbance at different time intervals using a UV-Vis spectrometer. The photocatalytic degradation of diethyl phthalate is determined

by a UV-Vis spectrometer on the basis of Beer- Lambert's Law. The UV spectrum of diethyl phthalate comprises two maxima, a peak at 279 nm and a strong peak at 229 nm. Since the absorbance is maximum around 229 nm, the absorbance of filtrates at different time intervals is compared at λ_{max}=229 nm wavelength. Our results are well supported by the work of Xu et al. [9]. The photocatalytic activity of the samples is measured in terms of the degradation of diethyl phthalate. The extent of diethyl phthalate degradation is monitored using UV-vis spectrophotometer (Hitachi U-3900H).

References

1. C. Chen, Z. Wang, S. Ruan, M. Zhao, B. Zou, F. Wu (2008) Dyes Pigm 77 (2008) 204.
2. B.D. Cullity and S.R. Stock, Elements of X-ray Diffractions (2001) Prentice Hall New Jersey.
3. M.R. Derrick, D. Stulik, J.M. Landry, Infrared Spectroscopy in Conservation Science (1999) The Getty Conservation Institute Los Angles.
4. J.R. Ferraro, Introductory Raman Spectroscopy (2003) Academic Press New Jersey.
5. Ebraheem S, El-Saied Antar, Mater Sci Appl 4 (2013) 324.
6. H.H. Helmut, UV-Vis spectroscopy and Its applications, Springer Lab Manuals (1st Edition).
7. C.P. Poole, F.J. Owens, Introduction to Nanotechnology (2003) Wiley India.
8. P. Gabbott, Principles and Applications of thermal analysis (2008) John Wiley & Sons.
9. B. Xu, N.Y. Gao, X.F. Sun, S.J. Xia, M. Rui, M.O. Simonnot, C. Causerrand, J.F. Zhao, J Hazard Mater B 139 (2007) 132.

Chapter 4
Results and discussion
Synthesis, characterization and photocatalytic activity of anatase- brookite heterojunctions

Overview

The present chapter describes the studies of TiO_2 nanoparticles prepared via sol-gel method followed by calcination at different temperatures (200 ^oC to 400 ^oC) and their photocatalytic study. The structural, optical and thermal properties of the samples are investigated using by X-ray diffraction (XRD), UV-Vis diffuse reflectance spectroscopy (DRS), Fourier transform infrared spectroscopy (FTIR), Raman spectroscopy, Thermogravimetric analyser (TGA), High resolution transmission electron microscopy (HRTEM) and photoluminescence (PL) techniques. The photocatalytic activity of samples is discussed in light of the degradation of diethyl phthalate.

4.1 Introduction

TiO_2 mainly exists in three crystalline forms namely anatase, rutile and brookite. Anatase phase has been reported to be more photo catalytically active than rutile or brookite phases. However, when anatase phase coexists with small fraction of rutile and brookite, it shows enhanced photocatalytic activity [1]. Anatase-brookite heterojunctions are rarely studied in comparison to the anatase-rutile heterojunctions. The present chapter aims to study effect of calcination temperature on different properties of TiO_2 anatase-brookite heterojunctions for the photocatalytic degradation of diethyl phthalate. The calcination temperature range is kept between 200-400 ^oC because above this temperature (say 450 ^oC), anatase-brookite heterojunctions are converted to anatase-rutile. The as synthesized sample, sample calcined at 200 ^oC, 300 ^oC and 400 ^oC are labeled as T1, T2, T3 and T4, respectively. The results are presented in the following sections.

4.1.1 XRD analysis

X-ray diffraction patterns of TiO_2 calcined at various temperatures are shown in Fig. 4.1. XRD patterns show the presence of anatase phase (ICDD No. 00-071-1169) and minor brookite phase (ICDD No. 15-0875). A small peak corresponding to the brookite phase at 30.8^o is observed in the present samples. The type of polymorphs formed in the final oxide is strongly dependent not only on calcination but also by the synthesis factors (type of precursor and solvent, acid catalyst, synthesis environment etc.) [2]. Volume fractions of anatase and brookite phase calculated by direct comparison method [3] and are given in Table 4.1. The samples show variation in volume fractions of the phases. Volume fraction of brookite phase is minimum in T2 sample.

Table 4.1: Volume fraction of anatase and brookite phase calculated from XRD data.

Sample Code	Volume fraction of anatase phase (%)	Volume fraction of brookite phase (%)
T1	97	3
T2	99	1
T3	98	2
T4	98	2

The crystallite size of samples is calculated using Scherrer equation [3].

$$D = \frac{K\lambda}{\beta \cos\theta} \tag{4.1}$$

where D is the crystallite size, K is the shape factor, λ is the wavelength of X-ray (Cu Kα= 1.5406 Å), β is the full width at half maximum (FWHM), θ is the diffraction angle. The crystallite size of T1, T2, T3 and T4 is found to be 5.48 nm, 5.79 nm, 6.57 nm, 8.43 nm, respectively. The crystallite size is calculated coressponding to the most intense (101) peak of anatase phase. An incresase in crystallite size with increasing calcination temperature indicates enhanced crystallite growth of TiO_2 nanoparticles.

The decrease in full width at half maximum (FWHM) with increasing calcination temperature (Table 4.2) indicates the increasing crystallinity in the samples. Fig. 4.1 shows that (101) peak of anatase is shifiting towards higher angles with increasing calcination temperature, which reveals the relaxation of tensile stress. The increase in 2θ values indicates the decrease in distance between crystal planes, which is in close agreement with the lattice parameters. Lattice parameters of samples are calculated using following formula [4]:

$$\frac{1}{d^2} = \frac{h^2+k^2}{a^2} + \frac{l^2}{c^2} \tag{4.2}$$

where *d* is the interplanar separation corresponding to the miller indices *h*, *k*, *l* and *a*, *c* are the lattice constants. The lattice parameters of samples given in Table 4.2 are calculated using XRD peaks at 2θ = 25.3 (101) and 47.84 peaks of anatase phase.

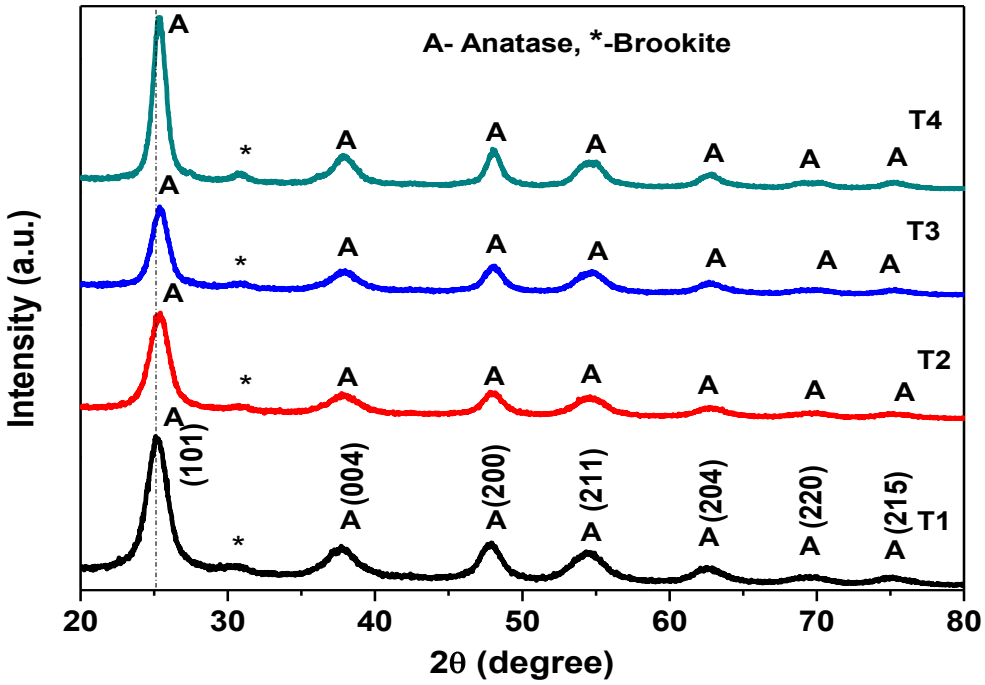

Figure 4.1: XRD patterns of TiO_2 nanoparticles calcined at various temperatures.

The X-ray density (given in Table 4.2) has also been calculated for all the samples using following formula [4]:

$$\rho = \frac{nM}{NV} \tag{4.3}$$

where ρ is the theoretical density, *M* is the molecular weight, *N* is the Avogadro number, *n* is the number of atoms per unit cell and *V* is the volume of the unit cell. For anatase phase the value of *n* is 4. Furthermore, the specific area of samples (given in Table 4.2) is calculated by the following equation [4]:

$$S = \frac{6}{D*\rho} \tag{4.4}$$

where *S* is the specific surface are, *D* is the crystallite size and ρ is the theoretical density.

Table 4.2: The structural parameters calculated from the XRD data corresponding to the characteristic peak (101) of anatase phase.

Sample Code	2θ (degree)	FWHM (degree)	d-spacing (Å)	Crystallite size (nm)	Lattice parameters (Å)	Unit cell volume (Å^3)	Density (g/cm^3)	Specific surface area (cm^2/g)
T1	25.20	1.485	3.531	5.48	a= b=3.79 c=9.56	137.90	3.849	2.844 x 10^6
T2	25.35	1.405	3.510	5.79	a= b=3.78 c=9.33	133.87	3.965	2.613 x 10^6
T3	25.40	1.238	3.503	6.57	a=b=3.78 c=9.29	132.88	3.995	2.285 x 10^6
T4	25.35	0.9647	3.5100	8.43	a=b=3.78 c=9.41	134.59	3.944	1.804 x 10^6

4.1.2 DRS analysis

Fig. 4.2 (a) shows the diffuse reflectance spectra of TiO_2 nanoparticles calcined at various temperatures. The intense absorption edge observed below 410 nm is related to the band−band transition of the TiO_2 nanoparticles according to its intrinsic bandgap [5]. The band gap of the samples is calculated using Kubelka-Munk Function [6] which is $f(R) = (1-R)^2/2R$, where R is the diffuse reflectance. In the present case, $(f(R).hv)^{1/2}$ is plotted against photon energy hv (Fig. 4.2 (b)) and the linear portion of the curves is extrapolated to have an intercept on the x-axis. The value at x-axis where intercept cuts i.e. $(f(R).hv)^{1/2}= 0$ is taken as the value of the band gap. For the linear region of the plots, the following relationship must be satisfied:

$$[f(R).hv]^n = K(hv - E_g) \quad (4.5)$$

where E_g is band gap energy and K is a characteristic constant for every semiconductor material. The band gap energy value of T1, T2, T3 and T4 sample is 3.12, 3.18, 3.16 and 3.15 eV, respectively. In comparison to this, the band gap energy values of TiO_2 nanoparticles synthesized by Xue et al. [5] were found to in range from 3.213 to 3.268 eV.

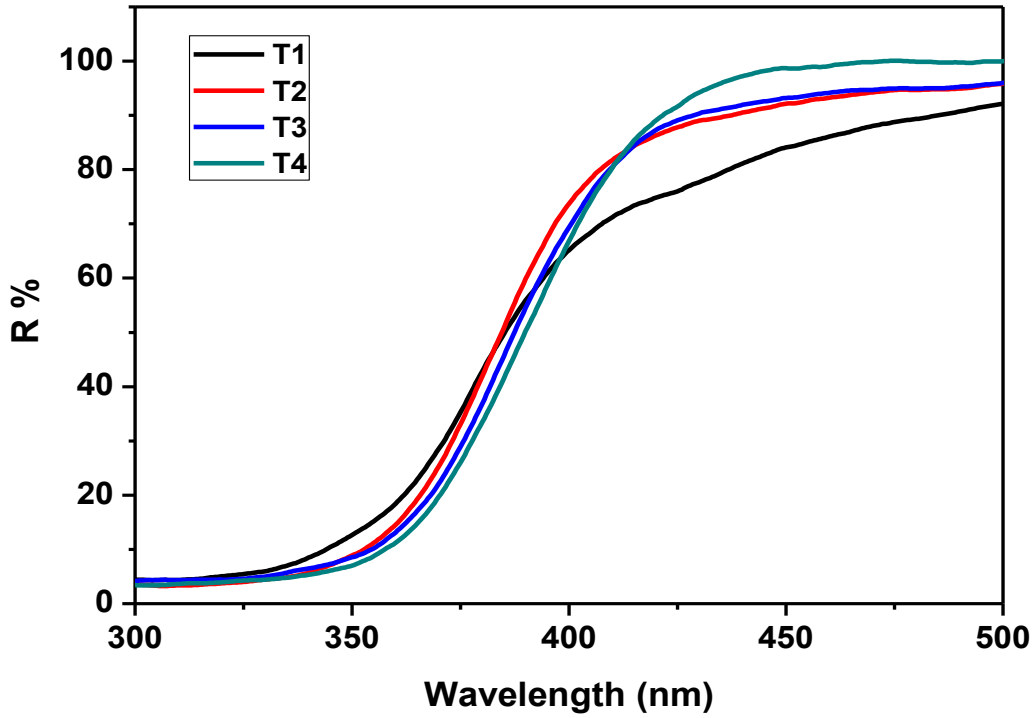

Figure 4.2 (a): Diffuse reflectance spectra of TiO_2 nanoparticles calcined at various temperatures.

Urbach energy gives a measure of structural randomness in a material and is given by the tail region where absorption α (ν) depends exponentially on the photon energy hν as follows [7]:

$$\alpha = \alpha_0 exp\left\{\frac{(h\nu)}{E_u}\right\} \quad (4.6)$$

where E_u is the Urbach energy. Absorption coefficient is proportional to *f(R)*, hence E_u is calculated by plotting *ln{f(R)}* versus *hν*. The reciprocal of the slope of linear portion of *ln f(R)*

vs *hv* gives the Urbach energy. The Urbach energy of T1, T2, T3 and T4 is found to be 0.113, 0.082, 0.080, and 0.073 eV, respectively.

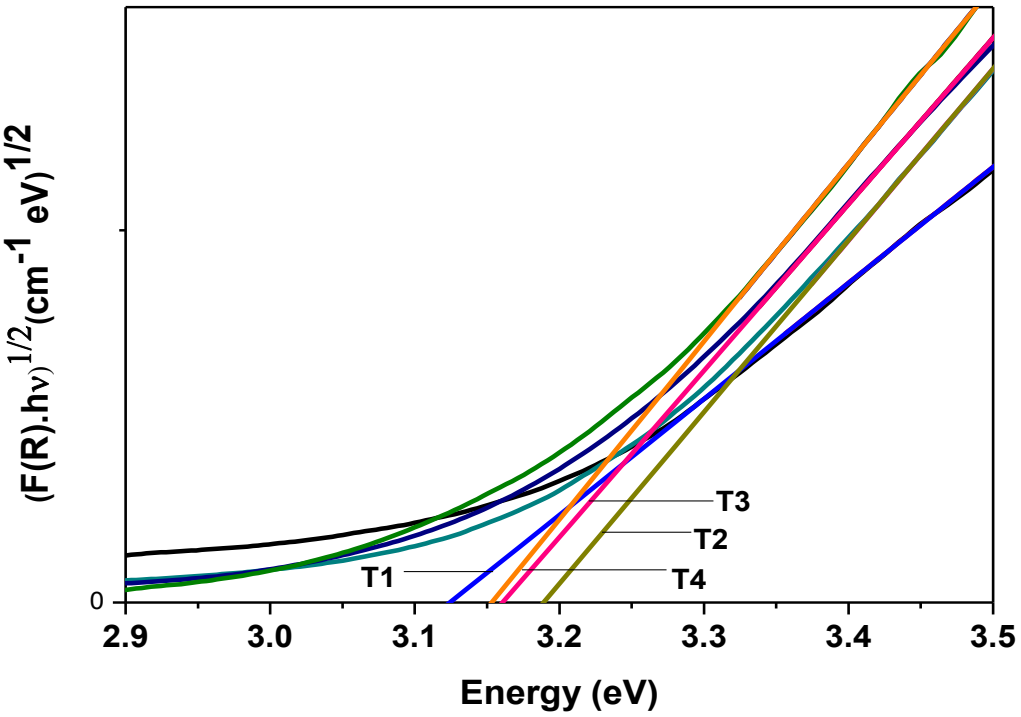

Figure 4.2 (b): Determination of band gap energy of samples using Kubelka-Munk function.

Table 4.3: Band gap values for TiO_2 nanoparticles calcined at various temperatures.

.

Sample Code	Band gap (eV)	Urbach energy (eV)
T1	3.12	0.113
T2	3.18	0.082
T3	3.16	0.080
T4	3.15	0.073

Considerable difference in the band gap of samples is not observed. In contrast to this, the Urbach energy shows a decreasing trend with the increase of calcination temperature. The as prepared sample T1 yields maximum Urbach energy of 0.113 eV, indicating its high structural randomness. T4 sample has minimum E_u of 0.073 eV, indicating that the increasing calcination

process might have led to structural rearrangements and reduction of the stresses and thereby decreasing the entropy of the system.

4.1.3 FTIR analysis

FTIR patterns of TiO_2 nanoparticles calcined at various temperautres are shown in Fig. 4.3. To improve the visibility, FTIR patterns of the samples are plotted in finger print region of 2000-400 cm^{-1}. In all the samples, the broad band in the range of 3600 – 3200 cm^{-1} in the group frequency region (not shown in Fig. 4.3) belongs to the stretching vibrations of hydroxyl groups [8]. The band at 1622 cm^{-1} corresponds to the bending vibrations of surface adsorbed water molecules [9, 10]. The intensity of this band decreases with increasing calcination temperature.

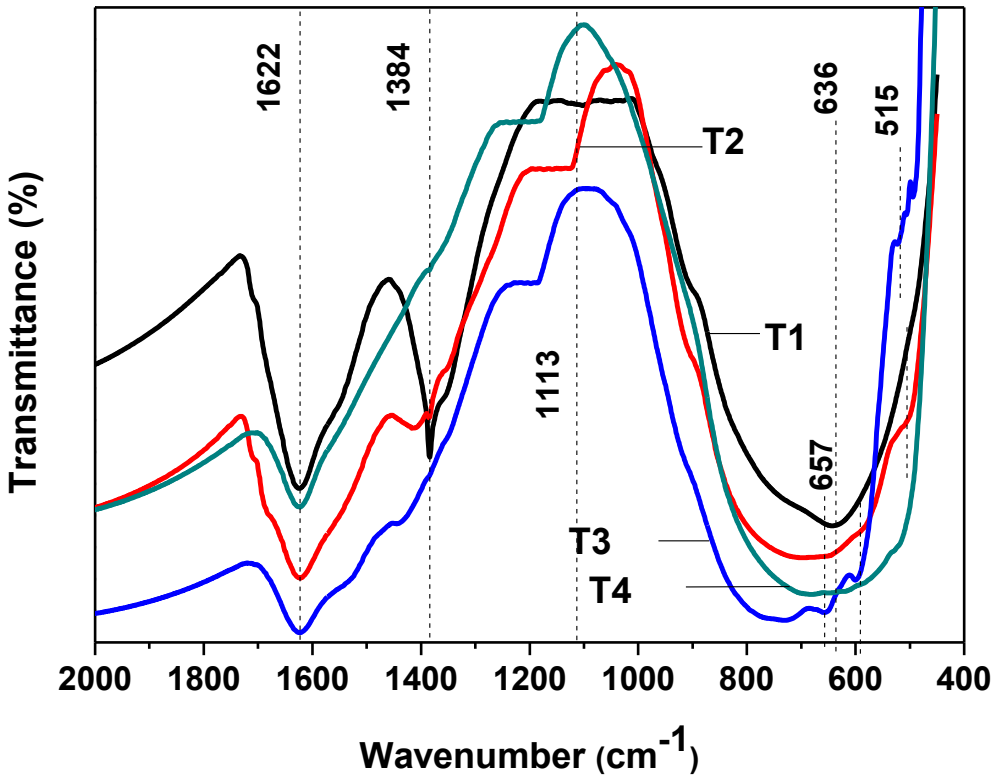

Figure 4.3: FTIR patterns of TiO_2 nanoparticles calcined at various temperatures.

The increase in calcination temperature increases the crystallite size which in turn decreases the surface area for adsorption of water molecules. Also, the nanoparticles having high specific area

like T1 sample can adsorb many water molecules on specific active sites on the surface and can form Ti^{4+}–OH_2 [11]. When the sample is given heat treatment at high temperature, the H-O-H bonds attached to Ti^{4+} get dissociated and the negatively charged O^{2-} takes part in formation of new bonds with Ti^{4+} ions. It results in formation of Ti-O bonds [11] which may cause increase in the intensity of strong band in range of 800–400 cm^{-1} associated with characteristic vibrational modes of TiO_2 with increasing calcination temperature [4]. The band between 1300-1500 cm^{-1} indicates the presence of organic materials in the sample attributed to the sol-gel fabrication technique, in which organic precursors are used [8]. The band at 1384 cm^{-1} is due to the symmetric bending vibrations of CH_3 groups [12]. This band gets diffused with increasing calcination temperature due to the removal of organic residues during heat treatment. The band between 1200 cm^{-1} to 1022 cm^{-1} is due to the Ti-O-Ti vibrations [4]. The strong band in range of 800–400 cm^{-1} is associated with characteristic vibrational modes of TiO_2, which is shifting towards higher wavenumber with increasing calcination temperature. This indicates the strengthening of bonds due to the structural rearrangements with increasing calcination temperature.

4.1.4 Raman analysis

Fig. 4.4 shows the Raman spectra of TiO_2 nanoparticles calcined at various temperatures. Raman spectroscopy is widely used technique to find and distinguish metal-oxide vibrations (M-O and M-O-M bonds) in the low wavenumber [13]. The anatase phase of TiO_2 has tetragonal structure with six Raman active modes (A_{1g} + 2B1g + 3Eg) at 144 cm^{-1} (E_g), 197 cm^{-1} (E_g), 399 cm^{-1} (B_{1g}), 513 cm^{-1}(A_{1g}), 519 cm^{-1} (B_{1g}), and 639 cm^{-1} (E_g) [14]. In the present study, we get the bands at 397 cm^{-1} (B_{1g}), 515 cm^{-1} (A_{1g}) and 641 cm^{-1}(E_g) which are ascribed to the anatase phase

of TiO_2. The bands at 247 cm^{-1} (A_{1g}), 318 cm^{-1} (B_{1g}) and 366 cm^{-1} (B_{2g}) are ascribed to the brookite phase of TiO_2 [15].

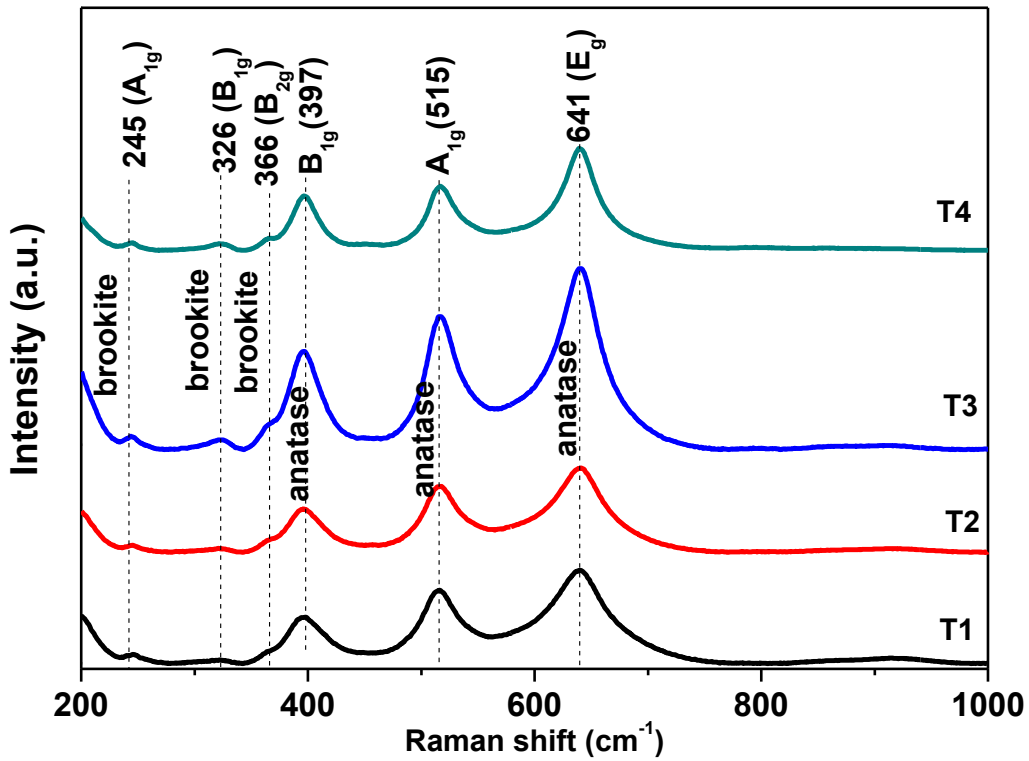

Figure 4.4: Raman patterns of TiO_2 nanoparticles calcined at various temperatures.

The results obtained from Raman spectra are in correlation with XRD and FTIR results. The XRD results (Fig. 4.1) indicate that the peak of brookite phase is very small. Similar results are obtained in Raman spectroscopy. Raman spectra further support the observed FTIR results viz. the strong bands at 515 and 641 cm^{-1} corresponding to Ti-O, Ti-O-Ti stretching vibrations, which are ascribed as weak bands in the FTIR spectra.

4.1.5 TGA analysis

Thermogravimetry analysis (TGA) has been performed to investigate the impact of calcination temperature on the thermal stablity of the samples. The TGA curves of T1, T2, T3 and T4

samples, at single heating rate of 10 ^{o}C/min in argon atmosphere (200 ml/min) are presented in Fig. 4.5 (a). Also, the thermal decomposition parameters involved in each stage of decomposition are determined from TGA curves. The mass loss observed in each stage of thermal decomposition of all the samples is presented in Table 4.4. Fig. 4.5 (a) clearly indicates that the thermal decompositon of all the samples occurred in four different stages. In stage 1 (~ 30 – 200 ^{o}C), the observed mass loss is attributed to the water loss and the degradation of organic chemicals [16]. The prominent mass loss in stage 1 has been observed in T1 sample, as evident from Table 4.4. The results agree well with FTIR results as the FTIR spectra show the presence of more prominent water peaks in T1 sample at 1620-1635 cm^{-1}.

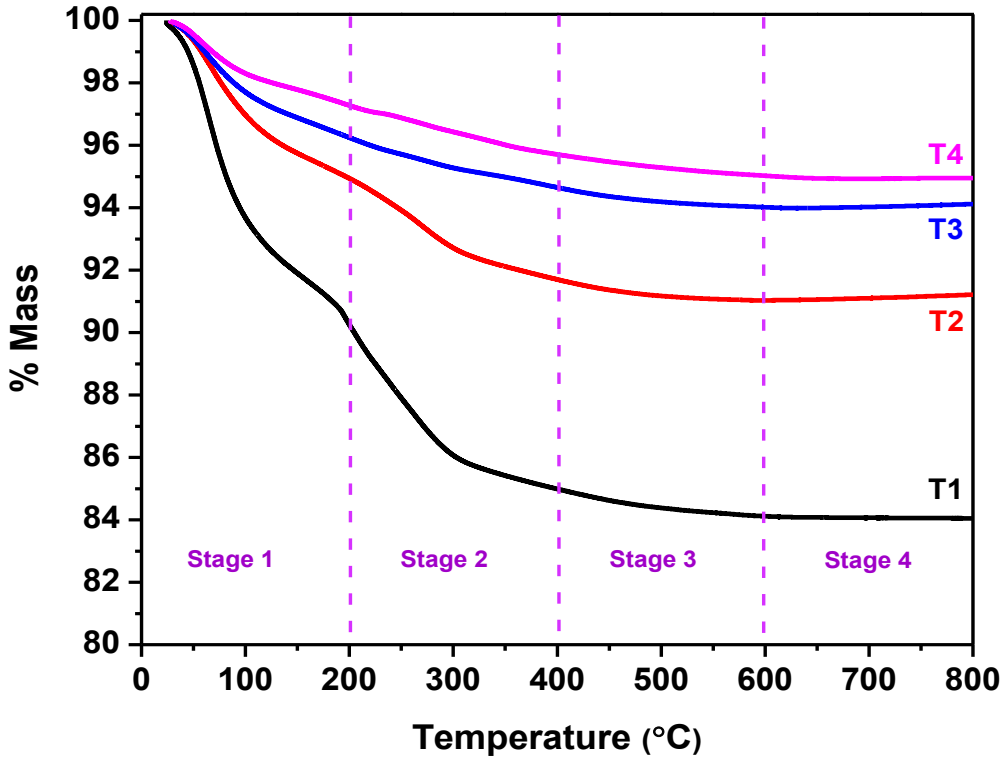

Figure 4.5 (a): Thermograms of TiO_2 nanoparticles calcined at various temperatures.

The mass loss observed in stage 2 (~ 200 – 400 ^{o}C) is attributed to the degradation of organic chemicals with strong bond [16]. It is observed that the mass loss due to the organic materials

residue decreased with increase in calcination temperature due to removal of organic matter with heat treatment. Similar trends are also observed in FTIR results as discussed in previous section. The mass loss observed in stage 3 (~ 400 - 600 ^{o}C) and stage 4 (~ 600 - 800 ^{o}C) is almost negligible. The total mass loss at 700 ^{o}C in T1, T2, T3 and T4 sample is approximately 17, 10, 7 and 5 %, repectively. As the calcination temperature increases, the total mass loss with temperature decreased.

Table 4.4: The mass loss obseved at each stage of thermal decomposition of all samples.

Sample Id	Mass loss (%)			
	Stage 1	**Stage 2**	**Stage 3**	**Stage 4**
T1	10	6	0.8	0.1
T2	5	4	0.7	0
T3	4	2	0.6	0
T4	3	1.6	0.7	0

Furthermore, kinetic parameters i.e. activation energy, pre-exponential factor and reaction mechanism are also determined for all the samples by employing Coats and Redfern method [17]. This method is an integral method, which can be expressed as:

$$ln\left(\frac{g(\alpha)}{T^2}\right) = ln\left(\frac{AR}{\beta E_a}\right) - \frac{E_a}{RT} \quad (4.7)$$

where, α is the degree of conversion, $g(\alpha)$ is the integral function of α, β is the heating rate, A is the pre-exponential factor, E_a is the activation energy, R is the gas constant (8.314 J K^{-1} mol^{-1}) and T is the absolute temperature.

The slope of the linear fitted curve between $ln\left(\frac{g(\alpha)}{T^2}\right)$ and $\frac{1000}{T}$ gives the value of activation enegy (E_a) and the pre-exponential factor (A) is calculated from the intercept. However, it is essential to determine appropriate value of $g(\alpha)$ to evaluate kinetic paramters accurately [18]. In

order to identify appropriate $g(\alpha)$ various reaction mechansim have been proposed [19], as tabulated in Table 4.5. The selection of $g(\alpha)$ calculated from each reaction mechanism depends on the value of co-relation factor.

Table 4.5: Various reaction mechanisms of thermal decomposition process in a reaction.

Reaction Mechanism	**Integral form $g(\alpha)$**
D_1 (1 – D diffusion)	α^2
D_2 (2 – D diffusion)	$\alpha + (1-\alpha)\,(ln(1-\alpha))$
D_3 (3 – D diffusion)	$(1-(1-\alpha)^{1/3})^2$
D_4 (Ginstling-Brounshtein)	$1 - 2\alpha/3 - (1-\alpha)^{2/3}$
F_1 (First order)	$-ln(1-\alpha)$
F_2 (Second order)	$1/(1-\alpha)$
F_3 (Third order)	$1/2(1-\alpha)$
R_1 (one – dimensional movement)	α
R_2 (contracting area)	$1-(1-\alpha)^{1/2}$
R_3 (contracting volume)	$1-(1-\alpha)^{1/3}$

Fig. 4.5 (b) – 4.5 (e) shows the linear fitted curves corresponding to various reaction mechanism for all the samples. The best linear fiting (R^2 ~ 0.8) was observed when D3 reaction mechanism dominates the thermal decomposition process of all the samples. This implies that the reaction mechanism remains identical (D3 mechanism) for all the samples. The activation energy and pre-exponential factor calculated from these curves (Fig. 4.5 (b) – 4.5 (e)) are presented in Table 4.6. The activation energy of T1, T2, T3 and T4 samples is found to be 21.94, 21.62, 19.11 and 18.19, respectively. The activation energy decreased from T1 to T4 samples, as evidenced from the Table 4.6. It is evident from thermal kinetic study that among calcined samples (T2 – T4), T2 sample shows higher thermal stablity and exhibit higher activation energy (21.62 kJ/mol). The

reason behind higher stabity of T2 sample is higher anatase phase content as compared to other samples (Table 4.1). The results of thermal kinetics are in agrement with XRD, FTIR and Raman results. This indicates that the T2 sample is highly suitable for photocatalytic application at higher temperatures. In comparison to this, the activation energy values of TiO_2 nanopowders synthesized by Moghaddam et al. [20] had been reported to be 85.87 and 73.47 kJ/mol.

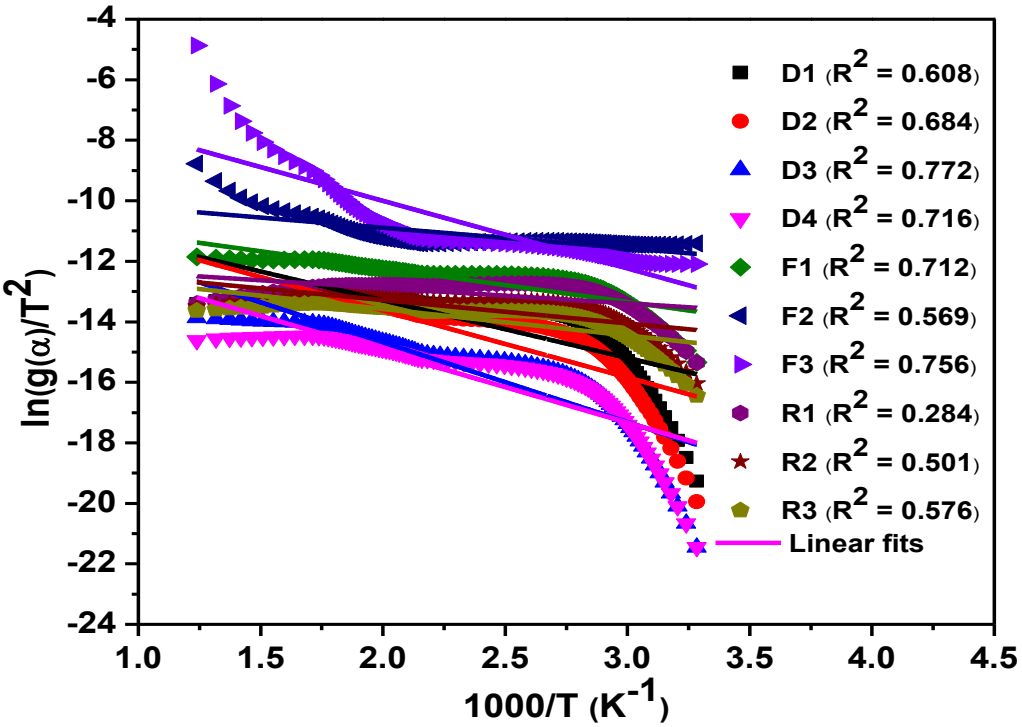

Figure 4.5 (b): Best linear fitted curves corresponding to various reaction mechanism for T1 sample.

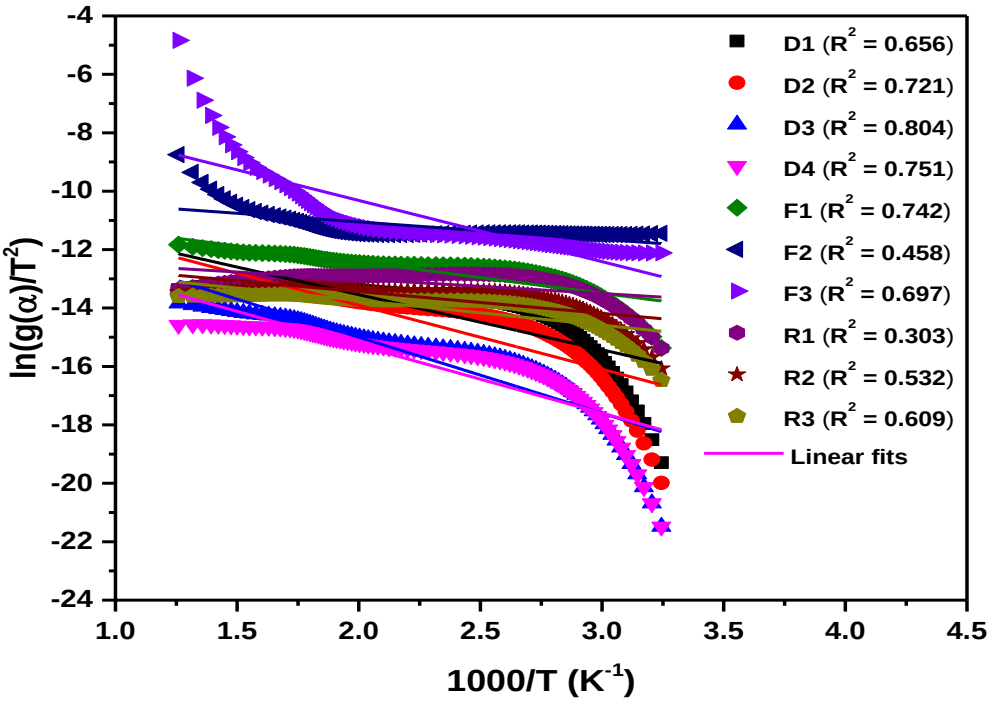

Figure 4.5 (c): Best linear fitted curves corresponding to various reaction mechanism for T2 sample.

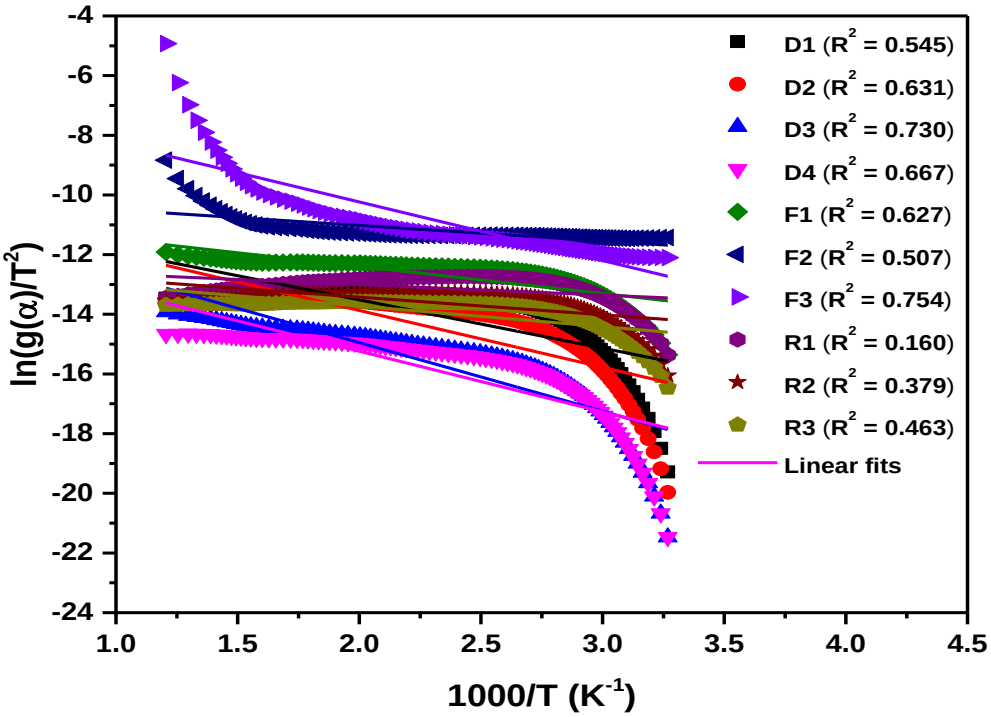

Figure 4.5 (d): Best linear fitted curves corresponding to various reaction mechanism for T3 sample.

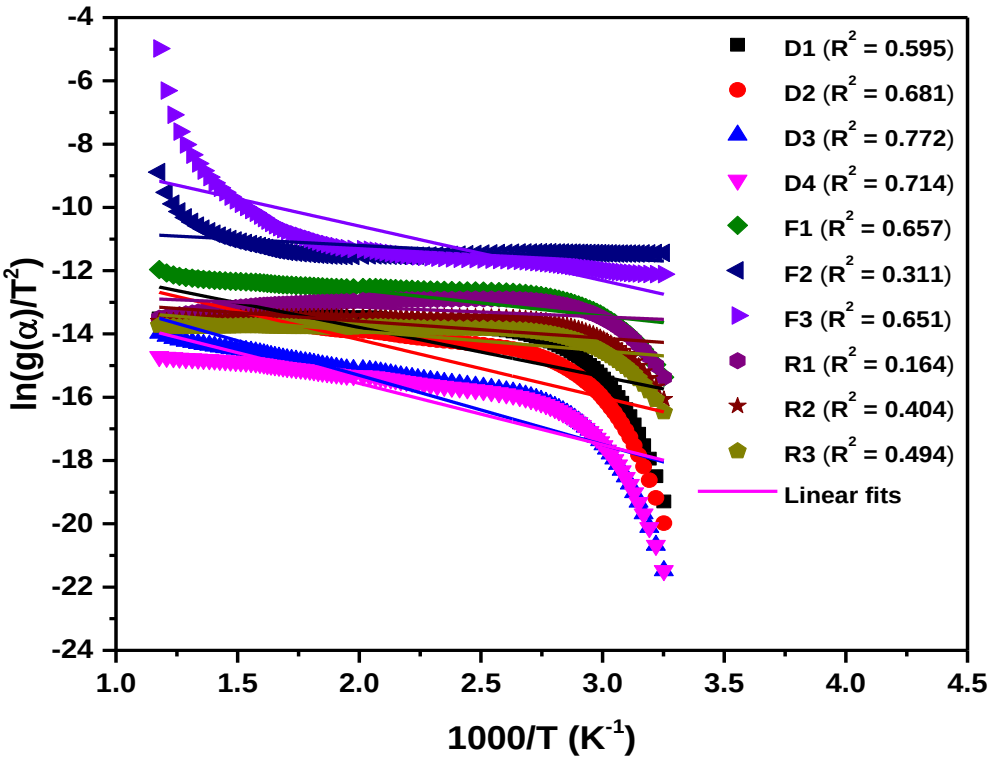

Figure 4.5 (e): Best linear fitted curves corresponding to various reaction mechanism for T4 sample.

Table 4.6: The value of activation energy and pre-exponential factor of all the samples.

Samples	Reaction mechanism	Activation Energy (kJ mol^{-1})	Pre-exponential factor (min^{-1})
T1	D3	21.94	3.14×10^{-6}
T2	D3	21.62	2.14×10^{-6}
T3	D3	19.11	1.39×10^{-6}
T4	D3	18.19	8.16×10^{-7}

4.1.6 HRTEM analysis

The HR-TEM micrographs of all the samples are shown in Fig. 4.6. It is evident from micrographs that aggregates of spherical nanoparticles have formed due to the very high surface free energy of small particles. Fig. 4.6 (b, d, f, h) shows the presence of lattice fringes of 0.35 nm corresponding to plane (101) of anatase phase which is also evident from XRD patterns of all the

samples. Selected area electron diffraction (SAED) pattern supports the nanocrystallinity of synthesized samples as shown in the inset of figure 4.6 (b, d, f and h). It can be observed that the diffraction spots present more sharper view as the calcination temperature is increased from 200 to 400 °C which is associated to the increased particle size of synthesized samples as shown in insets.

As the extent of agglomeration of nanoparticles is very high, Fig. 4.6 (a, c, e, g) are being considered for particle size distribution calculations in which the mean particle size is obtained with the help of *AxioVision Rel. 4.9.1.0* [21]. The mean particle size obtained for T1, T2, T3 and T4 sample is found to be 5.5, 5.1, 7.4 and 9.7 nm, respectively. The plot of frequency of particles against logerathmic particle size instead of the partcile size provides a good approximation of particle size distribution of synthesized samples. The size of the nanoparticle follows the lognormal distribution function [21] which is as follows,

$$f(d) = \frac{1}{\sqrt{2\pi}.\sigma.d_i} e^{-\left(\frac{(log(d_i)-\mu)^2}{2\sigma^2}\right)} \tag{4.8}$$

where $\mu = \frac{\sum log(d_i)}{\sum n_i}$; and $\sigma = \sqrt{\frac{\sum(log(d_i)-\mu)^2}{\sum n_i}}$

where *f(d)* designates the lognormal distribution of particle size, d_i represents the size of i^{th} particle of TiO_2, $\sum n_i$ is the total number of particles in consideration, μ is mean diameter and σ is the standard deviation of particle size. Fig. 4.7 shows the distribution of nanoparticles of all the samples.

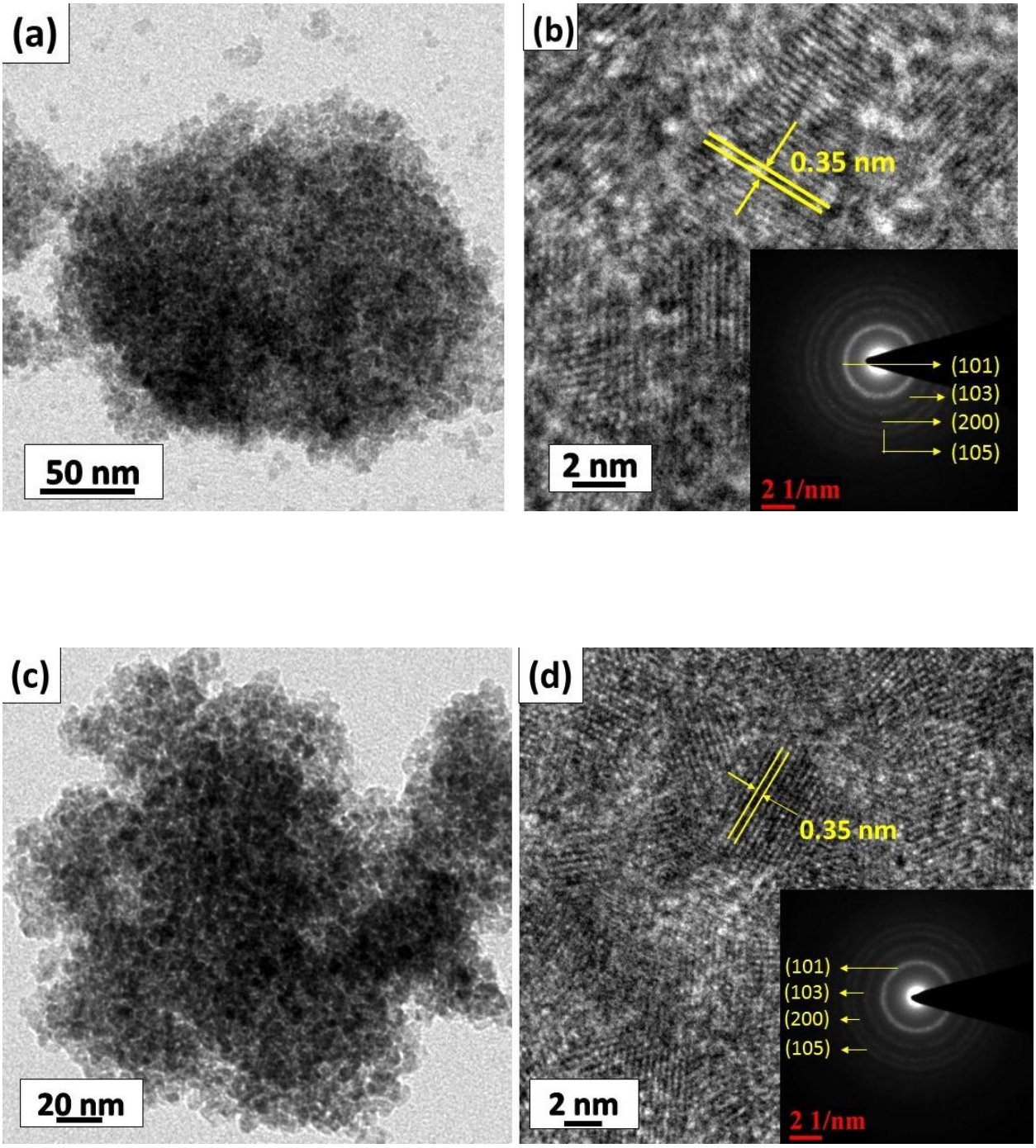

Figure 4.6 (i): HRTEM micrographs along with selected area diffraction patterns of T1 (a, b), T2 (c, d) samples.

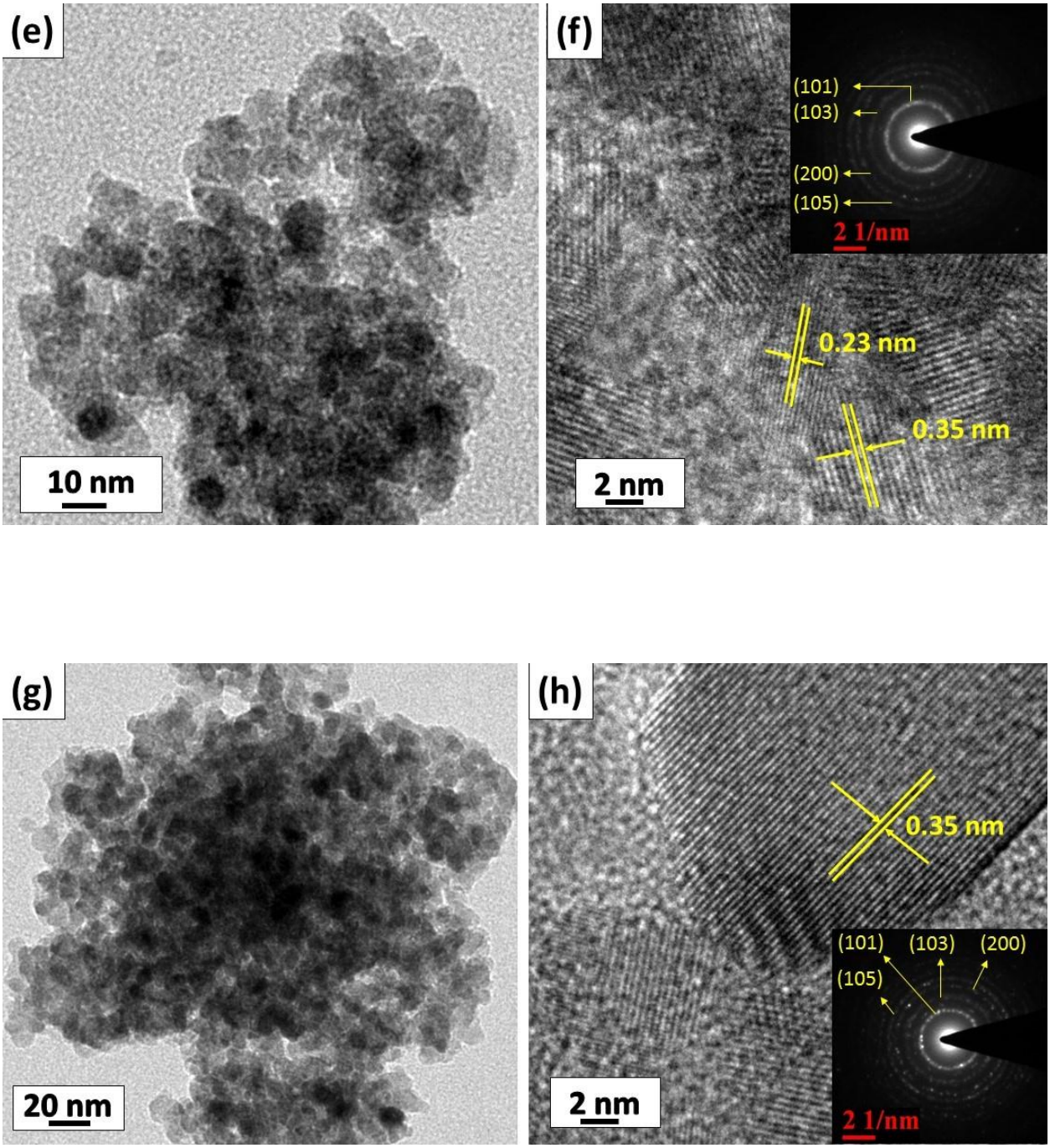

Figure 4.6 (ii): HRTEM micrographs along with selected area diffraction patterns of T3 (e, f) and T4 (g, h) samples.

$$f(d) = \frac{1}{\sqrt{2\pi}.\sigma.d_i} e^{-\left(\frac{(log(d_i)-\mu)^2}{2\sigma^2}\right)} \quad (4.8)$$

where $\mu = \frac{\sum log(d_i)}{\sum n_i}$; and $\sigma = \sqrt{\frac{\sum(log(d_i)-\mu)^2}{\sum n_i}}$

where *f(d)* designates the lognormal distribution of particle size, d_i represents the size of i^{th} particle of TiO_2, $\sum n_i$ is the total number of particles in consideration, μ is mean diameter and σ is the standard deviation of particle size. Fig. 4.7 shows the distribution of nanoparticles of all the samples.

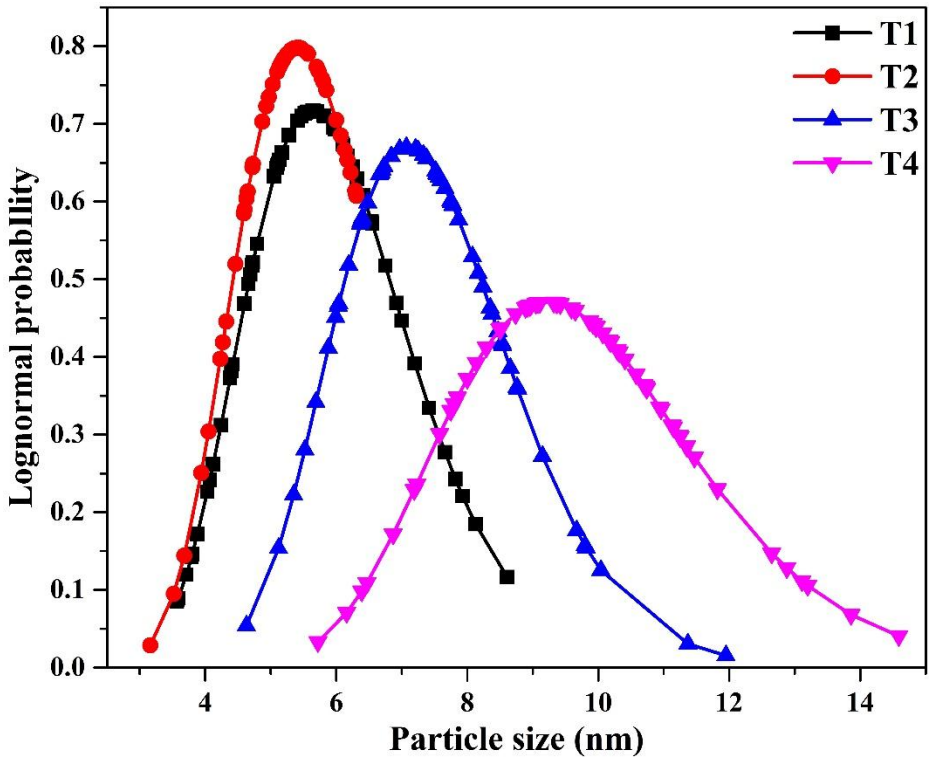

Figure 4.7: Particle size distribution of nanoparticle's size fitted with lognormal of T1, T2, T3 and T4 samples.

The maxima of the bell shaped distribution have a tendency to shift towards higher particle size when calcination temperature is increased. The maximum probable average size of nanoparticles may differ from other measuring technique due to the agglomeration of nanoparticles. The mean particle size of T2 sample is smallest i.e 5.1 nm. Moreover, particles of size 5.1 nm are maximum in number which can be interpreted from Fig. 4.7. This factor can play an important role in its photocatalytic activity. The average particle size of samples determined from XRD analysis is comparable with HRTEM results.

4.1.7 Photoluminescence analysis

Photoluminescence spectoscopy (PL) describes the transfer behaviour of photoinduced electron and hole pairs in the semiconductors and their recombination rate. Lower the intensity of PL spectra, lower is the recombination of electron hole pairs [9]. Fig. 4.8 shows the PL spectra of TiO_2 nanoparticles calcined at various temperatures and recorded at room temperature with the excitation wavelength of 350 nm. The emission spectra of all the samples give similar peak position, shape and with only difference in the intensity. The blue emission peak at 457 and green emission peak at 537 are due to color centres associated with oxygen vacancies [6]. The broad luminescence spectrum in the visible region is attributed to the electronic transition mediated by the defect levels, such as oxygen vacancies in the forbidden band gap [6]. Both radiative and non-radiative centres contribute to the PL emission intensity. Radiative recombination increases the emission intensity, while non radiative emission decreases the intensity. The decrease in PL intensity in T2 sample is due to the defects that act as non-radiative centres. The maximum PL intensity in T4 sample is due to the removal of some of the defects that act as non radiative centres with increasing calcination temperature. The lower PL intensity

of T2 sample reveals lower recombination of electron hole pairs and is regarded as an important factor in the photocatalytic properties.

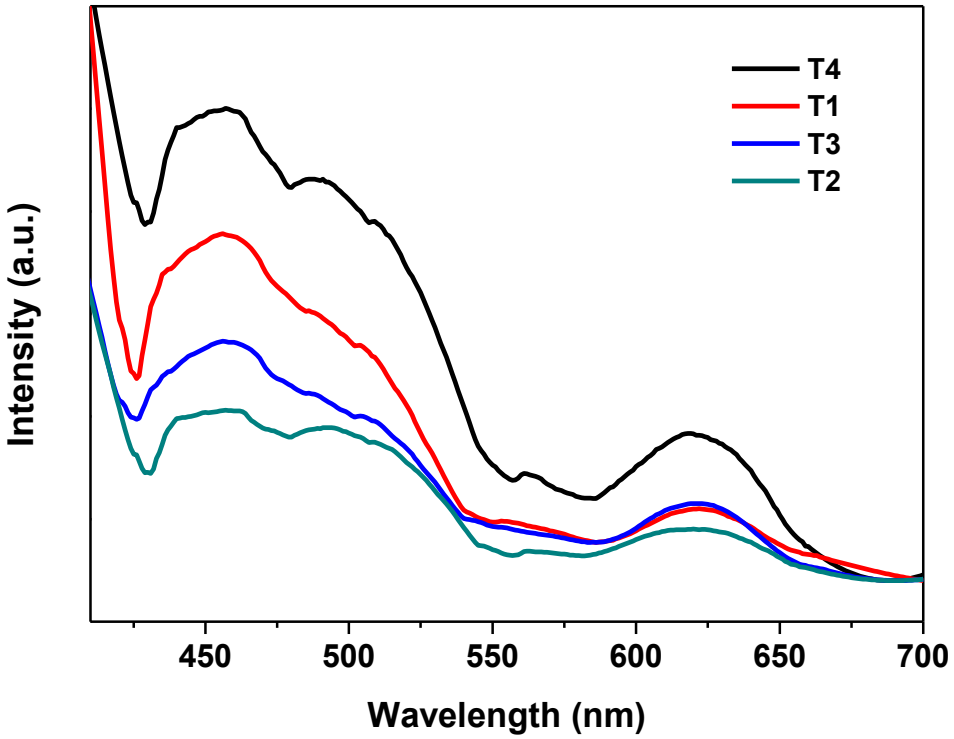

Figure 4.8: Photoluminescence spectra of TiO_2 nanoparticles calcined at various temperatures at excitation wavelength of 350 nm.

4.1.8 Photocatalytic degradation of diethy phthalate

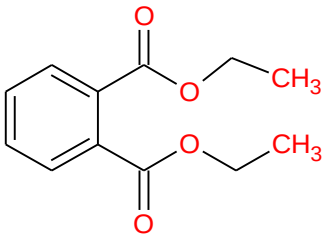

Figure 4.9: Chemical structure of diethyl phthalate.

The photocatalytic activity of samples is determined in terms of degradation of diethyl phthalate. The structure of diethyl phthalate is given in Fig 4.9. It is a highly conjugated system having pi-cloud on the benzene ring, the lone pairs on the oxygens and the p-orbitals on the carbonyl atoms

are all conjugated. The substituents are meta-directing and they are ortho to each other, so all positions in the ring are more or less equally deactivated. Due to conjugation, it is a stable compound and difficult to degrade [22].

Fig. 4.10 shows the linear plots of pseudo first order model for the degradation of diethyl phthalate in presence of photocatalysts and UV-vis light. The kinetics of pseudo first order photocatalytic degradation of diethyl phthalate is determined by Langmuir-Hinshelwood Kinetic model [23] as given in the following equation:

$$- ln\frac{C}{C_0} = k_{1app}t \qquad (4.9)$$

where C_o is initial concentration of diethyl phthalate, C is the concentration at irradiation time t in ppm and k_{1app} is the apparent rate constant. The linear plots of $-ln\ (C/C_o)$ vs time with higher correlation coefficients (close to unity), indicates that reactions follow pseudo first order kinetic model. The apparent constant (k_{1app}) is calculated from slope of $-ln\ (C/C_o)$ versus irradiation time. The apparent constants for the reaction using T1, T2, T3 and T4 samples are $4.2x10^{-3}$, $7.3x10^{-3}$, $5.8x10^{-3}$ and $3.4x10^{-3}$ min^{-1}, respectively. The highest apparent rate constant in case of T2 sample shows the highest photocatalytic activity of sample as compared to other samples. Many reports related to kinetic study of degradation of organic pollutants using TiO_2 are available in the literature. For example, In a study carried out by Sabry et al. [9], the apparent rate constant for the photocatalytic degradation of methylene blue using TiO_2 nanoparticles was found to be $6.0x10^{-3}$ min^{-1}.

Fig. 4.11 shows the linear plots of pseudo second order model for the degradation of diethyl phthalate in presence of photocatalysts and UV-vis light. The kinetics of pseudo second order photocatalytic degradation of diethyl phthalate is determined by following equation [24]:

$$\frac{1}{C} - \frac{1}{C_o} = k_{2app}t \quad (4.10)$$

where C_o is initial concentration of diethyl phthalate, C is the concentration at irradiation time t in ppm and k_{2app} is the apparent rate constant. The fitting of experimental data to the pseudo second order model is not so ideal with low correlation coefficient. The apparent constant (k_{2app}) is calculated from slope of *1/C* versus irradiation time. The apparent constants for the reaction using T1, T2, T3 and T4 samples are 2.56×10^{-4}, 7.0×10^{-4}, 4.50×10^{-4} and 1.85×10^{-4} min^{-1}, respectively. The apparent rate constants and correlation coefficients for pseudo first order and second order are given in Table 4.7

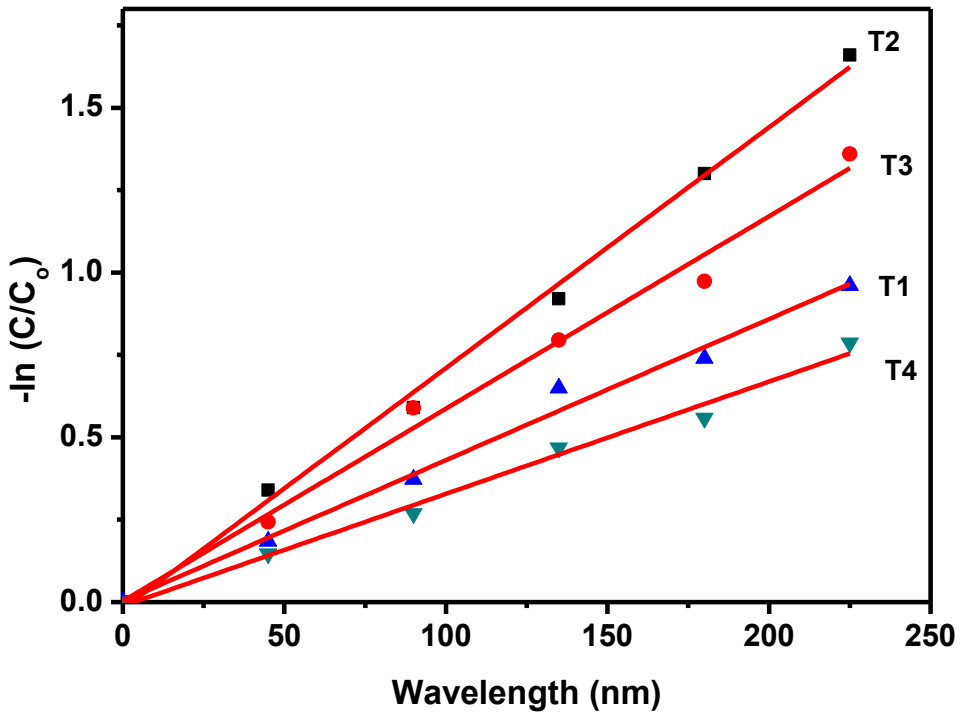

Figure 4.10: Linear plots of pseudo first order when C_o = 30 ppm, catalyst load = 1g/l.

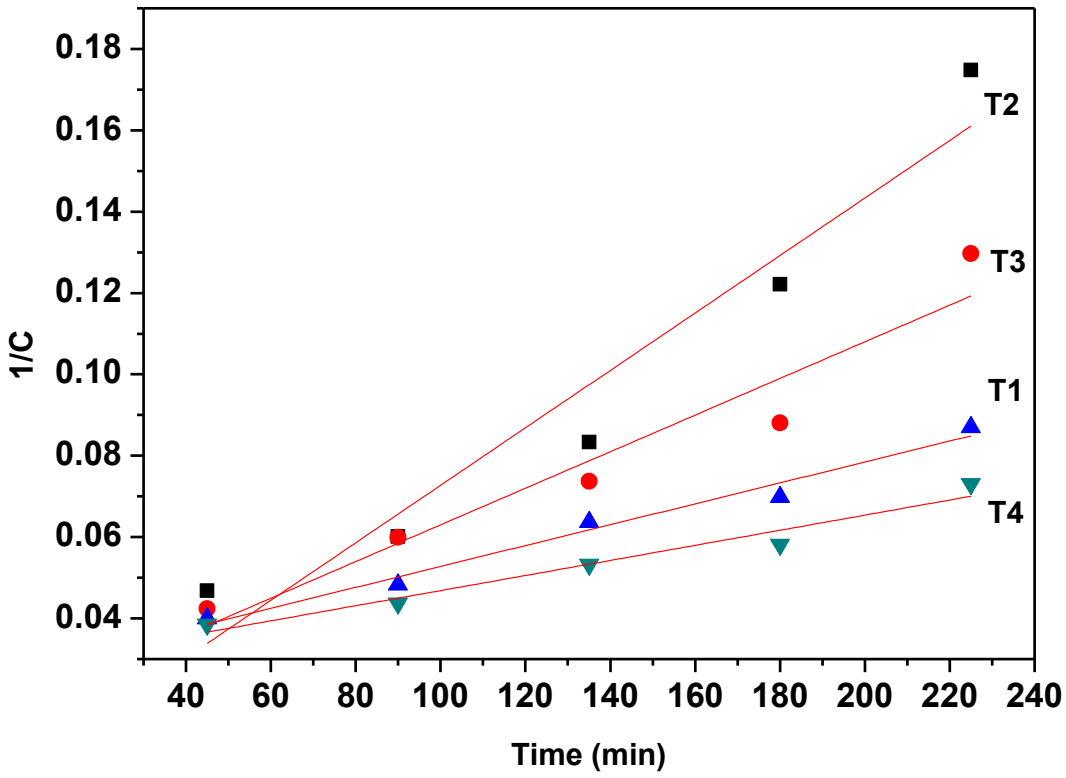

Figure 4.11: Linear plots of pseudo second order when C_o = 30 ppm, catalyst load = 1g/l.

Table 4.7: The value of activation enrgy, particle size and rate constant for all samples.

Sample Id	Activation Energy (kJ mol^{-1})	Particle size (nm)	Apparent reaction rate constant, k_{1app} (min^{-1}) (Pseudo first order)	R^2 (Pseudo first order)	Apparent reaction rate constant, k_{2app} (min^{-1}) (Pseudo second order)	R^2 (Pseudo second order)
T1	21.94	5.5	$4.2x10^{-3}$	0.9905	$2.56x10^{-4}$	0.9207
T2	21.62	5.1	$7.3x10^{-3}$	0.9958	$7.0x10^{-4}$	0.9163
T3	19.11	7.4	$5.8x10^{-3}$	0.9896	$4.50x10^{-4}$	0.9746
T4	18.19	9.7	$3.4x10^{-3}$	0.9895	$1.85x10^{-4}$	0.9507

The higher photocatalytic activity of T2 sample as compared to other calcined samples (T3&T4) can be attributed to the (a) small size (XRD and HRTEM analysis) (b) more disorder (Urbach energy) (c) presence of large number of surface adsorbed water molecules (FTIR and TGA analysis) (d) weak bonds (FTIR analysis) (e) low recombination of electron hole pairs (PL analysis). The small particle size in T2 sample leads to high specific area which in turn increases the reaction sites and photocatalytic activity. Higher disorderness in T2 sample leads to the localization of carriers and increases the photoluminescence life time due to non-availability of non-radiative recombination centers for localized carriers. Less recombination rate of electron-hole pairs in T2 sample increase the photocatalytic activity as there will be more number of electrons and holes, which are used in production of hydroxyl radicals. High rate of production of hydroxyl radicals leads to high photocatalytic activity.

T2 sample exhibits higher photocatalytic activity as compared to T1, although T1 sample has more disorder, more number of surface adsorbed water molecules and weak bonds. The other properties of T2 sample like smaller mean particle size (HRTEM analysis), crystallinity induced by calcination, lower recombination of electron-hole pairs and difference in its phase composition dominates for its higher photocatalytic activity. T1 sample exhibits more content of organic residues as compared to T2 (TGA analysis) which may act as deterrent for photocatalytic activity. The smallest particle size of T2 increases its surface active sites for photocatalytic reaction. The crystallinity can promote the charge transfer from center to the surface and then increase the photo catalytic activity [25]. Photocatalytic activity of a sample greatly depends on the recombination of electron hole pairs. Lower recombination of electron-hole pairs helps in increasing photocatalytic activity. Difference in phase composition of anatase to brookite in TiO_2 nanoparticles greatly affects the photocatalytic activity. There is a synergistic effect between

anatase and brookite. The conduction band of brookite is more negative as compared to anatase phase [23]. It ensures facilitated interfacial electron transfer (Fig. 4.11). Consequently, electrons moved to anatase are consumed for reduction of oxygen. This will lead to both charge separation and increased photocatalytic activity [25, 26].

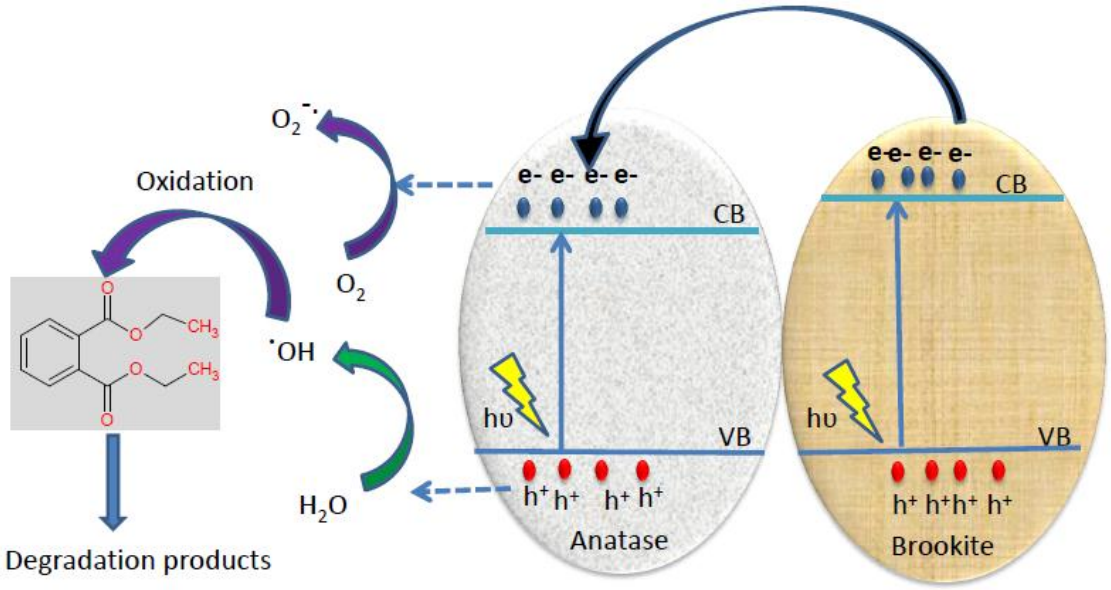

Figure 4.12: Electron transfer in anatase –brookite heterojunction.

Fewer studies are available in literature in which anatase-brookite hetrojunction is used for photocatalytic dergradation for organic polutants. For example, Kandiel et al. [25] used anatase-brookite naoparticles for the photocatalytic degradation of formaldehyde. Zhao et al. [27] synthesized samples having different anatase-brookite compostion. Sample having 75 % anatase and 25 % brookite was found to show highest photocatalytic activity. El-Sheikh et al. [28] found that anatase-brookite heterojunction having 61.8 % anatase and 38.2 % brookite shows highest photocatalytic activity for degradation of cylindrospermopsin. In contrast to this, optimum anatase to brookite ratio for highest photocatalytic degradation of diethyl phthalate is found to be 99 to 1 % for T2 sample in present study. Table 4.7 shows that on comparing calcined samples

only (T2-T4), the rate of reaction increases with decreasing particle size and increasing activation energy.

Fig. 4.12 shows the UV-vis spectral change of diethyl phthalate during irradiation in presence of T2 sample. Inset of Fig. 4.12 shows the UV-vis spectral change of diethyl phthalate in presence of T2 sample in dark. There is a negligible adsorption of around 1 % in 90 min. In UV-Vis spectrum of diethyl phthalate, two intense bands at wavelengths of 229 nm and 276 nm have been obtained. The decrease of absorption peak of diethyl phthalate at λ_{max}= 229 nm indicates degradation of diethyl phthalate during photo degradation. It works on the princple of absorption of light by TiO_2 to produce electron-hole pairs. The holes produced react with water and hydroxide ions to produce hydoxyl radicals (^{o}OH). The electrons react with oxygen to produce superoxide ions ($O_2^{-\cdot}$). The hydoxyl radicals, which are powerful oxidising agents causes photooxidation of organic pollutants to mineralize [29].

The percentage of degradation of diethyl phthalate is determined by the following equation [30]:

$$\%\ \text{Degradation} = \frac{C_o - C}{C_o} * 100 \qquad (4.11)$$

where C_o is the initial concentration of diethyl phthalate, C is the concentration at any time. Plot of % degradation and time is given in Fig. 4.13. The percantage degradation of diethyl phthalate is 95 % in 225 min.

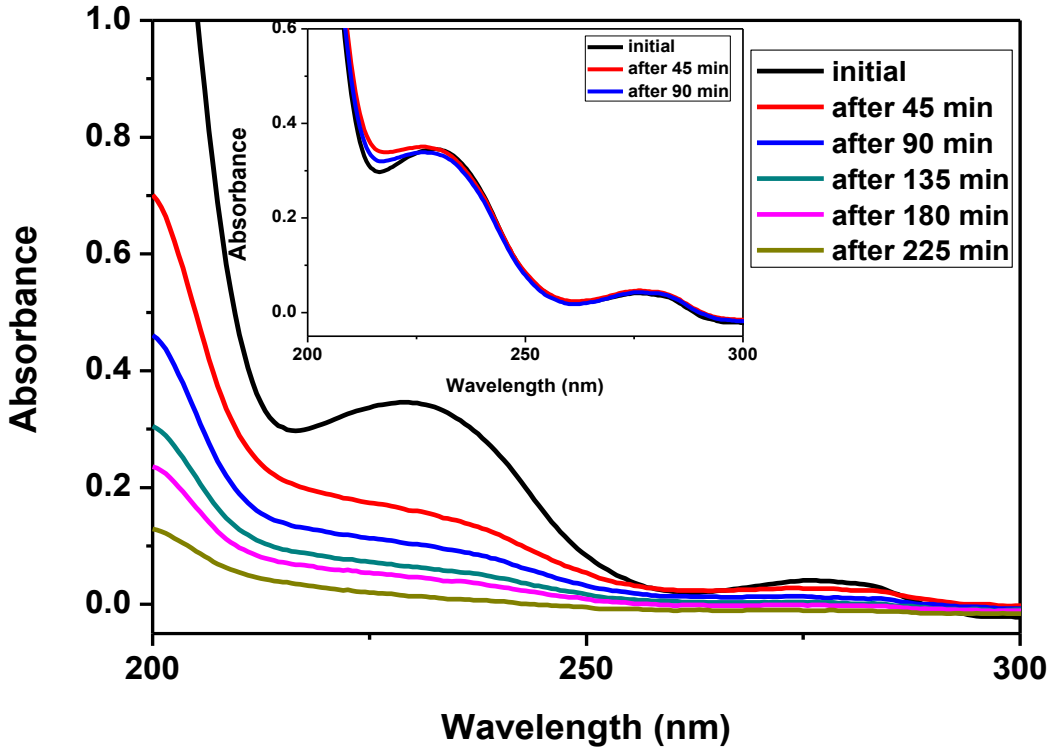

Figure 4.13: UV-vis spectral change of diethyl phthalate during irradiation in presence of T2 sample.

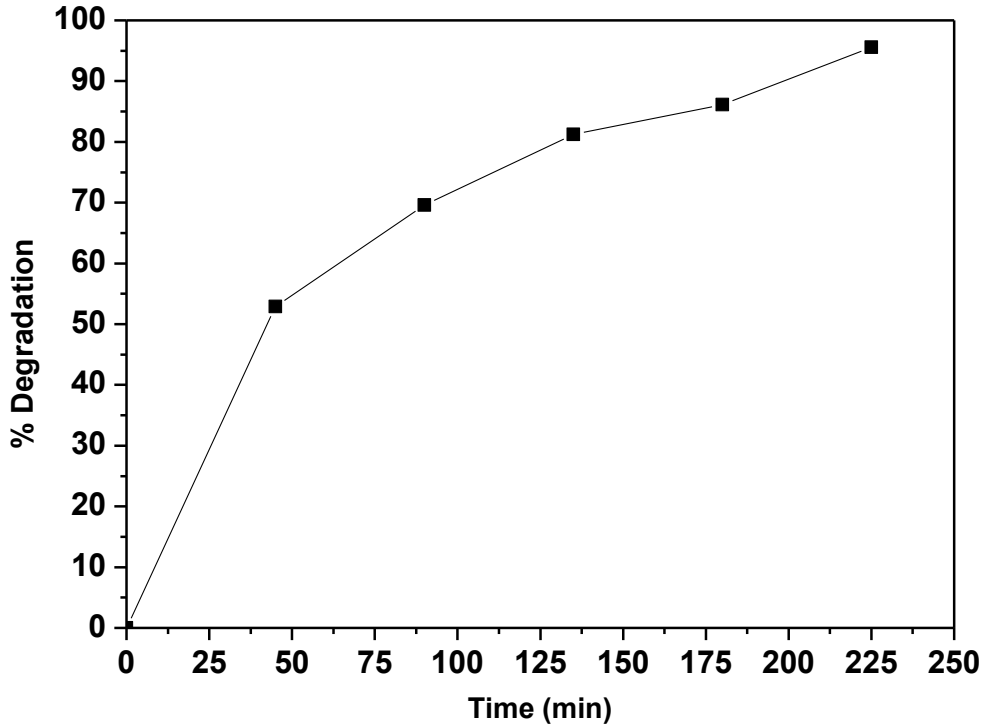

Figure 4.14: Change in % degradation of diethyl phthalate as a function of irradiation time.

4.1.9 Conclusions

TiO_2 nanoparticle are synthesized by sol gel method followed by calcination at different temperatures (200 to 400 ^oC). The particle size of samples obtained is in the range of 5-10 nm. Particle size of sample increases with increasing calcination temperature. XRD and Raman studies show the presence of anatase and minor brookite phase. The higher photocatalytic activity of T2 sample (calcined at 200 ^oC) as compared to other calcined samples at 300 and 400 ^oC (T3&T4) can be attributed to the (a) small size (b) more disorder (c) weak bonds. The rate of reaction increases with decreasing particle size and increasing activation energy. The optimum anatase-brookite ratio for high photocatalytic degradation of diethyl phthalate is found to be 99 to 1 % in present study. Hence, T2 can be a promising nanocatalyst candidate for removing organic pollutants from waste water.

References

1. Z. Li, S. Cong, Y. Xu, ACS Catal 4 (2014) 3273.
2. M. Crisan, M. Raileanu, N. Dragan, D. Crisan, A. Lanculescu, I. Nitoi, P. Oancea, S. Somacescu, N. Stanica, B. Vasile, C. Stan, Appl Catal A 504 (2015) 130.
3. B.D. Cullity, S.R. Stock (2001) Elements of X-ray Diffraction, 3rd edn Addision wesley-Publishing compony, Massachusetts.
4. A.K. Tripathi, M.K. Singh, M.C. Mathpal, S.K. Mishra, A. Agarwal, J Alloys Compd 549 (2013) 114.
5. X. Xue, W. Ji, Z. Mao, H. Mao, Y. Wang, X. Wang, W. Ruan, B. Zhao, J.R. Lombardi, J Phys Chem C 116 (2012) 8792.
6. S. Paul, A. Choudhary, Appl Nanosci 4 (2014) 839.
7. A. Hajjaji, A. Atyaoui, K. Trabelsi, M. Amlouk, L. Bousselmi, B. Bessais, M.A.E. Khakani, M. Gaidi, Amer J Anal Chem 5 (2014) 473.
8. P. Singla, O.P. Pandey and K. Singh K, Int J Environ Sci Technol 13 (2016) 849.
9. R.S. Sabry, Y.K. Al-Haidarie, M.A. Kudhier J. Sol-Gel Sci Technol 78 (2016) 299.
10. F.B. Dejene, M.O. Onani, P. Tarus, Physica B Condens Matter 480 (2016) 213.
11. B. Choudhury and A. Choudhury, Int Nano Lett 3 (2013) 55.
12. M.R. Derrick, D. Stulik, J.M. Landry, Infrared spectroscopy in conservation Science, The Getty conservation institute, Los Angles (1999).
13. L. OSterlund, John Wiley & Sons, Ltd, Chichester, UK. doi: 10.1002/9780470823996.ch8 (2010).
14. I. Ganesh, A.K. Gupta, P.P. Kumar, P.S.C. Sekhar, K. Radha, G. Padmanabham and G. Sundararajan, Scientific World J 2012 (2012) 1.

15. G. Tian, H. Fu, L. Jing, C. Tian, J Hazard Mater 161 (2015)1122.
16. M.M. Ba-Abbad, A.A.H. Kadhum, A.B. Mohamad, M.S. Takriff, K. Sopian, Int J Electrochem Sci **7** (2012) 4871.
17. A.W. Coats, J.P. Redfern, Nature 201 (1964) 68.
18. L. Nunez, F. Fraga, M.R. Nunez, M. Villanueva, Polymer 41 (2000) 4635.
19. J.M. Criado, J.A. Malek, Thermochim Acta 147 (1989) 377.
20. H.M. Moghaddam and S. Nasirian, Nanoscience Methods 1(2012) 201.
21. A. Gupta, G. Singla, O.P. Pandey, Ceram Int 42 (2016)13024.
22. J.J. Maitland, Organic chemistry, W.W. Nortan& Company, New York (2005).
23. G.M. Madhu, M.A. Raj and K.V. Pai, J Environ Biol 30 (2009) 259.
24. G. Raj, Chemical Kinetics, 9th edition, Krishna Parkahan, 2014.
25. T.A. Kandiel, L. Robben, A. Alkaima, D. Bahnemann, Photochem Photobiol Sci 12 (2014) 602.
26. V. Etacheri, C.D. Valentin, J. Schneider, D. Bahnemann, S.C. Pillai, J Photochem. Photobiol A Chem. 25 (2015) 1.
27. H. Zhao, L. Liu, J.M. Andinobc and Y.J. Li, Mater. Chem., A 1 (2013) 8209.
28. S.M. El-Sheikha, T.M. Khedra, G. Zhang, V. Vogiazib, A.A. Ismaila, K. O'Sheac, D.D. Dionysiou, Chem. Eng. J. In press. (2016).
29. L. Agartan, D. Kausuz, J. Park, A. Ozturk, Ceram Int 41 (2015) 12788.
30. M.R Shorabi, M. Ghavami, Desalination 252 (2010) 157.

Chapter 5
Results and discussion
Synthesis and characterization of Fe-doped, Cu doped and (Fe, Cu) codoped TiO_2 nanoparticles for the photocatalytic degradation of diethyl phthalate

Overview

The present chapter describes the studies of undoped, Fe-doped, Cu-doped and (Fe, Cu) co-doped TiO_2 nanoparticles prepared via sol-gel method. The samples were characterized for their structural, optical and thermal properties by X-ray diffraction (XRD), UV-vis absorption spectroscopy, Fourier transform infrared spectroscopy (FTIR), Thermogravimetric analysis (TGA), High resolution transmission electron microscopy (HRTEM) and photoluminescence (PL) techniques. The photocatalytic activity of samples is discussed in terms of the degradation of diethyl phthalate.

5.1 Introduction

TiO_2 has some limitations like high rate of electron-hole recombination, which leads to low quantum efficiency of photocatalytic reactions [1]. The wide bandgap of TiO_2 requires ultraviolet light for its application as catalyst [2]. Doping TiO_2 with transition metals is a promising way to extend the absorption of TiO_2 into the visible region. It also inhibits the recombination of electron-hole pairs [3]. Many transition metals like Fe, Cr, Mn, Co, Mo, Ni, Cu and Zn have been doped into TiO_2 to modify its band gap and photocatalytic activity [4-5]. The enhanced visible light photocatalytic activity of TiO_2 upon doping can be attributed to the band gap narrowing, formation of impurity energy levels within the band gap of TiO_2, formation of intrinsic defects (such as oxygen vacancies, interstitial Ti) and introduction of traps for electrons and/or holes [6]. In recent years, researchers have focused on doping of more than one transition metal ion in TiO_2. The improved photocatalytic activity of TiO_2 upon doping with two transition elements rather than single doped has been reported [6-7]. Yuan et al. [7] reported that Zn and Fe codoped TiO_2 exhibited two times improved photocatalytic activity than pure or single doped. Benjwal et al. [8] reported the improved photocatalytic activity of Zn-Mn codoped TiO_2 than undoped TiO_2. In the present chapter, the synthesis and characterzation of undoped, Fe-doped, Cu-doped and (Fe, Cu) codoped TiO_2 nanoparticles have been described for the photocatalytic degradation of diethyl phthalate. The undoped, 0.075 mol % Fe-TiO_2, 0.075 mol % Cu-TiO_2, (0.05 mol % Fe, 0.05 mol % Cu) codoped TiO_2, (0.075 mol % Fe, 0.075 mol % Cu) codoped TiO_2, (0.1 mol % Fe, 0.1 mol % Cu) codoped TiO_2 samples have been labeled as To, T2Fe, T3Cu, T4FeCu, T5FeCu and T6 FeCu, respectively. The results are presented in the preceding sections.

5.1.1 XRD analysis

Fig. 5.1 (a) shows the XRD patterns of undoped, Fe-doped, Cu-doped and (Fe, Cu) codoped TiO_2 samples calcined at 450 ^oC. XRD studies show the presence of anatase phase (ICDD No. 01-073-1764) with a small fraction of rutile phase (ICDD No. 00-001-1292) in all samples. The peaks in pristine TiO_2 observed at 2θ of 25.48^o, 38.01^o, 48.23^o, 54.12^o, 55.21^o, 62.87^o, 69.18^o, 70.44^o and 75.32^o corresponds to the (101), (004), (200), (105), (211), (204), (116), (220) and (215) planes of anatase phase, respectively. The diffraction peak at 2θ= 27.5^o corresponds to the rutile phase of TiO_2. No peaks corresponding to dopant oxides are observed in XRD patterns due to very low content of dopants and successful incorporation of dopants into the atomic level of TiO_2 [9].

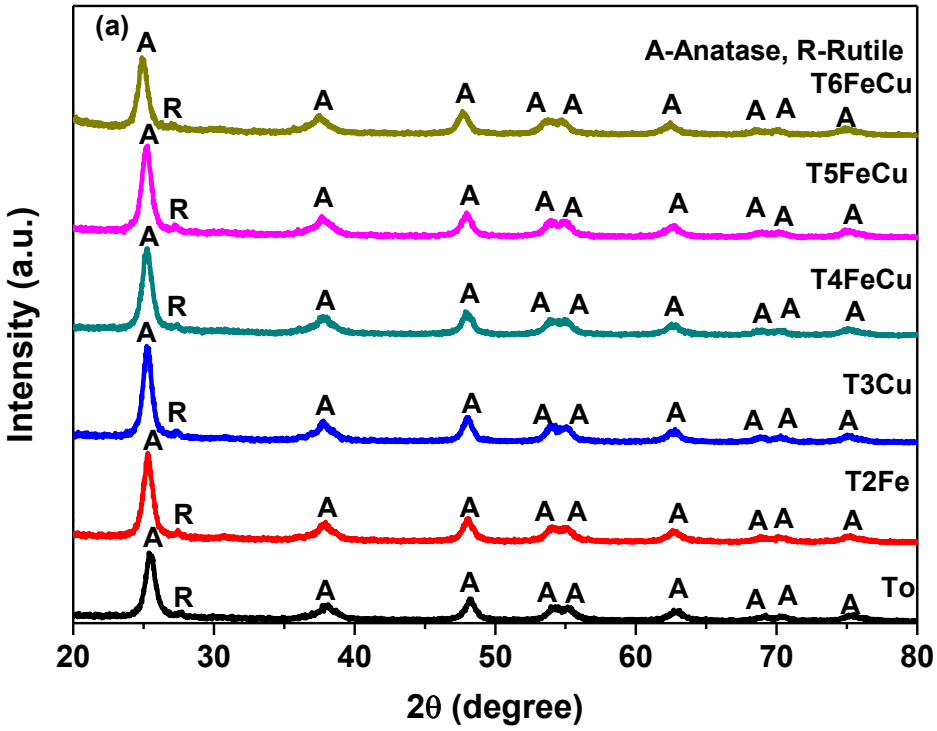

Figure 5.1 (a): XRD patterns of undoped, Fe-doped, Cu-doped and (Fe-Cu) codoped TiO_2 samples calcined at 450 ^oC.

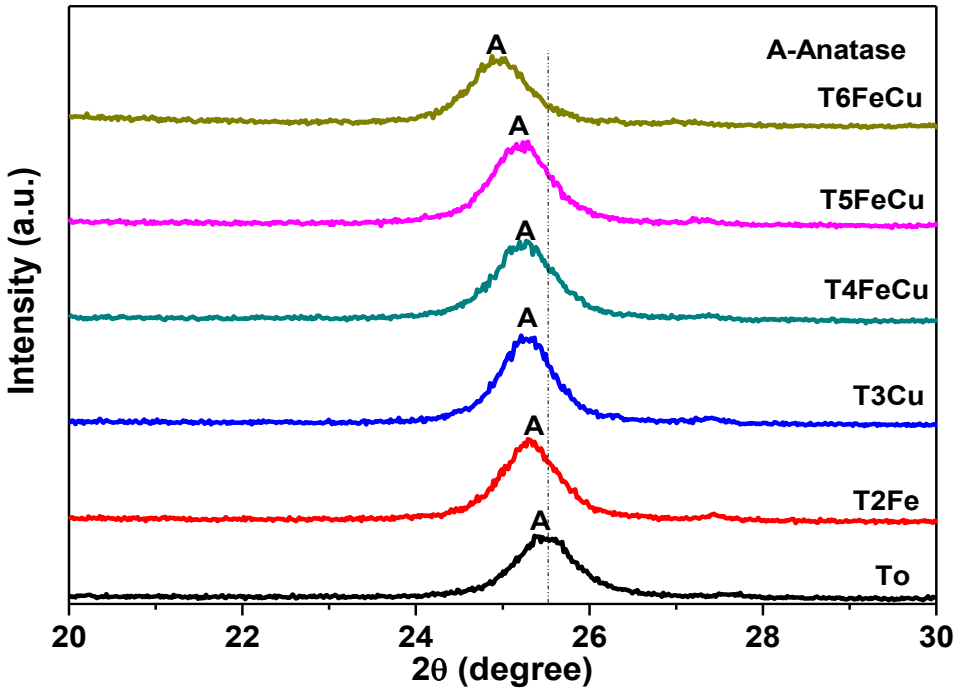

Figure 5.1 (b): XRD spectra demonstrating peak shift corresponding to the (101) plane of anatase phase.

From Fig. 5.1 (b) it is evident that for all the doped samples, the characteristic peak of anatase phase is shifting to lower 2θ values. The incorporation of dopants leads to the expansion of the crystalline lattice and results in structural distortion [10]. The increase in interplanar distance of anatase lattice shifts the diffraction peaks to lower angles according to Bragg's law [10]. The peak shift is an indirect evidence of successful doping into TiO_2 crystal lattice. The crystallite size of To, T2Fe, T3Cu, T4FeCu, T5FeCu and T6FeCu samples is found to be 10.77 nm, 11.20 nm, 12.31 nm, 10.59 nm, 10.76 nm and 11.14 nm, respectively. The crystallite size is determined by Scherrer equation [11] given in equation 4.1. Lattice parameters of the samples (given in Table 5.1) are calculated using equation 4.2. The lattice parameters are calculated using diffraction peaks corresponding to the (101) and (200) planes of anatase phase. The lattice parameters '*a*' and '*b*' remained almost constant upon doping. However, there is elogation along c-axis in all the doped samples as compared to undoped sample. This elongation is due to the fact

that dopants occupy body centered cubic (bcc) and face centered cubic (fcc) positions in the anatase structure [12].

Table 5.1: The structural parameters calculated from the XRD data corresponding to the characteristic peak (101) of anatase phase.

Sample	2θ (degree)	FWHM (degree)	d-spacing (Å)	Crystallite size (nm)	Lattice parameters (Å)	Unit cell volume ($Å^3$)	Density (g/cm^3)
To	25.49	0.7559	3.489	10.77	$a = b = 3.77$ $c = 9.229$	131.17	4.043
T2Fe	25.31	0.7264	3.515	11.20	$a = b = 3.783$ $c = 9.513$	136.14	3.895
T3Cu	25.27	0.6609	3.520	12.31	$a = b = 3.784$ $c = 9.592$	137.34	3.861
T4FeCu	25.25	0.7682	3.523	10.59	$a = b = 3.786$ $c = 9.620$	137.89	3.846
T5FeCu	25.21	0.7558	3.529	10.76	$a = b = 3.79$ $c = 9.67$	138.90	3.818
T6FeCu	24.95	0.7303	3.565	11.14	$a = b = 3.806$ $c = 10.25$	148.47	3.572

The significant structural changes are observed within TiO_2 due to incorporation of dopants ions. The ionic radius of Fe^{3+} (0.785 Å) and Cu^{2+} (0.87 Å) is larger than host Ti^{4+} (0.60 Å). The doping of subsitutional metal cation with valency less than +4 and higher ionic size would result in oxygen vacancies at the surface of anatase crystallites favourig strucural rearrangements [13]. The X-ray density of samples (given in Table 5.1) is calculated using equation 4.3.

5.1.2 UV-vis absorption analysis

Fig. 5.2 (a) depicts the UV-vis absorption spectra of undoped, Fe-doped, Cu-doped and (Fe, Cu) codoped TiO_2 samples calcined at 450 ^oC. The absorption edge in To sample corresponds to the band to band transition between O2p levels of valence band to Ti 3d levels of conduction band [12]. The optical absorption edge shows red shift in the doped samples as compared to the undoped sample. The red shift is attributed to the formation of new dopant energy levels within forbidden bandgap states of bare TiO_2. There are charge transitions between'd' electrons of metal ion and conduction or valence band of TiO_2 [6].

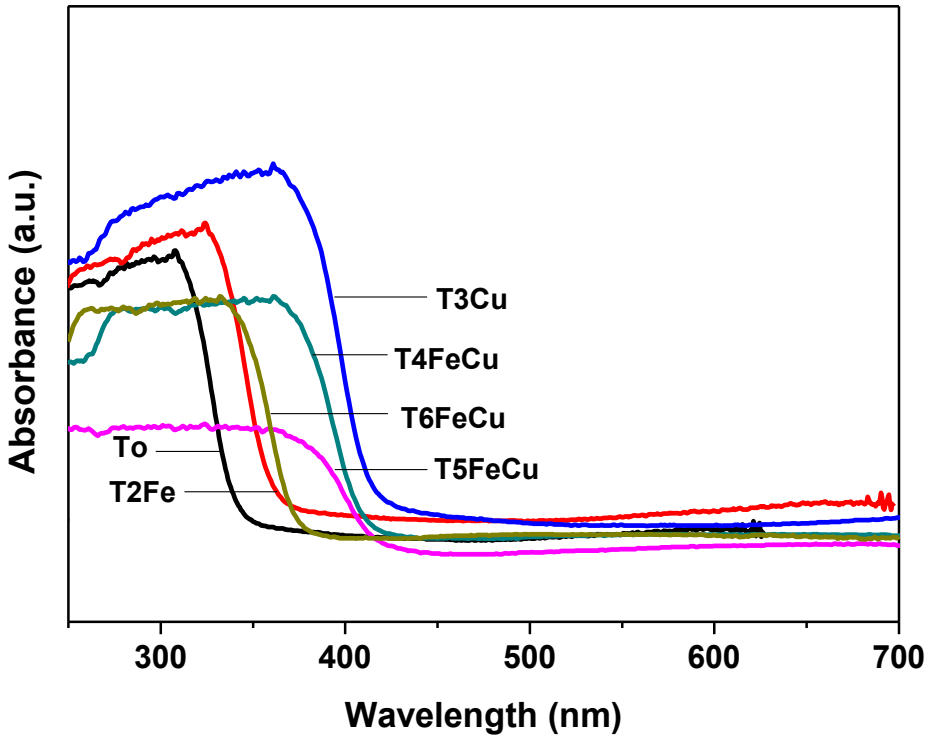

Figure 5.2 (a): UV-vis absorption spectra of undoped, Fe-doped, Cu-doped and (Fe, Cu) codoped TiO_2 samples calcined at 450 ^oC.

The optical band energy of the samples is determined by Tauc equation [14]. Tauc equation for for indirect allowed transition is

$$\alpha h\nu = B(h\nu - E_g)^2 \quad (5.1)$$

where α is absorption coefficient, h is Plancks constant, ν is frequency, E_g is band gap energy. Absorption coefficient (α) is determined by following equation:

$$\alpha = 2.303\ A / t \quad (5.2)$$

where A is absorbance, t is thickness of sample.

Photon energy (hν) is obtained by following equation:

$$h\nu\ (eV) = 1240 / [\text{incident wavelength (nm)}] \quad (5.3)$$

$(\alpha h\nu)^{1/2}$ is plotted against photon energy (hν) as shown in Fig. 5.2 (b). The linear portion of the obtained curves is extrapolated to have an intercept on the x axis. The value at intercept corresponding to $(\alpha h\nu)^{1/2} = 0$ is taken as the value of the band gap [15].

The band gap energy of To, T2Fe, T3Cu, T4FeCu, T5FeCu and T6FeCu samples is found to be 3.08, 2.85, 2.75, 2.53, 2.46 and 2.01, respectively. The decrease in band gap energy upon doping of TiO_2 with transition metals is supported by many researchers. Sood et al. [2] reported the band gap energy of 2.9 eV for 0.1 mol% Fe doped TiO_2 nanoparticles. Yadav et al. [16] reported the band gap of 2.89 eV for 1.0 mol% Cu doped TiO_2. Apiwong-ngarm et al. [17] reported the band gap energy of 2.73 eV for 0.5 mol% (Fe, Cu) codoped TiO_2.

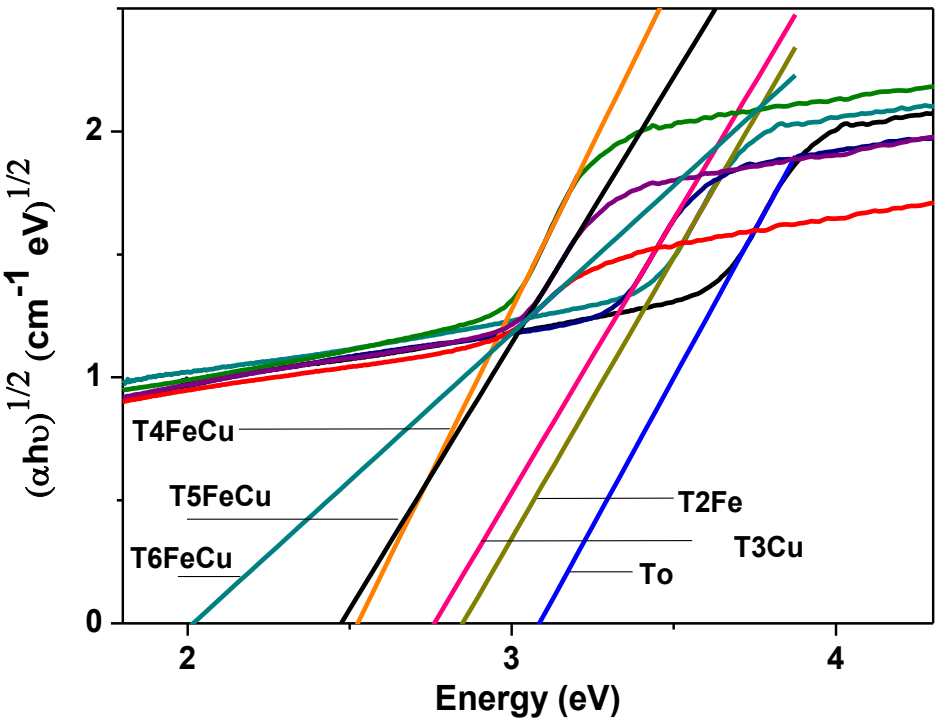

Figure 5.2 (b): Determination of band gap energy of undoped, Fe-doped, Cu-doped and (Fe, Cu) codoped TiO_2 samples using Tauc plot.

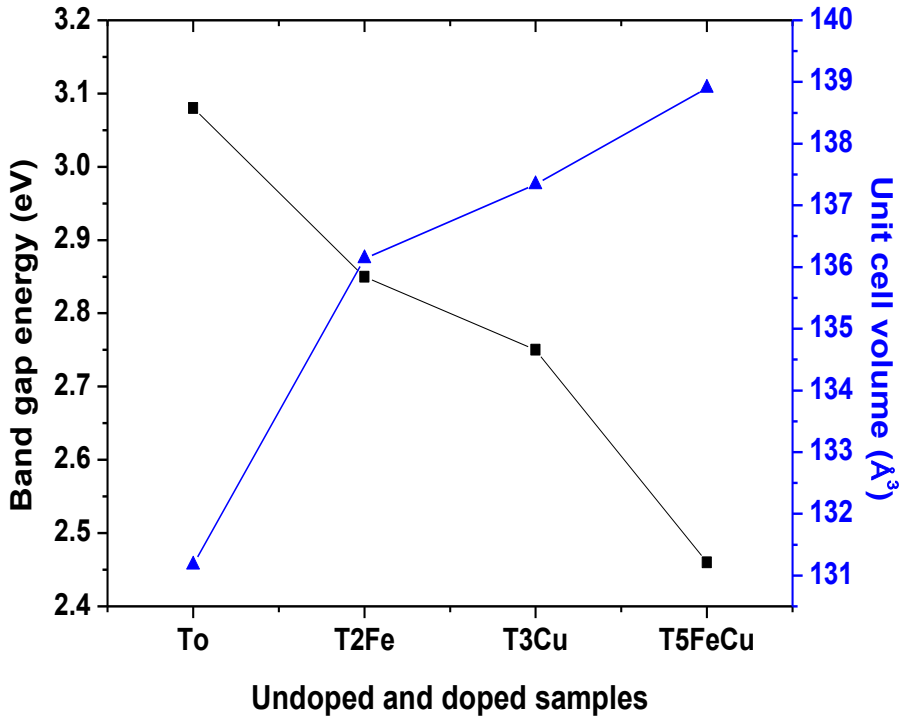

Figure 5.2 (c): Variation of band gap and unit cell volume with respect to doping.

From Fig. 5.2 (c), it can be observed that band gap energy decreases and corresponding unit cell volume increases with doping. It indicates that disorderness in the structure follows the trend Fe-Cu>Cu>Fe. The dopants may create their defect energy levels within the forbidden gap. This facilitates the absorption of electromagnetic waves at relatively lower energies. As a result, band gap energy of the material decreases.

5.1.3 FTIR analysis

FTIR patterns of undoped, Fe-doped, Cu-doped and (Fe, Cu) codoped TiO_2 samples calcined at 450 ^oC are given in Fig. 5.3. The broad band around 3363 cm^{-1} in all the samples is attributed to the stretching vibrations of hydroxyl groups [18]. The bands at 2932 cm^{-1} and 2846 cm^{-1} corresponds to the asymmetric and symmetric C-H stretches for methylene groups, respectively [19]. The band at 2347 cm^{-1} is attributed to atmospheric carbondioxide [19]. The band at 1629 cm^{-1} is due to the bending vibrations of surface adsorbed water molecules [2].

The band at 1384 cm^{-1} is attributed to the symmetric bending vibrations of CH_3 groups [19]. The occurrence of bands between 1300-1500 cm^{-1} and 2800-3000 cm^{-1} indicate the presence of small residue of organic materials in the sample [20]. The strong band in range of 800-400 cm^{-1} corresponds to the characteristic vibrational modes of TiO_2 [21]. This band is shifting towards lower wavenumber in doped samples. This indicates the weakening of bonds due to the structural rearrangements in doped samples. Introduction of dopant distorts the local symmetry of the lattice by inducing structural rearrangements in Ti-O-Ti environment. It is also supported by the X-rays diffraction results discussed in section 5.1.

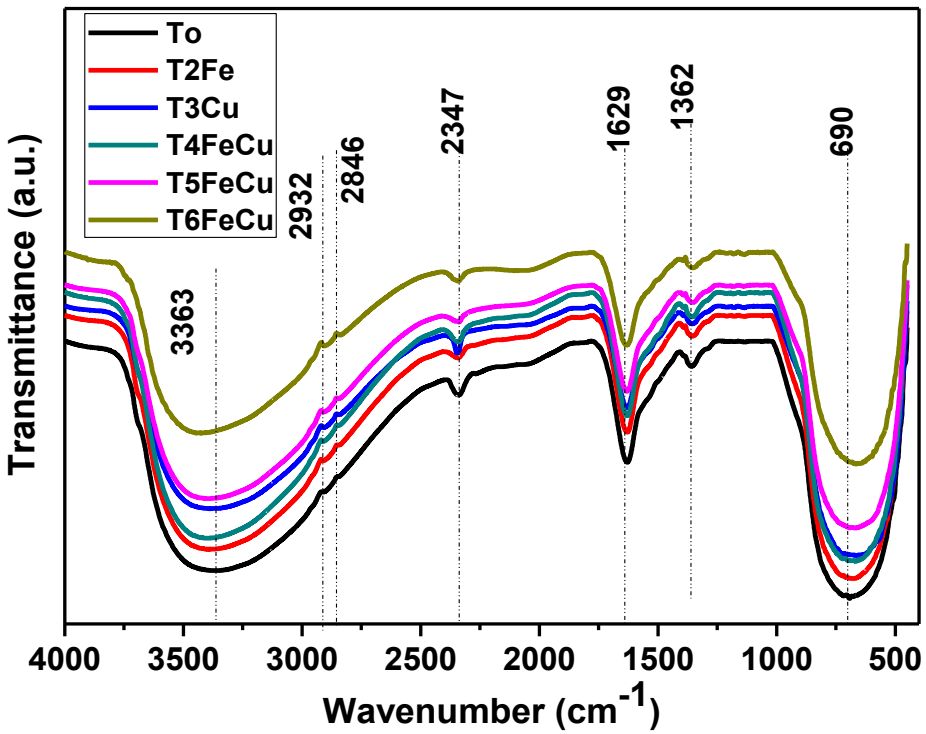

Figure 5.3: FTIR patterns of undoped, Fe-doped, Cu-doped and (Fe, Cu) codoped TiO_2 samples calcined at 450 ^oC.

Table 5.2: Peak assignment of various bands in undoped and doped samples.

Peak Position (cm^{-1})	Peak assignment
3363	stretching vibrations of OH groups [15]
2932	Asymmetric C-H stretches for methylene groups [16]
2846	Symmetric C-H stretches for methylene groups [16]
2347	Atmospheric carbon dioxide [16]
1622	bending vibrations of surface adsorbed H_2O molecules [2]
1384	Symmetric bending vibrations of CH_3 groups [16]
690	Bending vibrations of Ti-O-Ti bond of anatase phase [18]

5.1.4 TGA analysis

The thermogravimetric curves of undoped, Fe-doped, Cu-doped and (Fe-Cu) codoped TiO_2 samples calcined at 450 ^oC are shown in Fig. 5.4 (a). The weight loss between 30 – 200 ^oC is due to the desorption of physisorbed water and the degradation of organic chemicals [22]. The weight loss between 200 – 400 ^oC is attributed to the degradation of organic chemicals [22]. The weight loss between 400 - 600 ^oC is negligibe. The total weight loss in To, T2Fe, T3Cu, T4FeCu, T5FeCu and T6FeCu samples is 4.44 %, 2.85 %, 2.18 %, 2.92 %, 2.80 % and 2.74 %, respectively. Undoped sample (To) has maximum weigt loss. The introduction of dopants Fe, Cu or (Fe-Cu) co dopants increases the thermal stability of the systems.

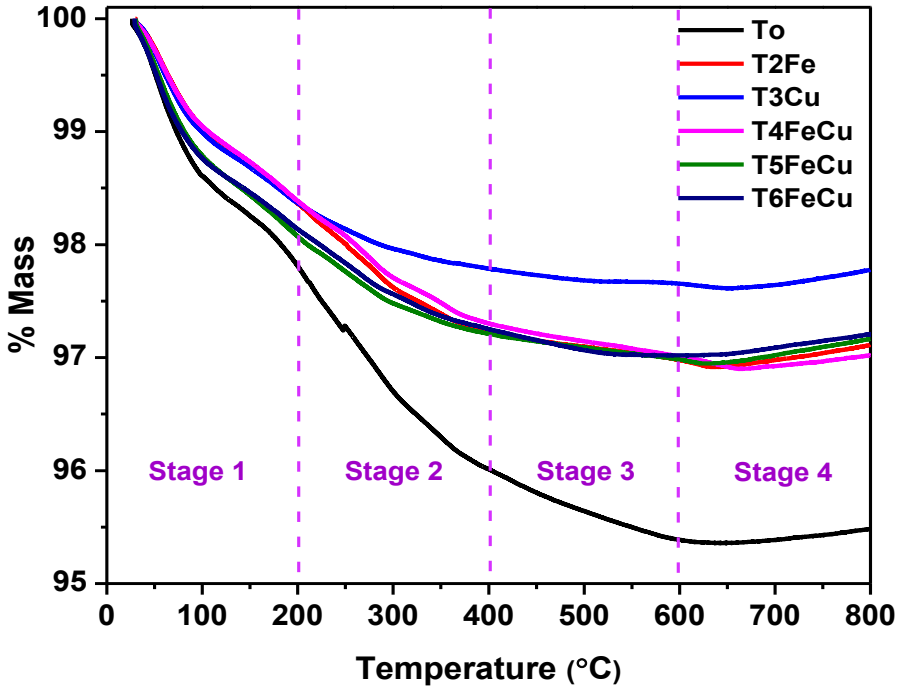

Figure 5.4 (a): Thermograms of undoped, Fe-doped, Cu-doped and (Fe, Cu) codoped TiO_2 samples calcined at 450 ^oC.

The kinetic parameters i.e. activation energy, pre-exponential factor and reaction mechanism are also determined using equation 4.7. The slope of the linear fitted curve between $ln\left(\frac{g(\alpha)}{T^2}\right)$ and

$\frac{1000}{T}$ gives the value of activation enegy (E_a) and the pre-exponential factor (A) is calculated from the intercept. In order to identify appropriate $g(\alpha)$, various reaction mechansim have already been given in Table 4.5 (Chapter 4). Fig. 5.4 (b) – 5.4 (g) shows the linear fitted curves corresponding to various reaction mechanism for all the samples. The reaction mechanism followed, activation energy and pre-exponential factor of samples are given in table 5.3.

Table 5.3: The value of activation energy and pre-exponential factor of all the samples.

Sample Id	Reaction mechanism	Activation Energy (kJ mol^{-1})	Pre-exponential factor (min^{-1})
T0	D3	18.94	8.15×10^{-7}
T2Fe	D3	20.77	1.54×10^{-6}
T3Cu	F3	18.98	2.4×10^{-4}
T4FeCu	D3	19.94	1.24×10^{-6}
T5FeCu	F3	16.74	1.2×10^{-4}
T6FeCu	D3	19.01	1.61×10^{-6}

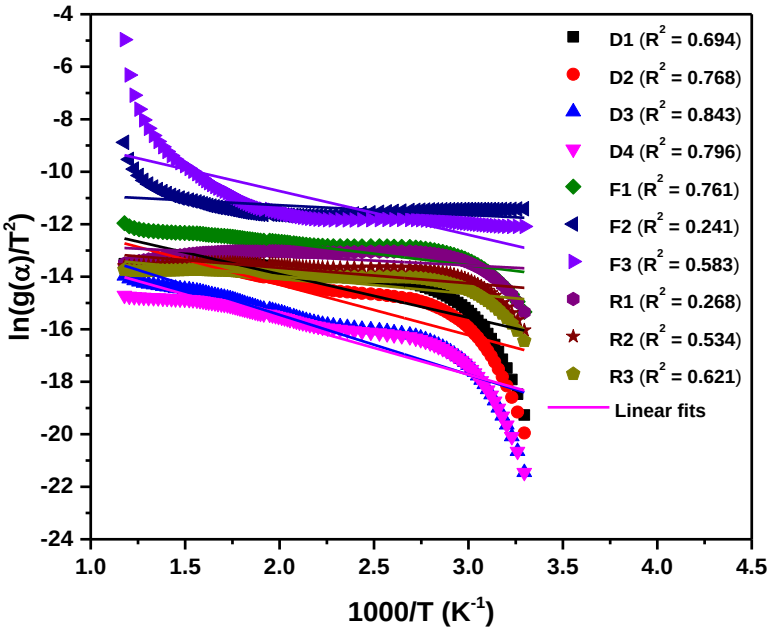

Figure 5.4 (b): Best linear fitted curves corresponding to various reaction mechanism for To sample.

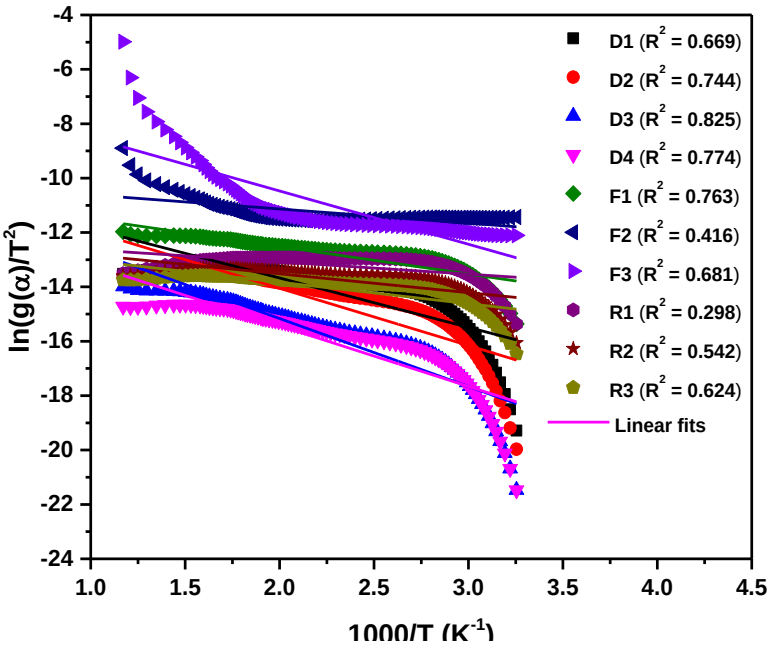

Figure 5.4 (c): Best linear fitted curves corresponding to various reaction mechanism for T2Fe sample.

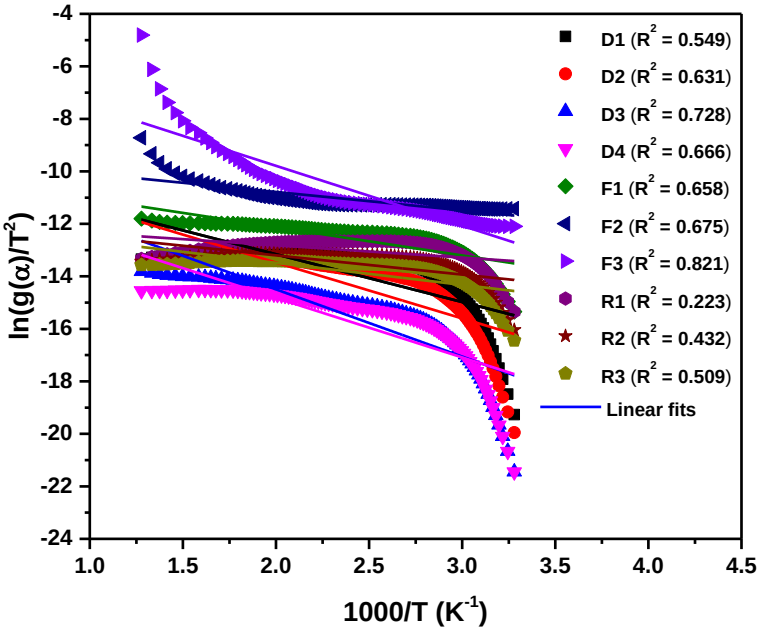

Figure 5.4 (d): Best linear fitted curves corresponding to various reaction mechanism for T3Cu sample.

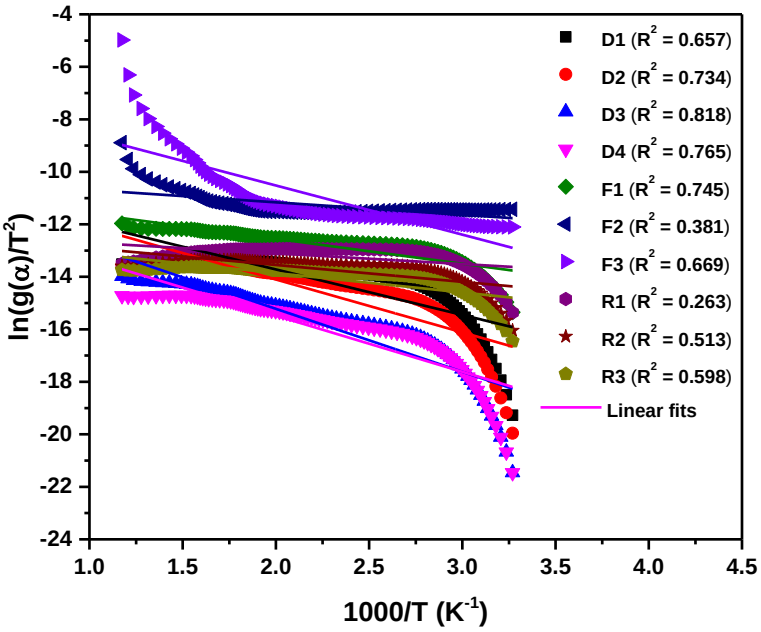

Figure 5.4 (e): Best linear fitted curves corresponding to various reaction mechanism for T4FeCu sample.

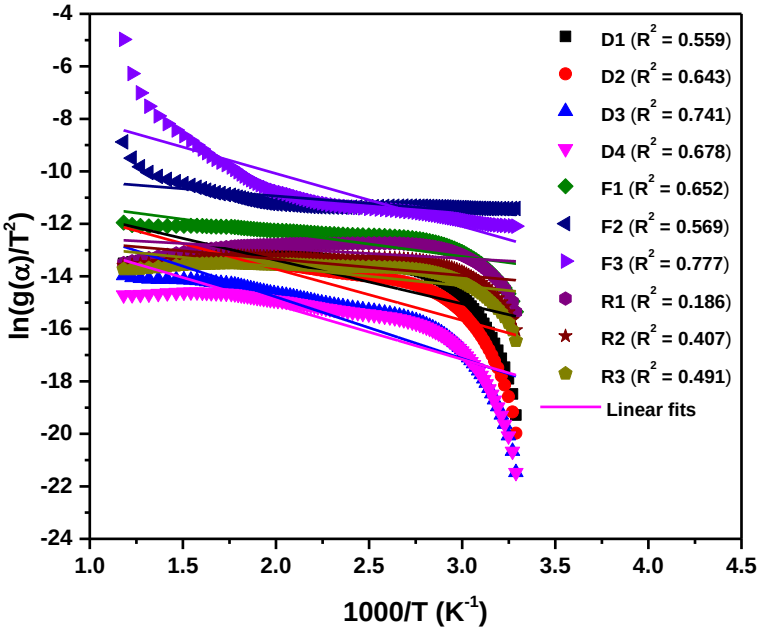

Figure 5.4 (f): Best linear fitted curves corresponding to various reaction mechanism for T5FeCu sample.

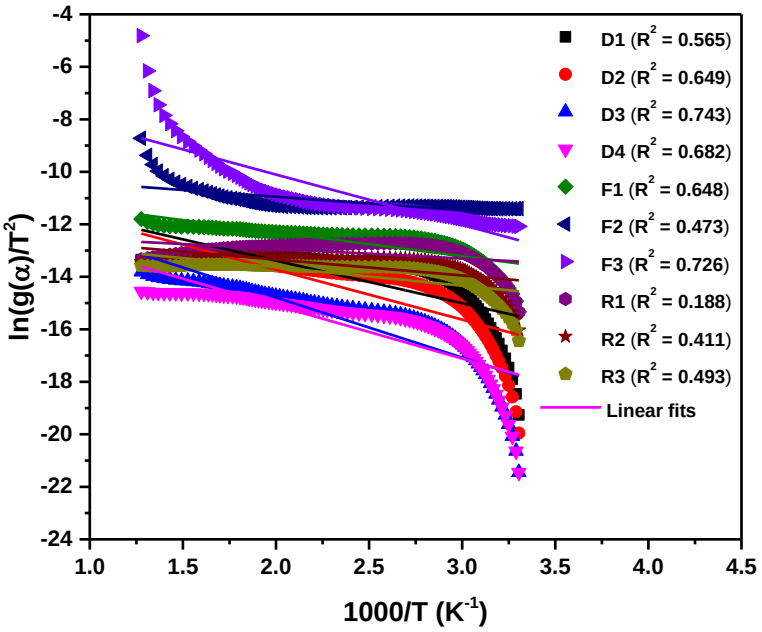

Figure 5.4 (g): Best linear fitted curves corresponding to various reaction mechanism for T6FeCu sample.

5.1.5 HRTEM analysis

TEM and HRTEM images of undoped, Fe-doped, Cu-doped and (Fe, Cu) codoped TiO_2 samples are shown in Fig. 5.5 (a) and 5.5 (b). It is clear from Fig. 5.5 (a) that aggregates of nanoparticles have formed due to the very high surface free energy of small nanoparticles. In Fig. 5.5 (b), lattice arrays of samples show interplanar distance corresponding to the (101) plane of anatase phase. Selected area electron diffraction (SAED) pattern supports the nanocrystallinity of synthesized samples as shown in Fig. 5.5 (c). Due to high agglomeration of nanoparticles, the particle size distribution calculations are done using *AxioVision Rel.4.9.1.0* [23] to find the mean particle size. The mean particle size of To, T2Fe, T3Cu and T5FeCu samples is found to be 11.71, 11.08, 10.51 and 9.95 nm, respectively. The results are in close agreement well with the XRD results. The plot of frequency of particles againt logrithmic particle size is given in Fig. 5.5 (d). The size of nanoparticles follows the logrithmic distribtution function given in equation 4.8.

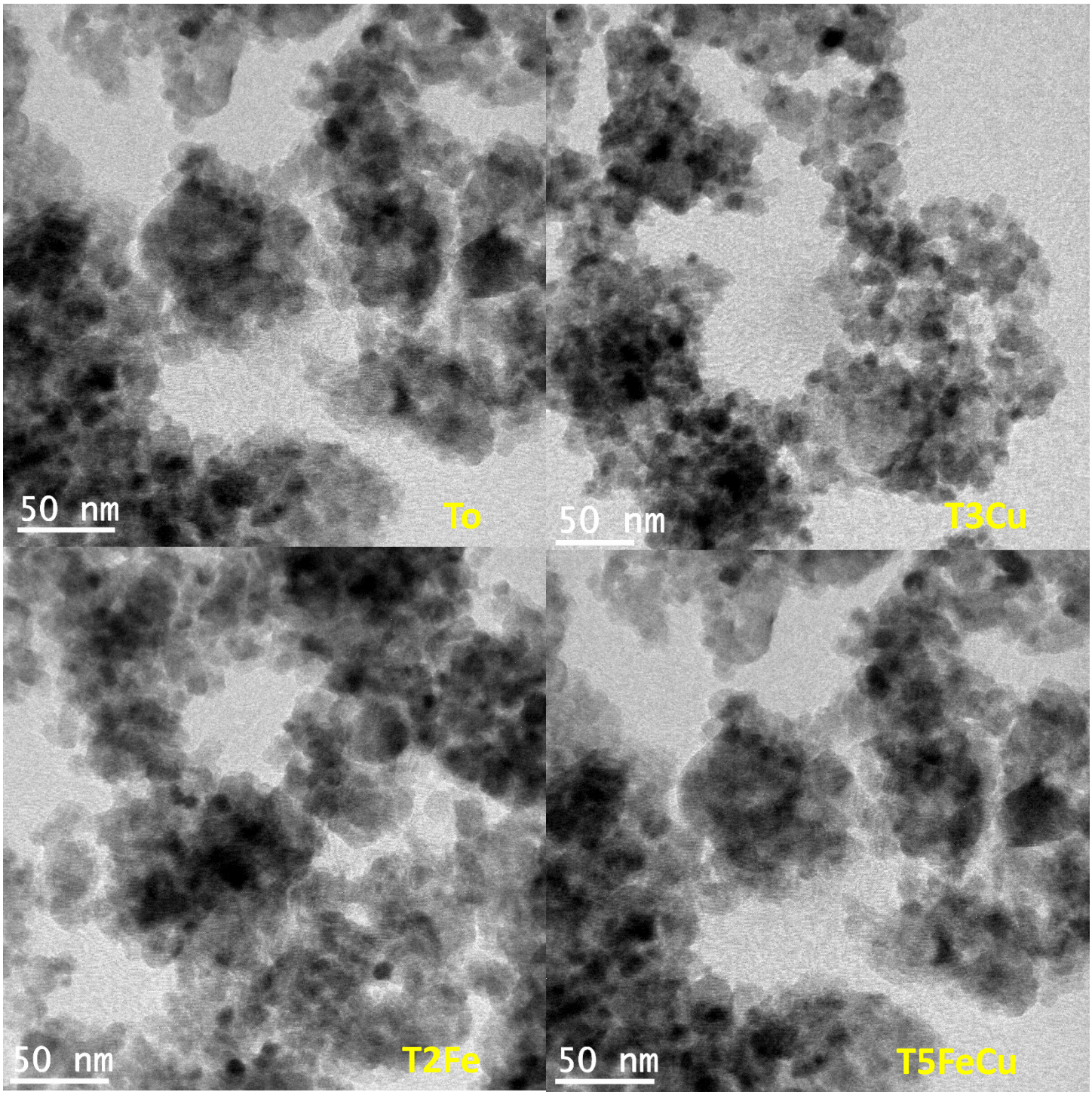

Figure 5.5 (a): TEM micrographs of undoped, Fe-doped, Cu-doped and (Fe, Cu) codoped TiO_2 samples calcined at 450 ^{o}C.

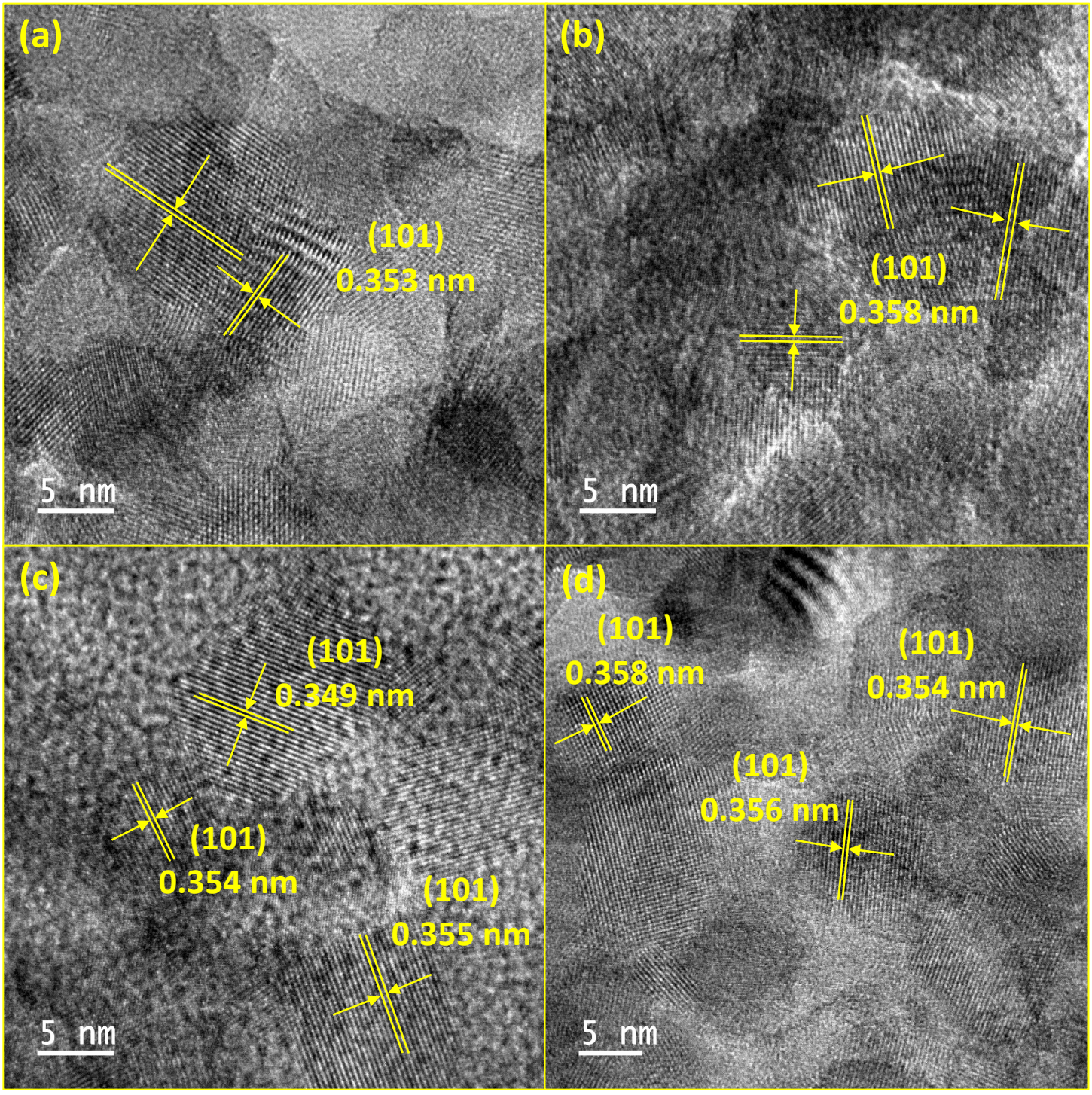

Figure 5.5 (b): HRTEM micrographs of (a) undoped, (b) Cu-doped, (c) Fe-doped and (d) (Fe-Cu) codoped TiO_2 samples calcined at 450 ^oC.

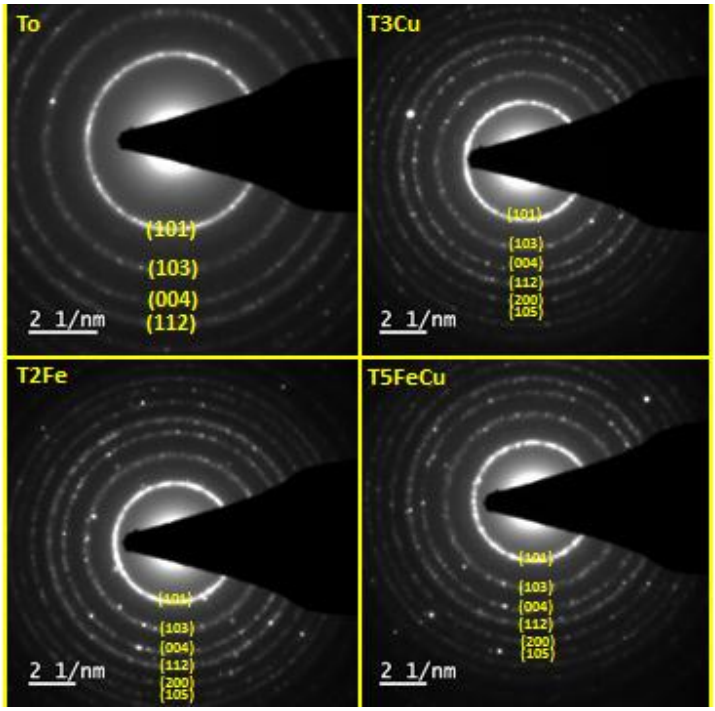

Figure 5.5 (c): Selected area diffraction patterns of undoped, Fe-doped, Cu-doped and (Fe, Cu) codoped TiO_2 samples calcined at 450 ^oC.

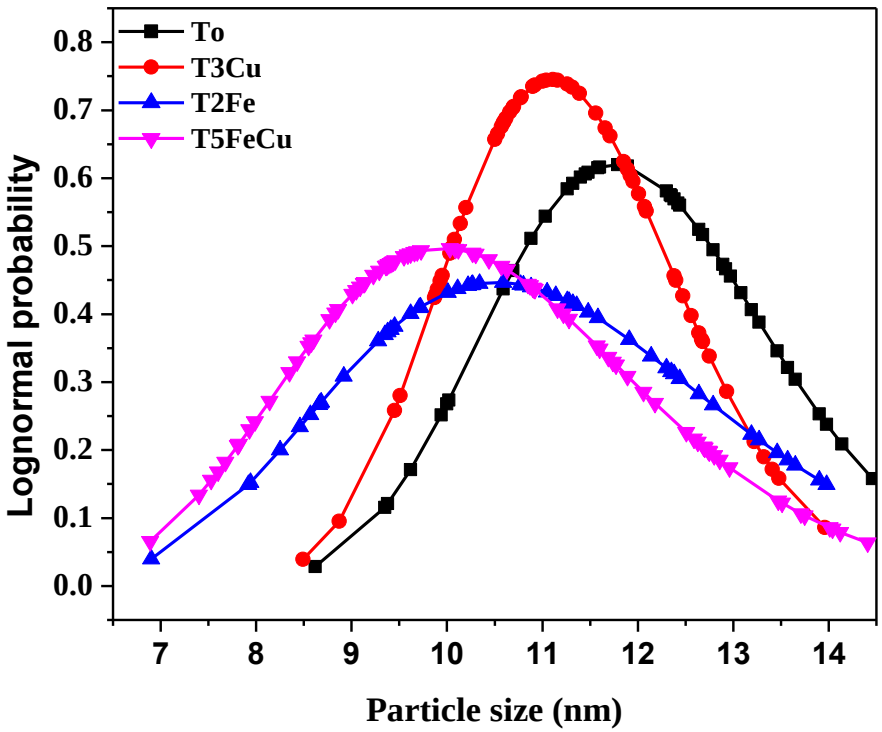

Figure 5.5 (d): Lognormal distribution of nanoparticle's size of undoped, Fe-doped, Cu-doped and (Fe, Cu) codoped TiO_2 samples calcined at 450 ^oC.

5.1.6 PL analysis

Room temperature PL spectra of samples recorded at an excitation wavelength of 400 nm are given in Fig. 5.6. The peak observed around 465 nm is due to excitonic PL, indicates the presence of surface oxygen vacancies and defects in the TiO_2 samples [16]. As compared to the undoped TiO_2 (To), doped samples show decrease in PL intensity which indicates that dopants inhibit the recombination of photo electron hole pairs [16]. It owes to the transfer of the electrons from the conduction band to the new levels introduced by metal dopants. T5FeCu shows a maximum decrease in intensity.

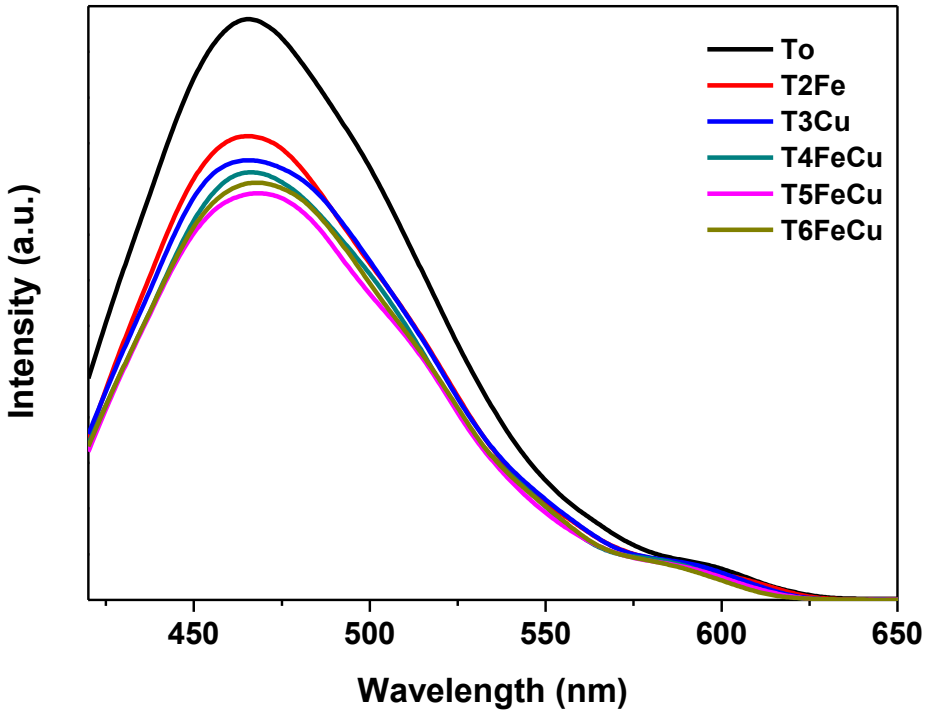

Figure 5.6: Room temperature photoluminescence spectra of undoped, Fe-doped, Cu-doped and (Fe, Cu) codoped TiO_2 samples calcined at 450 ^oC.

5.1.7 Photocatalytic degradation of diethyl phthalate

The influence of doping on intrinsic TiO_2 photocatalytic activity is studied using photocatalytic degradation of diethyl phthalate. The structure and the stability of diethyl phthalate have been

discussed in chapter 4 (Section 4.1.8). The kinetic studies of degradation of diethyl phthalate in presence of To, T2Fe, T3Cu, T4FeCu, T5FeCu and T6FeCu samples and UV-vis light source, are given in Fig. 5.7 (a). The resultant linear curves indicate that degradation of diethyl phthalate with each photocatalyst follow pseudo first order kinetic model, $-\ln\frac{C}{C_o} = k_{1app}t$, where C is concentration of diethyl phthalate at time t, C_o is the initial concentration, k_{1app} is the apparent first-order rate constant (min^{-1}) [16]. The rate constants derived from –ln C/C_o versus t plots are given in table 5.3. The rate constants for photocatalytic reaction using To, T2Fe, T3Cu, T4FeCu, T5FeCu and T6FeCu are found to be $8.5x10^{-3}$, $1.2x10^{-2}$, $1.6x10^{-2}$, $2.1x10^{-2}$, $3.4x10^{-2}$ and $2.7x10^{-2}$, respectively. The maximum rate constant for T5FeCu sample reveals about its highest photocatalytic activity as compared to other samples. The use of Fe doped, Cu doped, (Fe, Cu) codoped TiO_2 samples for the photocatalytic degradation of organic pollutants has been reported in literature [3, 24, 25]. The first order apparent rate constant for Rhodamine B dye degradation using Fe doped TiO_2 [3] and reactive blue dye degradation using Cu doped TiO_2 [24] has been reported to be $3.0x10^{-2}$ and $3.6x10^{-2}$ min^{-1}, respectively.

Fig. 5.7(b) shows the linear plots of pseudo second order model for the degradation of diethyl phthalate in presence of photocatalysts and UV-vis light. The kinetics of pseudo second order photocatalytic degradation of diethyl phthalate is determined by using equation 4.10. The fitting of experimental data to the pseudo second order model is not so ideal with low correlation coefficient. The apparent constant (k_{2app}) is calculated from slope of *1/C* versus irradiation time. The apparent rate constants and correlation coefficients for pseudo first order and second order are given in Table 5.4.

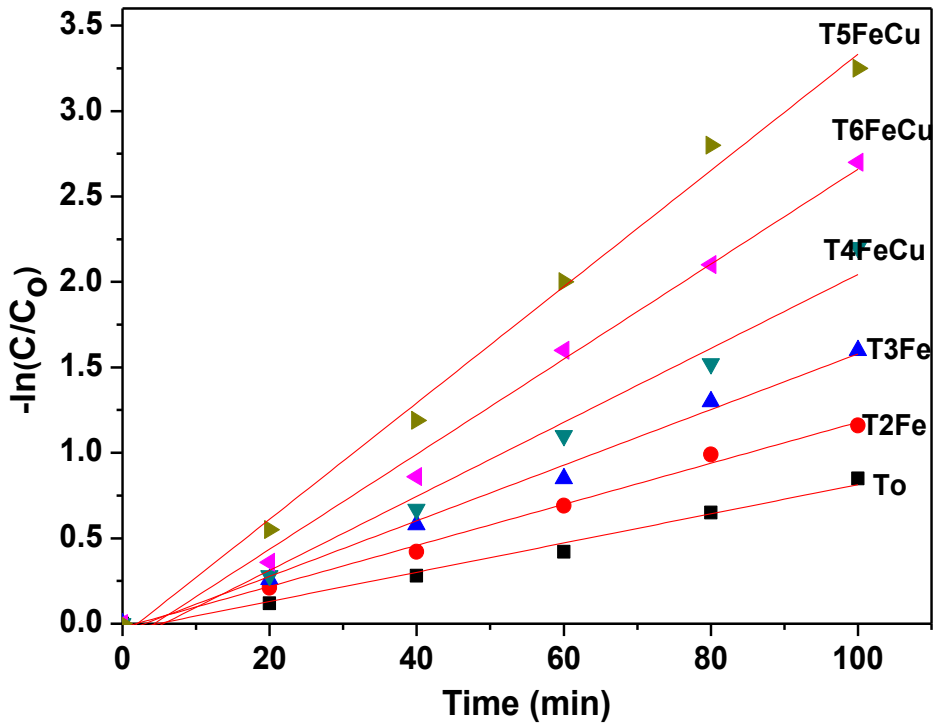

Figure 5.7 (a): Linear plots of pseudo first order when C_o = 30 ppm, catalyst load = 1g/l.

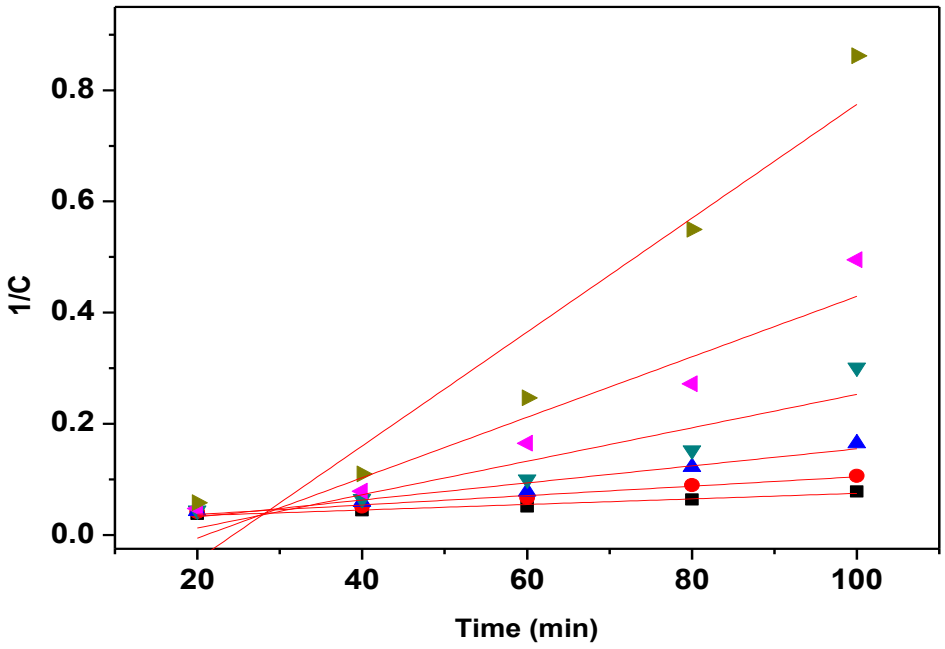

Figure 5.7 (b): Linear plots of pseudo second order when C_o = 30 ppm, catalyst load = 1g/l.

Table 5.4: The value of apparent rate constants for pseudo first order and pseudo second order model.

Sample Id	Apparent reaction rate constant, k_{1app} (min^{-1}) (Pseudo first order)	R^2 (Pseudo first order)	Apparent reaction rate constant, k_{2app} (min^{-1}) (Pseudo second order)	R^2 (Pseudo second order)
To	$8.5x10^{-3}$	0.9927	$5x10^{-4}$	0.9554
T2Fe	$1.2x10^{-2}$	0.9951	$8.4x10^{-4}$	0.9758
T3Cu	$1.6x10^{-2}$	0.9987	$1.5x10^{-3}$	0.9350
T4FeCu	$2.1x10^{-2}$	0.9959	$3.0x10^{-3}$	0.8082
T5FeCu	$3.4x10^{-2}$	0.9950	$1.0x10^{-2}$	0.874
T6FeCu	$2.7x10^{-2}$	0.9941	$5.4x10^{-3}$	0.8968

T5FeCu sample has an optimum dopant concentration of 0.075 % Fe and 0.075 % Cu, where the dopants act as trapping sites. T6FeCu sample, having higher dopant concentration than T5FeCu, dopants may act as recombination centers. Beyond the optimum dopant concentration, the rate of recombination starts dominating according to following equation:

$$K_{RR} = \exp(\frac{-2R}{a_o}) \quad (5.4)$$

where K_{RR} is the rate of recombination, R is the distance separating electron hole-pairs, a_o is the hydrogenic radius of wavefunction for the charge carrier [13]. As a consequence, the recombination rate increases exponentially with the dopant concentration because the average distance between the trap sites decreases with increasing number of dopant ions confined within a domain [13].

From Table 5.5, it is clear that the rate of reaction increases with decreasing particle size. However, the activation energy does not follow any trend corresponding to rate of reaction.

Table 5.5: The value of activation energy, apparent rate constant and particle size for all samples.

Photocatalysts	Particle size (nm)	Activation Energy (kJ mol^{-1})	Apparent reaction rate constant, k_{1app} (min^{-1}) (Pseudo first order)
To	11.71	18.94	$8.5x10^{-3}$
T2Fe	11.08	20.77	$1.2x10^{-2}$
T3Cu	10.51	18.98	$1.6x10^{-2}$
T4FeCu	Not done	19.94	$2.1x10^{-2}$
T5FeCu	9.95	16.74	$3.4x10^{-2}$
T6FeCu	Not done	19.01	$2.7x10^{-2}$

Fig. 5.7 (c) shows the UV-vis spectral change of diethyl phthalate during irridation in presence of T5FeCu sample. In UV-vis spectrum of diethyl phthalate, two intense bands at wavelengths of 229 nm and 276 nm have been obtained. The decrease of absorption peak of diethyl phthalate at λ_{max}= 229 nm indicates the degradation of diethyl phthalate during photo degradation.

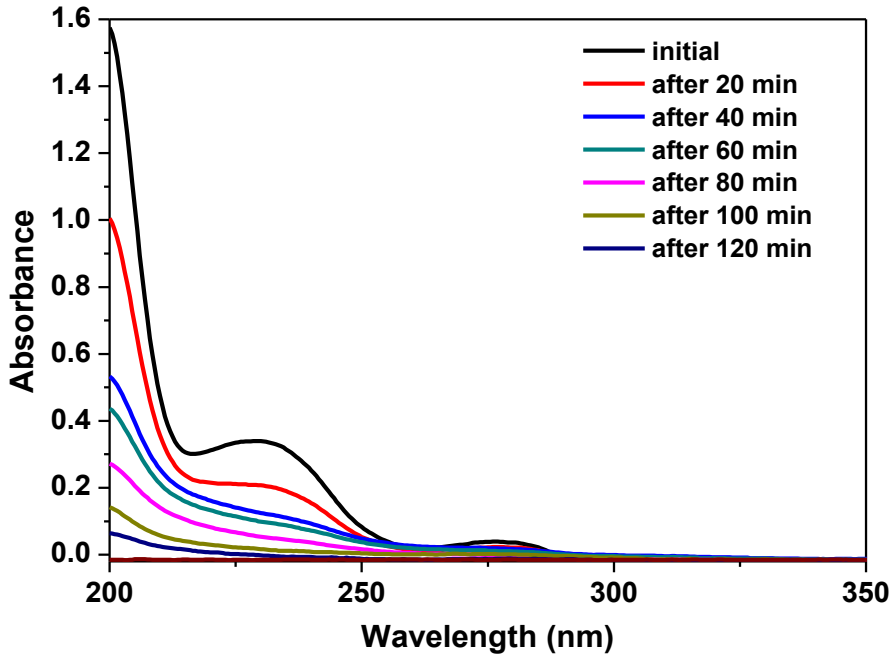

Figure 5.7 (c): UV-vis absorption spectra of diethyl phthalate in presence of T5FeCu sample during light irradiation.

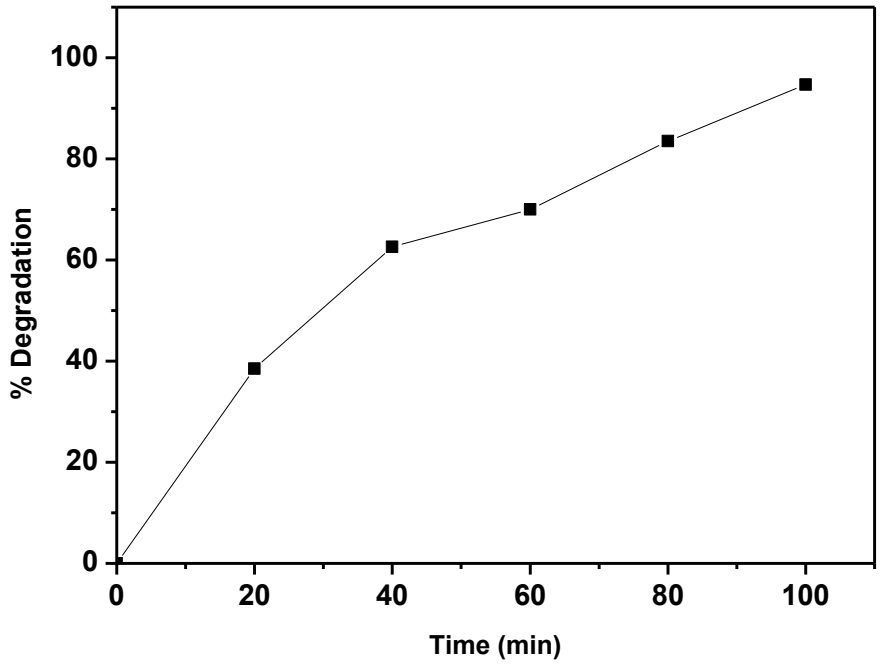

Figure 5.7 (d): Change in % degradation of diethyl phthalate as a function of irradiation time.

The percentage of degradation of diethyl phthalate is determined by using equation 4.11. Plot of % degradation and time is given Fig. 5.7 (d). The percentage degradation of diethyl phthalate is 95 % in 120 min.

5.1.8 Conclusions

Undoped, Fe-doped, Cu-doped and (Fe, Cu) codoped TiO_2 nanoparticles are prepared via sol-gel method and their photocatalytic activity is evaluated. The XRD peaks shift towards lower diffraction angle with dopants which leads to larger unit cell of anatase phase. The rate of reaction increases with decreasing particle size. (0.075 mol % Fe, 0.075 mol % Cu) codoped TiO_2 sample shows higher photocatalytic activity than pure or single doped TiO_2. The enhancement in photocatalytic activity upon codoping can be attributed to the higher disordering

created by the lower valence metal ions doping and increased absorption as well as the efficient transfer of electron-hole pairs through co-dopant ions in the sub energy bands of TiO_2.

References

1. L. Agartan, D. Kausuz, J. Park, A. Ozturk Ceram Int 41 (2015) 12788.
2. S. Sood, A. Umar, S.K. Mehta, S.K. Kansal, J Colloid Interface Sci 450 (2015) 213.
3. N.R. Mathews, M.A. Cortes Jacome, C. Angeles-Chavez, J.A. Toledo Antonio, J Mater Sci: Mater Electron 26 (2014) 5574.
4. A. Zaleska, Recent Patents on Engineering 2 (2008) 157.
5. B. Liu, H.M. Chen, C. Liu, S. C. Andrews, C. Hahn, P. Yang, J Am Chem Soc 135 (2013) 9995.
6. T. Sun, J. Fan, E. Liu, L. Liu, Y. Wang, H. Dai, Y. Yang, W. Hou, X. Hu, Z. Jiang, Powder Technol 228 (2012) 210.
7. Z. Yuan, J. Jia, L. Zhang, Mater Chem Phys 73 (2002) 323.
8. P. Benjwal, K. K. Kar, RSC Adv 5 (2015) 98166.
9. L.G. Devi, B.N. Murthy, S.G. Kumar, Mater Sci Eng B 6 (166) 2010.
10. S.Yu, H.J. Yun, D.M. Lee, J.Yi, J Mater Chem 22 (2012) 12629.
11. B.D. Cullity, S.R. Stock (2001) Elements of X-ray Diffraction, 3rd edn Addision wesley-Publishing compony, Massachusetts.
12. L.G. Devi, N. Kottam, B.N. Murthy, S.G. Kumar, J Mol Catal A: Chem 328 (2010) 44.
13. L.G. Devi, N. Kottam, S.G. Kumar, K.S. Anantha Raju, Catal Lett 131 (2009) 612.
14. S. Singh, K. Singh, J Non Cryst Solids 386 (2014) 100.
15. R. Lopez, R. Gomez, J Sol-Gel Technol 61 (2012) 1.

16. H.M. Yadav, S.V. Otari, V.B. Koli, S.S. Mali, C.K. Hong, S.H. Pawar, S.D. Delekar, J Photochem Photobiol A Chem 280 (2014) 232.
17. K. Apiwong-ngram, P. Pongwan, S. Phanichphant, K. Wetchakun, N. Wetchakun, Powder Technol 266 (2014) 447.
18. L.S. Yoong, F.K. Chong, B.K. Dutta, Energy (2009) 1652.
19. M.R. Derrick, D. Stulik, J.M. Landry, Infrared spectroscopy in conservation Science, The Getty conservation institute, Los Angles (1999).
20. L. Kumaresan, A. Prabhu, M. Palanichamy, E. Arumugam, V. Murugesan, J Hazard Mater 186 (2011) 1183.
21. B. Babiarczuk, A. Szczurek, A.D. Sikorska, I. Rutkowska, J. Krzak, Surf Coat Technol 285 (2016) 134.
22. M.M. Ba-Abbad, A.A.H. Kadhum, A.B. Mohamad, M.S. Takriff, K. Sopian, Int J Electrochem Sci **7** (2012) 4871.
23. A. Gupta, G. Singla, O.P. Pandey, Ceram Int 42 (2016)13024.
24. P Dharmarajan, A. Sabastiyan, S. Titus, C. Muthukumar, Chem Sci trans 2 (2013) 1450.
25. J. Liu, Z. Zhang, L. Yang, S. Deng, International J Chem 3 (2011) 87.

Chapter 6
Results and discussion
Study of photocatalytic degradation of diethyl phthalate using Ni doped TiO_2 nanoparticles

Overview

The present chapter deals with the study of undoped and Ni doped TiO_2 nanoparticles synthesized by the sol-gel technique. The samples are characterized using X-ray diffraction (XRD), UV-Vis diffuse reflectance spectroscopy (DRS), Fourier transform infrared spectroscopy (FTIR), Thermogravimetric analysis (TGA), Transmission electron microscopy (TEM) and photoluminescence (PL) techniques. The as prepared samples are used for the photocatalytic degradation of diethyl phthalate.

6.1 Introduction

High rate of electron-hole recombination and wide optical band gap of TiO_2 makes it unusable for photocatalytic applications on commercial level [1]. Doping of TiO_2 with transition metal ions is an effective and simple approach to modify the photocatalytic properties of TiO_2. Among various transition metals, Ni^{2+} has been found to be an efficient dopant for improving photocatalytic activity of TiO_2. Ni^{2+} can form octahedral coordination as Ti^{4+} [2]. Also, it traps the charge carriers and prevents the recombination of photogenerated electron-hole pairs. The ionic radius of Ni^{2+} (0.68 Å) is close to that of Ti^{4+} (0.60 Å). Ni^{2+} can be conveniently integrated into TiO_2 lattice matrix. Tseng et al. [3] studied the enhanced photocatalytic degradation of xylene vapors using Ni doped TiO_2 photocatalysts as compared to bare TiO_2. Ganesh et al. [4] found the improved photocatalytic activity of TiO_2 for the degradation of methylene blue dye by doping Ni into TiO_2. Parveen et al. [5] found that the degradation of Rose Bengal dye was significantly enhanced using Ni doped TiO_2 as compared to undoped TiO_2. The present work focuses on the synthesis of undoped and Ni doped TiO_2 nanoparticles by the sol-gel method. The synthesized powders are further used to degrade diethyl phthalate through photocatalytic degradation technique. The undoped, 0.2 mol % Ni-TiO_2, 0.4 mol % Ni-TiO_2, 0.6 mol % Ni-TiO_2, 0.8 mol % Ni-TiO_2 and 1.0 mol % Ni-TiO_2 samples have been labeled as T0N, T2N, T4N, T6N, T8N and T10N, respectively. The characterizations are done for T0N, T2N, T4N and T6N samples because high doping in T8N and T10N samples decreases the photocatalytic degradation (discussed in section 6.1.7).

6.1.1 XRD analysis

X-ray diffraction patterns of undoped and Ni doped TiO_2 nanoparticles calcined at 450 ^oC are given in Fig. 6.1. The XRD patterns of the samples show the presence of two phases, namely

anatase [ICDD No. 01-089-4921] and rutile [ICDD No. 01-083-2242]. The diffraction peaks at 2θ = 25.36°, 36.9°, 37.8°, 38.5°, 48.0°, 53.8°, 55.0°, 62.7°, 70.3° and 75.1° are attributed to the (101), (103), (004), (112), (200), (105), (211), (204), (220) and (215) planes of anatase phase respectively. The diffraction peaks at 2θ = 27.4°, 36.0°, 39.1°, 41.2°, 44.0°, 54.3°, 56.6°, 64.0° and 69.2° are attributed to the (110), (101), (200), (111), (210), (211), (220), (310) and (301) planes of rutile phase of TiO_2, respectively**.** The XRD peaks at 2θ = 25.36° (101) and 2θ = 27.4° (110) are the characteristic peaks of anatase and rutile phase, respectively. No characteristic peak corresponding to Ni has been observed, which may be due to the formation of solid solution between Ni and TiO_2 [6]. The volume fraction of anatase phase increases with doping as given in table 6.1. From Fig. 6.1, it is clear that intensity of all the peaks corresponding to the rutile in doped TiO_2 samples decreases with increasing amount of dopant, which indicates the inhibition of rutile phase due to doping of nickel.

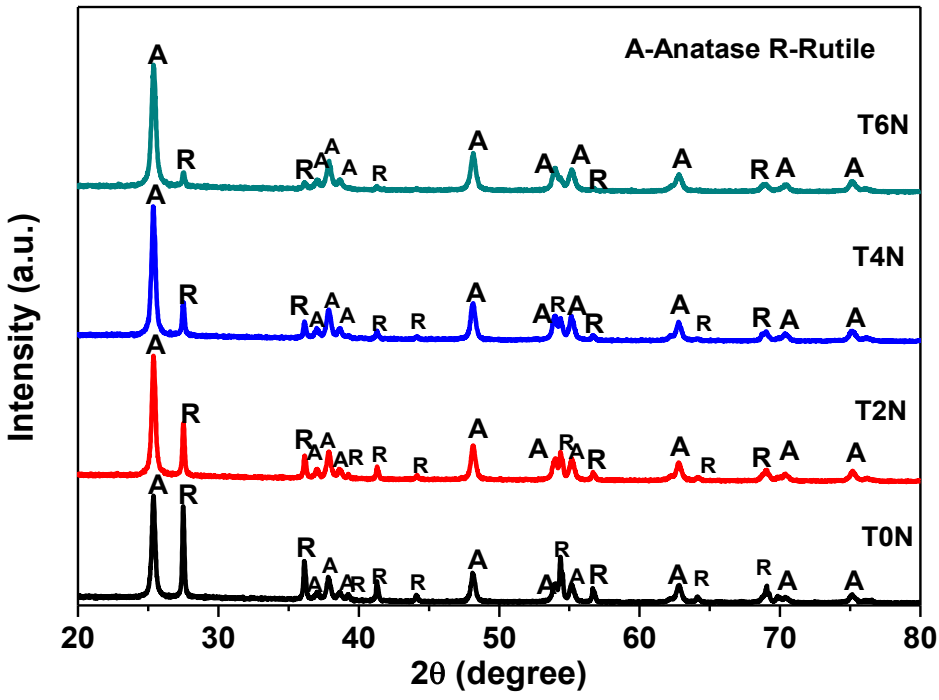

Figure 6.1: XRD patterns of undoped and Ni doped TiO_2 nanoparticles calcined at 450 °C.

Table 6.1 Volume fraction of anatase and rutile phase calculated from XRD data.

Sample Code	Volume fraction of anatase phase (%)	Volume fraction of rutile phase (%)
T0N	67.2	32.8
T2N	79.5	20.5
T4N	86.4	13.6
T6N	95.2	4.8

Same dopant in subsitutional form may increase the oxygen vacancy level and thereafter promote the phase transformation, whereas in the interstitial form, it may enhance higher lattice constraint as compared to subsitutional form and hence inhibit the phase transformation. This concept usually applies to all the dopants, although the transition metal ions like Mn, Fe, Ni with variable valency mostly show mixed effects [7].

Table 6.2: The structural parameters calculated from the XRD data corresponding to the characteristic peak (101) of anatase phase.

Sample	2θ (degree)	FWHM (degree)	d-spacing (Å)	Crystallite size (nm)	Lattice parameters (Å)	Unit cell volume ($Å^3$)
T0N	25.37	0.2755	3.506	29	$a = b = 3.76$ $c = 9.712$	137.30
T2N	25.38	0.2883	3.506	28	$a = b = 3.76$ $c = 9.712$	137.30
T4N	25.37	0.2912	3.507	27	$a = b = 3.76$ $c = 9.712$	137.30
T6N	25.39	0.3352	3.504	24	$a = b = 3.76$ $c = 9.667$	136.66

As phase transformation is getting inhibited in the present case, Ni is expected to occupy interstitial site in the synthesized samples. Generally, the presence of interstitial ions as well as the reduction of interparticle contact (grain boundary phases) in anatase phase inhibits the transformation [7]. The crystallite size is estimated using Debye Scherrer formula [8] as given in equation 4.3. The crystallite size of T0N, T2N, T4N and T6N samples is obtained to be approximately 29, 28, 27 and 24 nm, respectively. Moreover, the crystallite size decreases with the increase in dopant concentration, which can be attributed to the peak broadening due to defects created by dopant in doped samples. Lattice parameters of the samples (given in Table 6.2) are calculated using equation 4.2. The lattice parameters are calculated using diffraction peaks corresponding to the (101) and (200) planes of anatase phase.

6.1.2 UV-vis absorption analysis

Fig. 6.2 (a) shows the diffuse absorbance spectra of undoped and Ni doped TiO_2 nanoparticles measured in the UV-vis region. It clearly indicates that the doped samples show remarkable absorbance in the region of 400-550 nm, demonstrating their strong visible light absorbance ability as compared to the undoped sample. The band gap of the samples is calculated using Kubelka Munk Function which is $f(R) = (1-R)^2/2R$, where R is the diffuse reflectance [9]. In the present case, $(f(R).hv)^{1/2}$ is plotted against photon energy hv (Fig. 6.2 (b)) and the linear portion of the curves is extrapolated to have an intercept on the x-axis. The value at x-axis where intercept cuts i.e. $(f(R).hv)^{1/2}= 0$ is taken as the value of the band gap. For the linear region of the plots, the following relationship must be satisfied:

$$[f(R).hv]^{1/2}=K(hv -E_g) \quad (2)$$

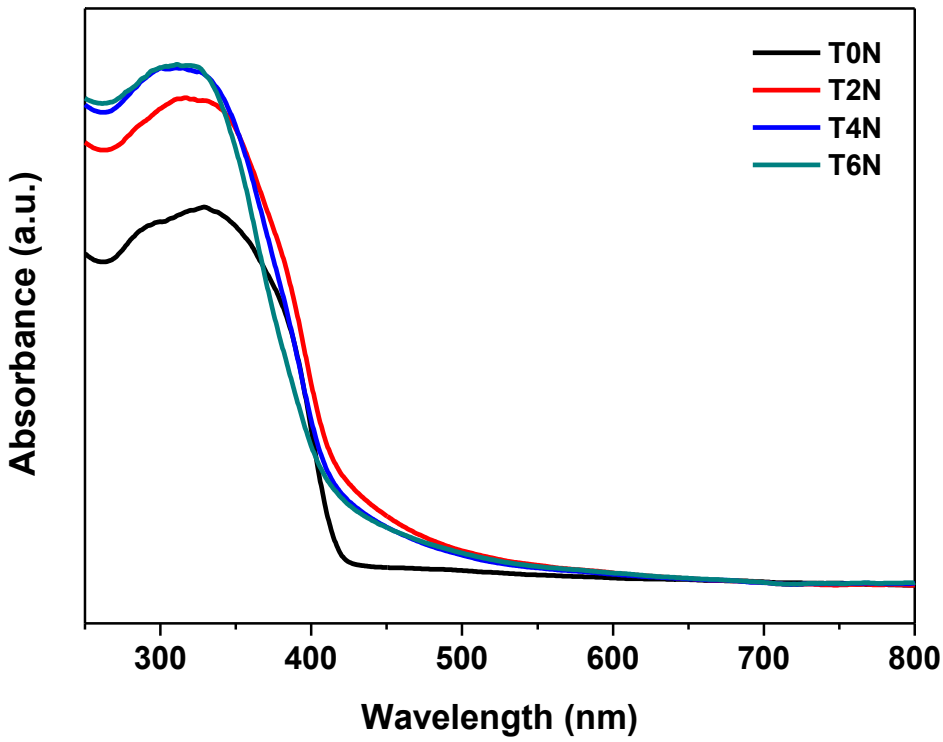

Figure 6.2 (a) UV-vis absorption spectra of undoped and Ni doped TiO_2 nanoparticles calcined at 450 ^{o}C.

where E_g is band gap energy and K is a characteristic constant for every semiconductor material [9]. The band gap of T0N, T2N T4N and T6N samples is obtained to be 2.94, 2.87, 2.97 and 3.07 eV, respectively. Ganesh et al. [4] reported the band gap of 0.5 atm % Ni doped TiO_2 to be 2.97 eV []. Our results agree well with work of Ganesh et al. [4]. Pure anatase has band gap of 3.2 eV whereas for rutile phase it is 3.0 eV. However, a mixture of these phases yields lower band gap corresponding to the visible region [10].

The red shift of 0.2 mol % Ni-TiO_2 samples can be attributed to the charge transfer transitions between impurity band and the TiO_2 conduction band [11]. In TiO_2, the valence band is composed of O-2p states and the conduction band is composed of Ti-3d states. The incorporation of Ni^{2+} into TiO_2 lattice host provides Schottky barriers, which facilitate the transfer and trapping

of electrons from TiO_2. Hence, the charge transfer between the Ni^{2+} ions d-electron and TiO_2 conduction will appear [11].

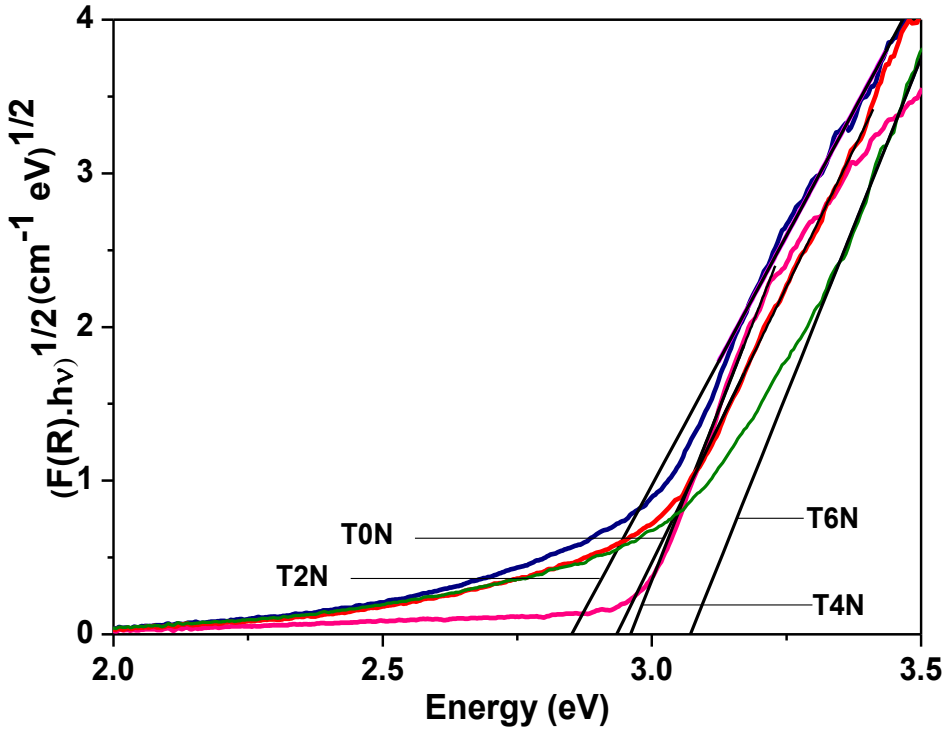

Figure 6.2 (b): Determination of band gap energy of samples using Kubelka-Munk function.

Urbach energy, before and after introduction of the dopant, can give fair idea about the modification of the band structure of TiO_2. Urbach energy gives a measure of structural disorder in a material and is given by the tail region where absorption α (ν) depends exponentially on the photon energy hν (Equation 4.6). Urbach energy, E_u is calculated by plotting lnf(R) versus hν. The reciprocal of the slopes of the linear portion gives the value of E_u. The Urbach energy of T0N, T2N, T4N and T6N samples is 0.038, 0.098, 0.098, 0.150 eV, respectively. Higher Urbach energy in doped samples depicts more disorder in them as compared to the undoped sample. Many factors like dislocations, electric field of defects and thermal vibrations etc. can cause the tailing of energy states in the forbidden gap. According to Dow and Redfield, Urbach energy is

attributed to the random internal electric field associated with the structural disorder, which broadens the excitons line [12, 13].

6.1.3 FTIR analysis

The FTIR patterns of undoped and Ni doped TiO_2 nanoparticles calcined at 450 ^oC are shown in Fig. 6.3. In all the samples, the group frequency region of 4000-1300 cm^{-1} has bands around 3421 and 1639 cm^{-1} which are attributed to the stretching vibrations of O-H groups and bending vibrations of adsorbed water molecules, respectively [14]. Moreover, occurrence of bands between 1300-1500 cm^{-1} and 2800-3000 cm^{-1} indicate the presence of small amount of organic material in the sample [15]. In present case, the band around 595 cm^{-1} is due to the stretching vibrations of Ti-O-Ti and Ti-O bonds [16]. It is clear that the band has different shape in case of doped sample as compared to undoped sample due to doping. Moreover, the band is shifting towards lower wavenumber in case of doped samples. This indicates the weakening of bonds.

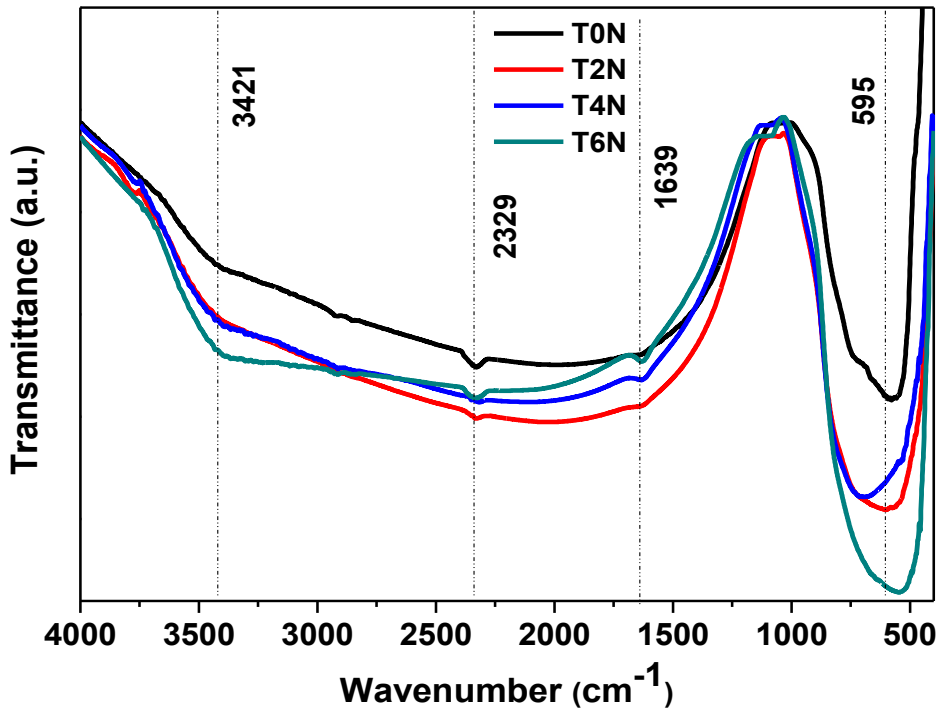

Figure 6.3: FTIR patterns of undoped and Ni doped TiO_2 nanoparticles calcined at 450 ^oC.

With the introduction of dopant, the structural rearrangements can take place in Ti-O-Ti environment leading to strained network and distortion of local symmetry. The band is more intense in case of doped samples as compared to undoped because of presence of more molecules in doped samples. Our results agree well with the results obtained by Ganesh et al. [17].

6.1.4 TGA analysis

Thermogravimetric analysis is done in order to study the thermal stability of undoped TiO_2 as compared to nickel doped TiO_2. The thermogravimetric curves of undoped and Ni doped TiO_2 nanoparticles calcined at 450 ^oC are given in Fig. 6.4.

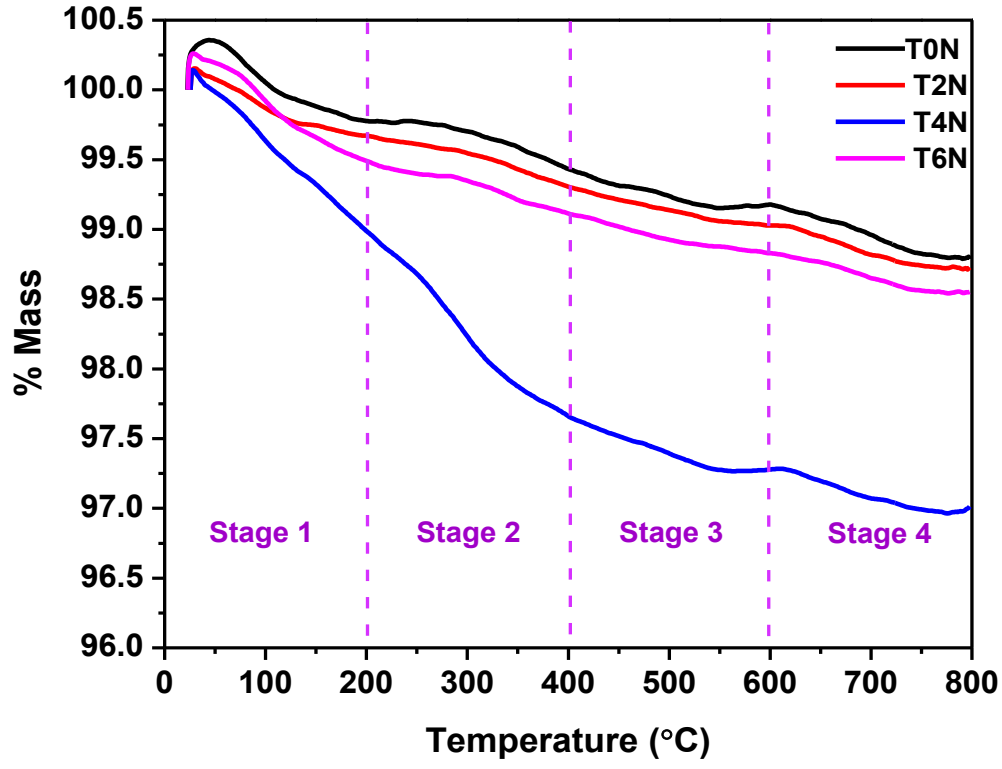

Figure 6.4 (a): Thermograms of undoped and Ni doped TiO_2 nanoparticles calcined at 450 ^oC.

The total weight loss in T0N, T2N, T4N and T6N samples is 1.19 %, 1.46 %, 3.00 % and 1.29 %, respectively. The weight loss is attributed to the evaporation of water, volatility of organic compounds and loss of OH groups [17]. The kinetic parameters i.e. activation energy, pre-exponential factor and reaction mechanism are also determined using equation 4.7. The slope of

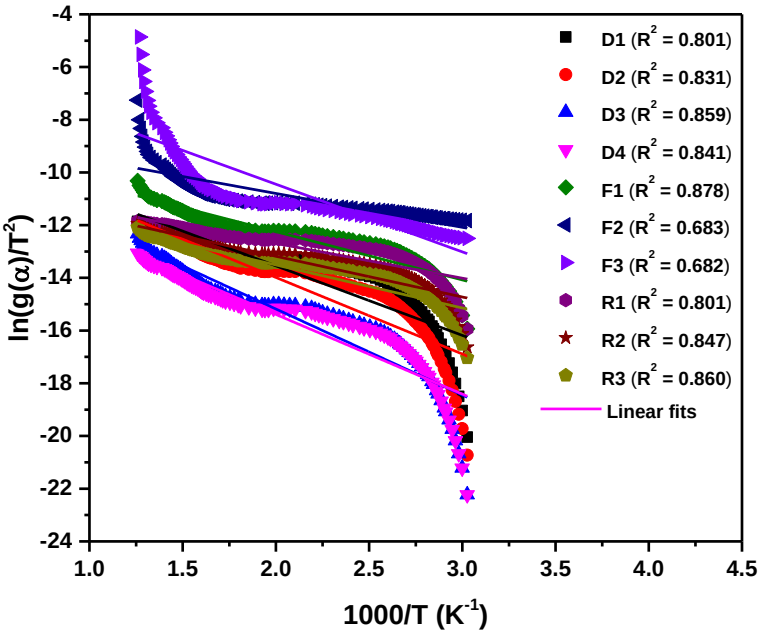

Figure 6.4 (b): Best linear fitted curves corresponding to various reaction mechanism for T0N sample.

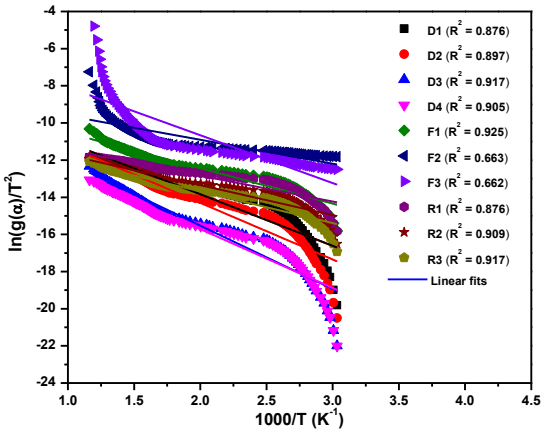

Figure 6.4 (c): Best linear fitted curves corresponding to various reaction mechanism for T2N sample.

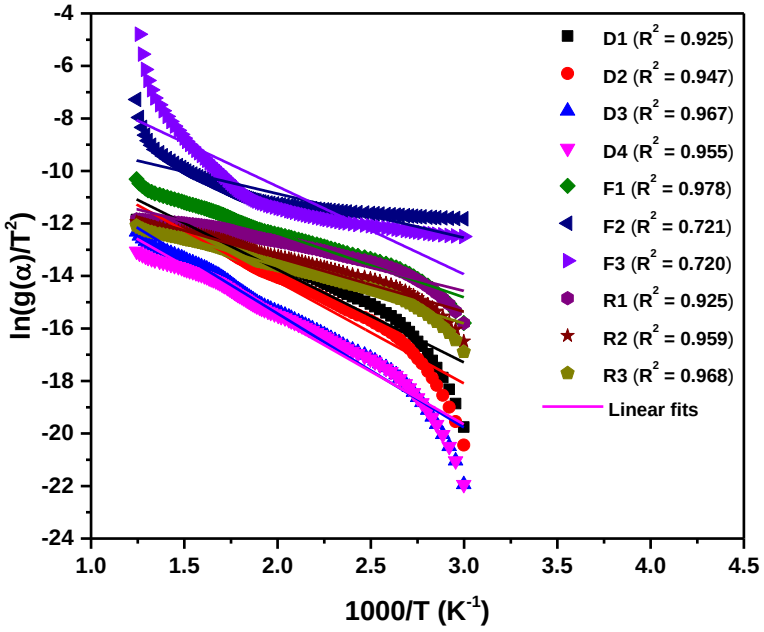

Figure 6.4 (d): Best linear fitted curves corresponding to various reaction mechanism for T4N sample.

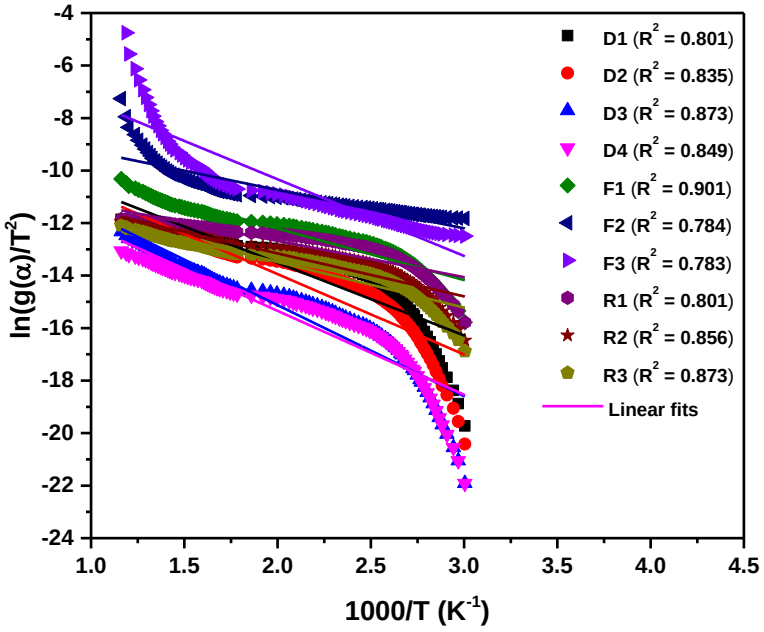

Figure 6.4 (e): Best linear fitted curves corresponding to various reaction mechanism for T6N sample.

the linear fitted curve between $ln\left(\frac{g(\alpha)}{T^2}\right)$ and $\frac{1000}{T}$ gives the value of activation enegy (E_a) and the pre-exponential factor (A) is calculated from the intercept. In order to identify appropriate $g(\alpha)$, various reaction mechansim have already been given in Table 4.5 (Chapter 4). Fig. 6.4 (b) – 5.4 (e) shows the linear fitted curves corresponding to various reaction mechanism for all the samples. The reaction mechanism followed, activation energy and pre-exponential factor of samples are given in Table 6.3.

Table 6.3: The reaction mecahnism, activation energy and pre-exponential factor of all the samples.

Samples	Reaction Mechanism	Activation Energy (kJ mol^{-1})	Pre-exponential factor (min^{-1})
T0N	F1	15.23	1.02×10^{-5}
T2N	F1	15.84	9.40×10^{-6}
T4N	F1	20.23	2.24×10^{-5}
T6N	F1	16.29	1.28×10^{-5}

6.1.5 HRTEM analysis

HRTEM micrographs of undoped and 0.6 mol % Ni doped TiO_2 nanoparticles are shown in Fig. 6.5 (a). It is evident from Fig. 6.5 (a), that the particles are nearly spherical in shape. The lattice arrays of samples show interplanar spacing coresponding to the (101) plane of anatase phase. Selected area electron diffraction (SAED) pattern supports the nanocrystallinity of synthesized samples. The particle size distribution calculations are done using *AxioVision Rel.4.9.1.0* as aggregates of nanoparticles have formed due to the very high surface free energy of small nanoparticles. From Fig. 6.5 (b), the average particle size of undoped and 0.6 mol % Ni doped TiO_2 sample is obtained as 19.70 nm and 14.59 nm, respectively.

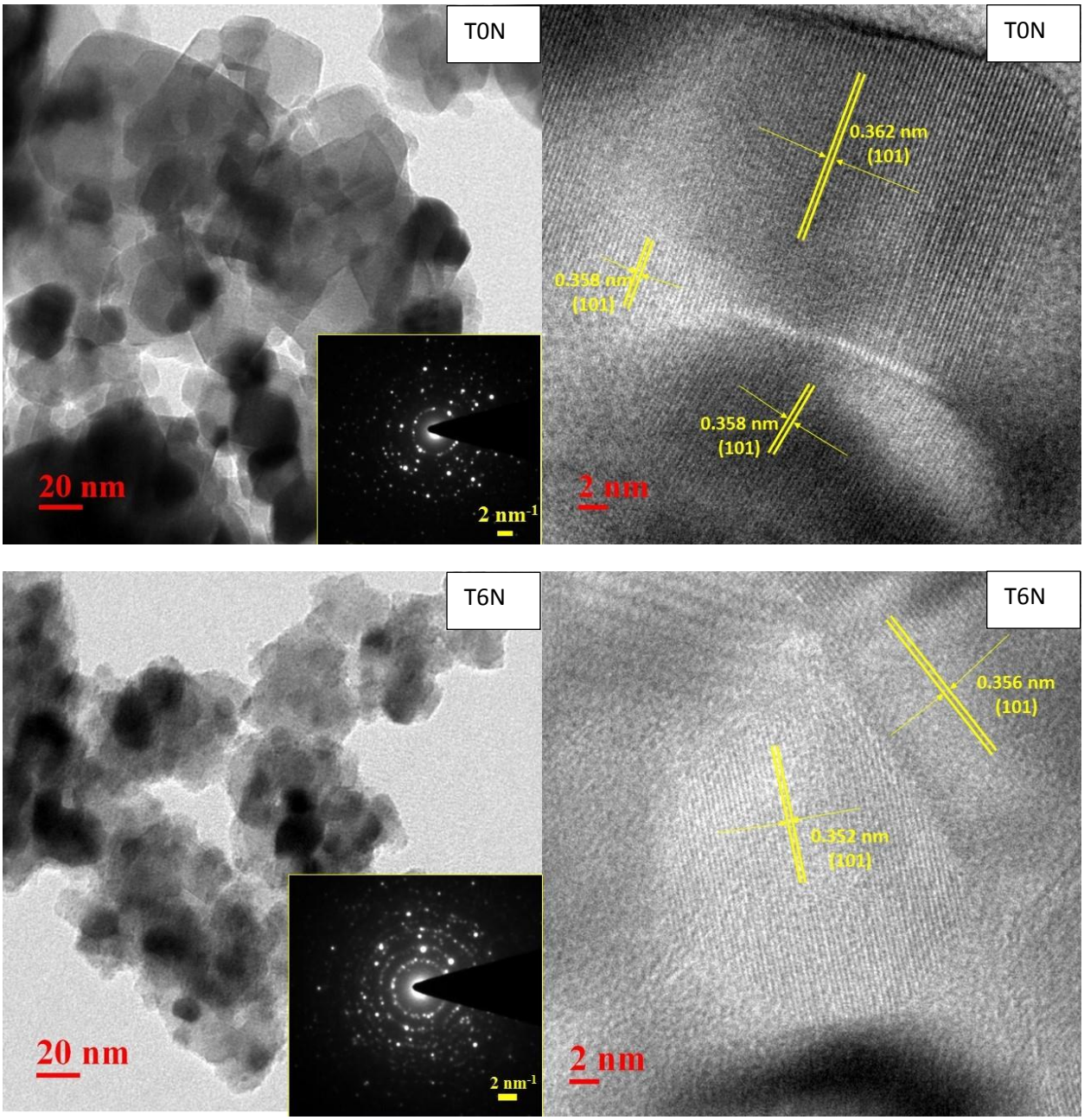

Figure 6.5 (a): HRTEM micrographs of (a) undoped (T0N) and (b) 0.6 mol % Ni doped TiO_2 (T6N) nanoparticles.

The estimated particle size obtained from XRD measurement is slightly higher as compared to the TEM measurement, which may be ascribed to the broadening of XRD peaks due to

geometric reasons. The TEM results are in correlation with the results obtained from XRD analysis i.e. the particle size is decreased in doped sample.

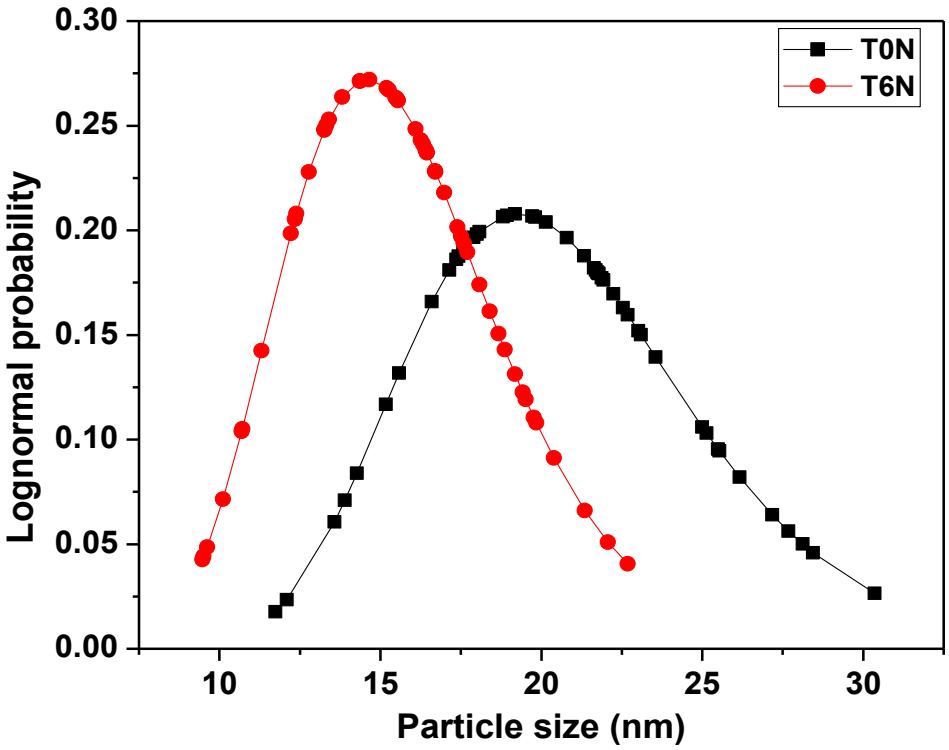

Figure 6.5 (b): Particle size distribution of nanoparticle's size fitted with lognormal of T0N and T6N samples.

6.1.6 PL analysis

Fig. 6.6 illustrates the photoluminescence spectra of undoped and Ni doped TiO_2 nanoparticles at the excitation wavelength of 400 nm. The PL emission intensity mainly depends on the recombination of excited electron-hole pairs. The lower PL intensity reveals the decrease in recombination rate [18]. The PL spectra of anatase TiO_2 has three origins i.e. due to self-trapped excitons, oxygen vacancies and can also be due surface defects [19]. Most of the surface states have oxygen vacancies or the Ti^{4+} ions adjacent to oxygen vacancies. The emission peak at 490 nm is associated with charge transfer transition from Ti^{3+} to TiO_6 octahedral [19]. The peak at

457 nm is related with oxygen related defect sites. The emission peaks in the visible region are attributed to the defect levels below conduction band. It is evident from Fig. 6.6 that PL intensity decreases with increase in doping. This is due to the reason that after photoexcitation, the electrons in conduction band can either go to oxygen defect levels or to the d-states of nickel. At higher dopant concentration, the distance between the dopants and defects decreases. Decrease in the distance will increase the interaction between them, increasing the energy transfer between the dopants and also between dopants and defects. In this process, the energy is dissipated non radiatively, which decreases the overall intensity [20]. It plays an important role in photocatalytic activity. Lower recombination rate of electron hole pairs in doped samples favors their higher photocatalytic activity.

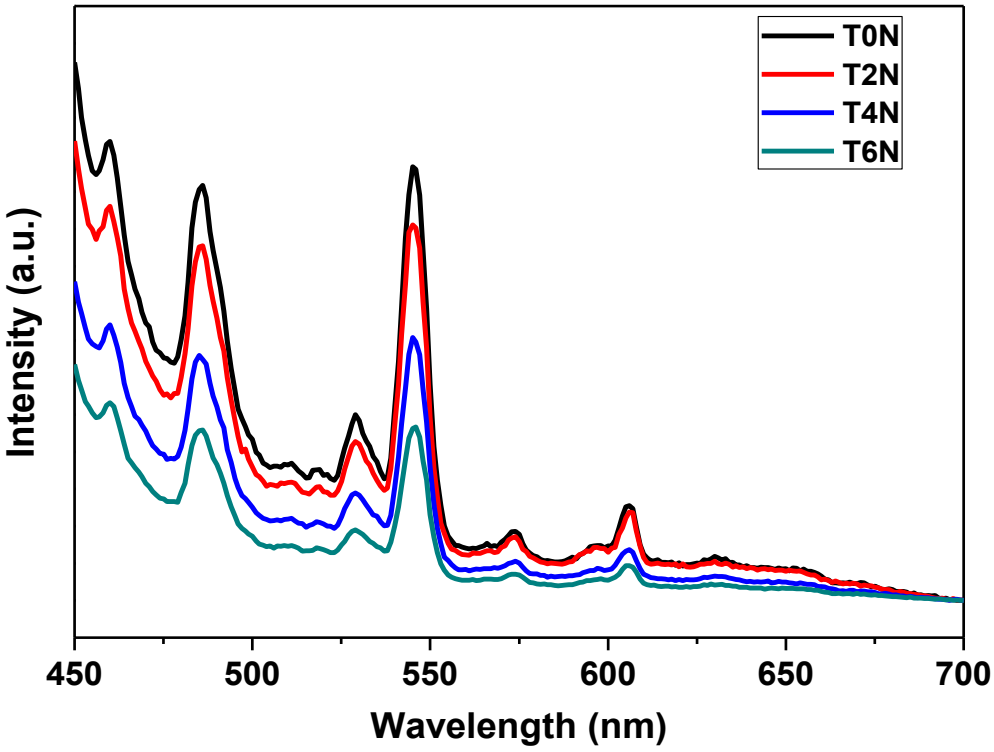

Figure 6.6: Photoluminescence spectra of undoped and Ni doped TiO_2 nanoparticles calcined at 450 ^oC.

6.1.7 Photocatalytic degradation of diethyl phthalate

Fig. 6.7 (a) shows the kinetic study of degradation of diethyl phthalate in presence of T0N, T2N, T4N, T6N, T8N, and T10N samples during light irradiation. The linearity in the curves obtained indicates that degradation of diethyl phthalate with each photocatalyst follow the pseudo first order kinetic model, $-ln\frac{C}{C_o} = k_{app}t$, where C is concentration of diethyl phthalate at time t, C_o is the initial concentration, k_{app} is the apparent first-order rate constant (min^{-1}) [21]. The rate constants derived from $-ln\ C/C_o$ versus t plots are given in table 6.3. The rate constants for photocatalytic reaction using T0N, T2N, T4N, T6N, T8N and T10N are found to be $0.41x10^{-2}$, $0.62x10^{-2}$, $0.71x10^{-2}$, $1.3x10^{-2}$, $1.0x10^{-2}$ and $0.9x10^{-2}$, respectively. The maximum rate constant for T6N sample reveals about its highest photocatalytic activity as compared to other samples. The apparent rate constant for the degradation of AO7 dye using Ni doped TiO_2 sample has been reported to be $2.5x10^{-3}$ [22].

Fig. 6.7(b) shows the linear plots of pseudo second order model for the degradation of diethyl phthalate in presence of photocatalysts and UV-vis light. The kinetics of pseudo second order photocatalytic degradation of diethyl phthalate is determined by using equation 4.10. The fitting of experimental data to the pseudo second order model is not so ideal with low correlation coefficient. The apparent constant (k_{2app}) is calculated from slope of *1/C* versus irradiation time. The apparent rate constants and correlation coefficients for pseudo first order and second order are given in Table 6.4.

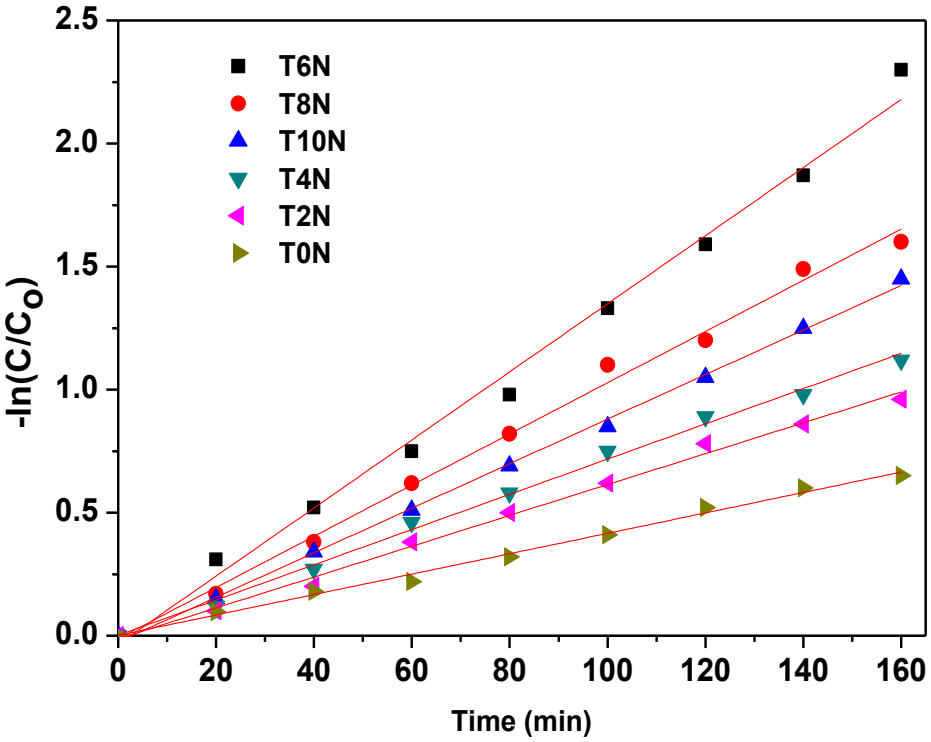

Figure 6.7 (a): Linear plots of pseudo first order when C_o = 30 ppm, catalyst load = 1g/l.

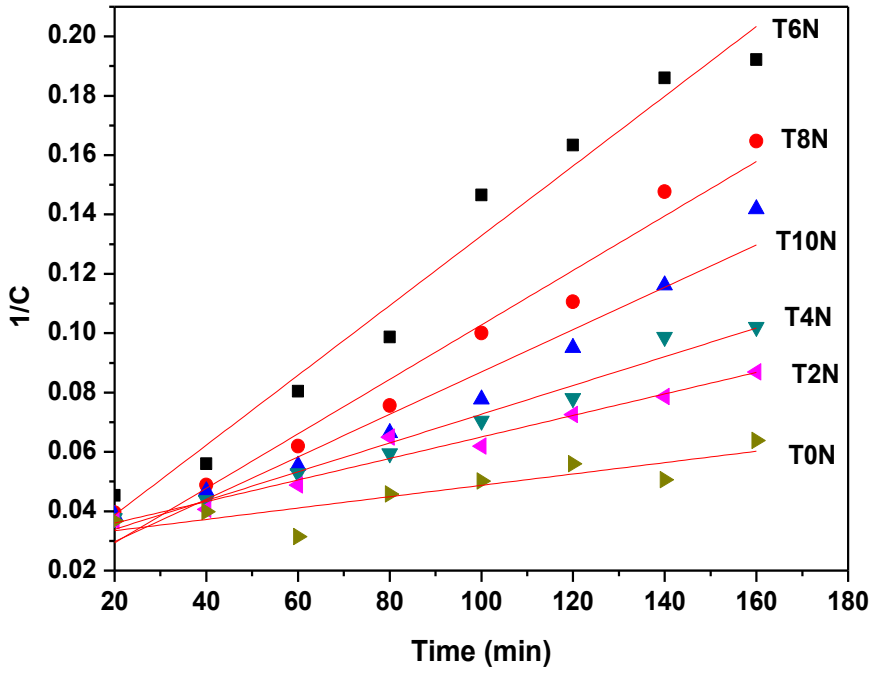

Figure 6.7 (b): Linear plots of pseudo second order when C_o = 30 ppm, catalyst load = 1g/l.

Table 6.4: The value of apparent rate constants for pseudo first order and pseudo second order model.

Sample Id	Apparent reaction rate constant, k_{1app} (min^{-1}) (Pseudo first order)	R^2 (Pseudo first order)	Apparent reaction rate constant, k_{2app} (min^{-1}) (Pseudo second order)	R^2 (Pseudo second order)
T0N	$0.41x10^{-2}$	0.9927	$1.9x10^{-4}$	0.9694
T2N	$0.62x10^{-2}$	0.9951	$3.6x10^{-4}$	0.9474
T4N	$0.71x10^{-2}$	0.9987	$4.8x10^{-4}$	0.9728
T6N	$1.3x10^{-2}$	0.9959	$1.1x10^{-3}$	0.9507
T8N	$1.0x10^{-2}$	0.9950	$9.18x10^{-4}$	0.9628
T10N	$0.9x10^{-2}$	0.9941	$7.13x10^{-4}$	0.7469

T6N sample has an optimum dopant concentration of 0.06 mol % Ni where the dopants act as trapping sites. In T8N and T10N sample, having higher dopant concentration than T6N, dopants act as recombination centers. Beyond the optimum dopant concentration, the rate of recombination starts dominating according to equation 5.1. With increase in dopant concentration above an optimum level, the rate of recombination increases exponentially. This is because the average distance between the trapping sites confined in a domain decreases [21].

Fig. 6.7 (c) shows the UV-vis spectral change of diethyl phthalate during irridation in presence of T6N sample. In UV-vis spectrum of diethyl phthalate, two intense bands at wavelengths of 229 nm and 276 nm have been obtained. The decrease of absorption peak of diethyl phthalate at λ_{max}= 229 nm indicates the degradation of diethyl phthalate during photo degradation. The percentage of degradation of diethyl phthalate is determined by the using equation 4.11. The percentage degradation of diethyl phthalate is 93 % in 160 min. Plot of % degradation and time is given Fig. 6.7 (d).

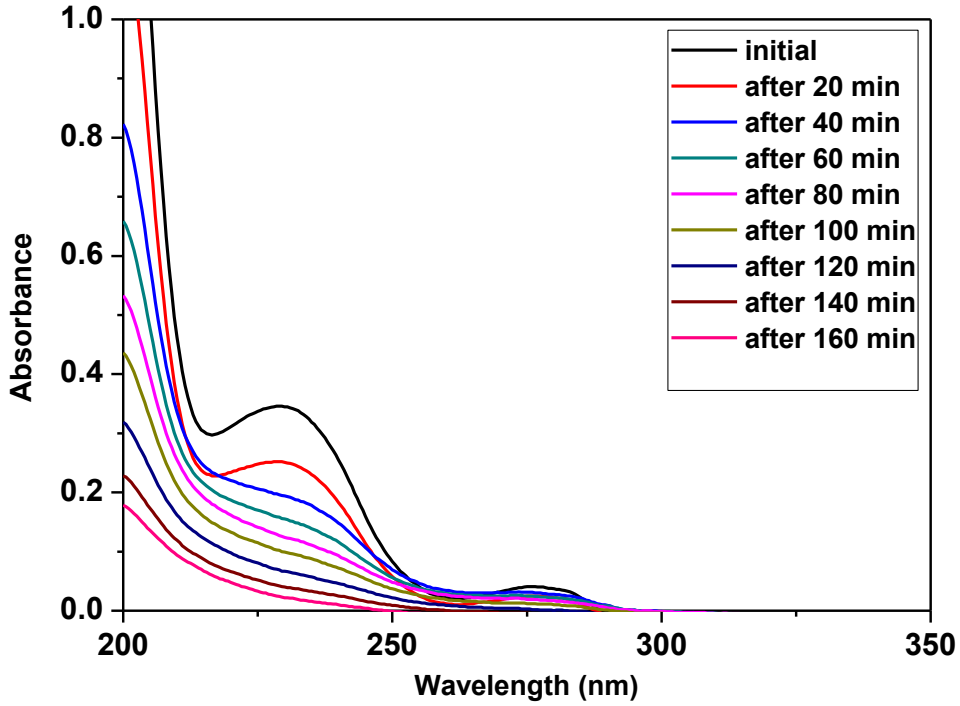

Fig. 6.7 (b): Degradation of diethyl phthalate during light irradiation in presence of 0.6 mol % Ni-TiO_2 nanoparticles when C_o = 30 ppm, catalyst load = 1g/l.

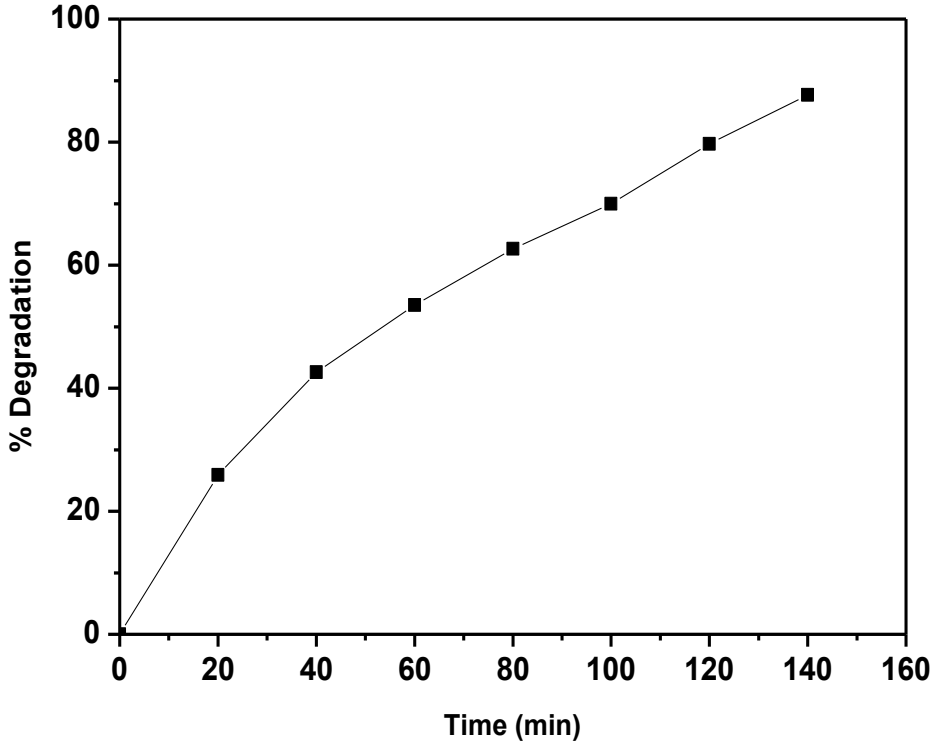

Figure 6.7 (d): Change in % degradation of diethyl phthalate as a function of irradiation time.

6.1.8 Conclusions

Doping of Ni in TiO_2 restricts the growth of particles and promotes the formation of anatase phase. According to XRD analysis, the crystallite size of T0N, T2N, T4N and T6N samples is obtained to be approximately 29, 28, 27 and 24 nm, respectively. The value of Urbach energy increases with dopant concentration indicating higher disorder in doped samples. However, optical band gap does not follow any trend with dopant concentration. The peak position shifts towards the lower wave number with the increase of Ni doping as has been observed in FTIR spectra. The HRTEM results are in correlation with the results obtained from XRD analysis i.e. the particle size decreases with increase in dopant concentration whereas negligible change in morphological structure is observed with increased doping. T6N sample show best photocatalytic activity due to lowest crystallite size and higher disordering in this particular sample. Ni doping in TiO_2 has facilitated the degradation of phthalate ester. The optimum amount of doping is found to be 0.6 mol %, because doping higher than 0.6 mol %, decreases the photocatalytic degradation. The rate of reaction increases with decrease in particle size.

References

1. L. Agartan, D. Kausuz, J. Park, A. Ozturk Ceram Int 41 (2015) 12788.
2. P. Hermawan, H.D. Pranowo, I. Kartini, Indo J Chem 11 (2011) 135.
3. H.H. Tseng, M.C. Wei, S.F. Hsiung, C.W. Chiou, Chem Eng J 150 (2009) 160.
4. I. Ganesh, A.K. Gupta, P.P. Kumar, P.S.C. Sekhar, K. Radha, G. Padmanabham, Scientific World J 2012 (2012) 1.
5. K. Parveen, R. Vyas, Acta Chim Pharm Indica 6 (2016) 135.
6. P. Vijayan, C. Mahendiran, C. Suresh, K. Shanthi, Catal Today 141 (2009) 220.
7. D.A.H. Hanaor, C.C. Sorrell, J Mater Sci 46 (2011) 855.
8. B.D. Cullity, S.R. Stock (2001) Elements of X-ray Diffraction, 3rd edn Addision wesley-Publishing compony, Massachusetts.
9. K. Umar, M.M. Haque, M. Muneer, T. Harada, M. Matsumura, (2013) J Alloys Compd 578 (2013) 431.
10. T. Aguilar, J. Navas, R. Alcantara, C.F. Lorenzo, J. Gallardo, G. Blanco, J.M. Calleja, Chem Phys Lett 571 (2013) 49.
11. S. Paul, A. Choudhary, Appl Nanosci 4 (2014) 839.
12. E. Mansour, K. El-Egili, G. El-Damrawi, Phys B 39 (2007) 221.
13. J. Tauc, A. Menth, J Non Cryst Solids 8 (1972) 569.
14. S. Sood, A. Umar, S.K. Mehta, S.K. Kansal, J Colloid Interface Sci 450 (2015) 213.
15. L. Kumaresan, A. Prabhu, M. Palanichamy, E. Arumugam, V. Murugesan, J Hazard Mater 186 (2011) 1183.
16. N. Venkatachalam, M. Palanichamy, V. Murugesan, J Mol Catal A Chem 273 (2007) 177.

17. C.M. Whang, S.S. Lim, Bull Korean Chem Soc 21 (2000) 1181.

18. R.S. Sabry, Y.K. Al-Haidarie, M.A. Kudhier J. Sol-Gel Sci Technol 78 (2016) 299.

19. A.K. Tripathi, M.C. Mathpal, P. Kumar, V. Agrahari, M.K. Singh, S.K. Mishra, M.M. Ahmad, A. Agarwal, Adv Mater Lett 6 (2015) 201.

20. B. Choudhury, A. Choudhury, J Lumin 136 (2013) 339.

21. L.G. Devi, N. Kottam, S.G. Kumar, K.S. Anantha Raju, Catal Lett 131 (2009) 612.

22. O.M. Min, Y.S. Yong, Advances in Environmental Biology 8(2014) 501.

Overview

In this chapter, the effect of different particle size distribution of TiO_2 nanoparticles obtained by varying the calcination temperature on the photocatalytic degradation of phthalate ester has been summarized. The effect of Fe doping, Cu doping, Fe-Cu codoping into TiO_2 on photcatalytic degradation of diethyl phthalate has been concluded. Conclusions are made from the effect of various concentration of Ni dopant into TiO_2 nanoparticles for the photocatalytic degradation of diethyl phthalate. Based on the observation of the present work, some suggestions to carry out more work in this field have also been given at the end of this chapter.

7.1 Conclusions

In the present work, undoped and transition metal doped TiO_2 nanoparticles have been synthesized. The main objective behind this work was to study photocatalytic degradation of phthalate ester using undoped and transition metal doped TiO_2 nanoparticles. The undoped TiO_2 nanoparticles having different particle size distribution have been sucessfully synthesized. The various structural, optical and thermal properties of samples have been studied with aim to utilize them for the photocatalytic degradation of diethyl phthalate. The single metal cation doping and codoping of Fe and Cu into TiO_2 nanoparticles has been carried out. A comparative study has also been done for single and codoping of Fe and Cu on structural, optical, thermal and photocatalytic properties. A series of samples having different concentrations of Ni dopant into TiO_2 nanoparticles has been synthesized. The optimum concentration of Ni into TiO_2 for the highest degradation of diethyl phthalate has been determined.

Undoped TiO_2 nanoparticle having different particle size distribution have been synthesized by the sol-gel method. The samples were calcined at three different temperatures (200, 300 and 400 ^oC). XRD and Raman studies showed the presence of anatase and minor brookite phase. The band gap energy values of the samples were found to be in range of 3.12-3.18 eV. The optimum anatase-brookite ratio for high photocatalytic degradation of diethyl phthalate in present study was found to be 99 to 1 %, respectively. The particle size of the samples was obtained in the range of 5-10 nm according to HRTEM which agreed well with the XRD results. Particle size of the samples increased with increasing calcination temperature. The higher photocatalytic activity of sample calcined at 200 ^oC as compared to other calcined samples at 300 ^oC and 400 ^oC was attributed to the small particle size, more disorder and weak bonds.

Undoped, Fe-doped, Cu-doped and (Fe, Cu) codoped TiO_2 nanoparticles were prepared via sol-gel method and their photocatalytic activity was evaluated. XRD studies confirmed the presence of anatase phase with small fraction of rutile phase in all samples. UV-vis absorption studies showed that absorption shifted to visible region upon doping and codoping. FTIR studies indicated the weakening to bond due to structural rearrangements in doped samples. The average particle size of samples was found to be between 10-11 nm in samples according to HRTEM which was in correlation with XRD. Photoluminescence studies showed that the recombination of electron hole pairs decreased upon doping. (0.075 mol % Fe, 0.075 mol % Cu) codoped TiO_2 sample showed higher photocatalytic activity than undoped or single element cation doped TiO_2. The enhancement in photocatalytic activity upon codoping was attributed to the higher disordering and increased absorption as well as the efficient transfer of electron-hole pairs through co-dopant ions in the sub energy bands of TiO_2.

Undoped and a series of Ni doped TiO_2 nanoparticles were synthesized via sol-gel method. XRD studies confirmed the presence of anatase and rutile phase. Doping of Ni in TiO_2 restricted the growth of particles and promoted the formation of anatase phase at the cost of rutile phase. The crystallite size of samples was obtained to be in range of 24-29 nm. The value of Urbach energy increased with dopant concentration, indicating higher disorder in doped samples. However, band gap did not follow any trend with dopant concentration. The peak position shifted towards the lower wave number with the increase of Ni doping as observed in FTIR spectra. The HRTEM results were in correlation with the results obtained from XRD analysis i.e. the particle size decreased with increase in dopant concentration whereas negligible change in morphological structure was observed with increased doping. 0.6 mol % Ni doped TiO_2 sample showed best

photocatalytic activity due to lowest crystallite size and higher disordering in this particular sample. Ni doping in TiO_2 facilitated the degradation of phthalate ester.

From these studies it can be concluded that doping of transition metals whether it is single cation doping or codoping, increased the photocatalytic degradation of phthalate ester as compared to undoped TiO_2 sample. In present study, the (0.075 mol % Fe, 0.075 mol % Cu) codoped TiO_2 gives the highest rate constant for the degradation of diethyl phthalate. There is always an optimum amount of dopant concentration for highest photocatalytic degradation. Above or below that concentration, the degradation is decreased. Doping changes the phase composition, particle size, band gap values, Urbach energy, bond lengths, recombination rate of electron hole pairs etc. These changes lead to the higher degradation of phthalate ester in case of doped sample than undoped sample. The samples like T2Fe, T3Cu, T4FeCu, T5FeCu and T6FeCu can be used to degrade organic pollutants in visible region of light whose band gap is greatly decreased upon doping. In each series, the rate of reaction increased with decreasing particle size.

7.2 Future Scope

From the developed nanoparticles following study can also be undertaken.

- Photocatalytic degradation of more colorless recalcitrant organic compounds can be explored.
- Study to replace artificial energy sources with solar light irradiation.
- Designing such type of reactors which can be used on industrial level using solar light for purification of water.
- New combinations of dopants can also be explored for higher degradation.